NEW METHODS FOR ACCURATE UPSCALING WITH FULL-TENSOR EFFECTS

A DISSERTATION
SUBMITTED TO THE DEPARTMENT OF ENERGY
RESOURCES ENGINEERING
AND THE COMMITTEE ON GRADUATE STUDIES
OF STANFORD UNIVERSITY
IN PARTIAL FULFILLMENT OF THE REQUIREMENTS
FOR THE DEGREE OF
DOCTOR OF PHILOSOPHY

Tianhong Chen

March 2009

I certify that I have read this dissertation and that, in my opinion, it is fully adequate in scope and quality as a dissertation for the degree of Doctor of Philosophy.

(Margot G. Gerritsen) Principal Co-Advisor

I certify that I have read this dissertation and that, in my opinion, it is fully adequate in scope and quality as a dissertation for the degree of Doctor of Philosophy.

(Louis J. Durlofsky) Principal Co-Advisor

I certify that I have read this dissertation and that, in my opinion, it is fully adequate in scope and quality as a dissertation for the degree of Doctor of Philosophy.

(James V. Lambers)

Approved for the University Committee on Graduate Studies.

Abstract

Upscaling is commonly applied to generate practical reservoir simulation models from highly detailed geocellular descriptions. It is often the case that fine-scale geological features, or the principal correlation directions of the geostatistical model, are not aligned with the simulation grid. For such systems, full-tensor effects generally arise at the coarse scale, even if the fine-scale permeability is isotropic.

In this thesis, new upscaling procedures designed to accurately capture full-tensor effects are developed and evaluated. These techniques are based on variable compact multipoint (VCMP) flux approximations, and are applied to both Cartesian and non-Cartesian grids. The new upscaling procedures generate coarse-scale transmissibilities directly. The inclusion of global flow effects in upscaling computations is known to improve coarse-grid accuracy for highly heterogeneous systems. For this reason, approaches for incorporating global flow effects into the upscaled models are investigated. These include global methods, in which global fine-scale flow information is used for the upscaling, and local-global techniques, in which the global flow information derives from coarse-scale simulations.

We first consider global upscaling methods and develop two procedures within the context of VCMP – one in which the upscaled model is determined directly (VCMP-DG) and one in which iteration of the coarse-scale model is used to minimize

the mismatch between coarse-scale fluxes and integrated fine-scale fluxes (VCMP-IG). These two approaches use a complementary local flow in addition to a fine-scale global flow in the determination of upscaled transmissibilities. VCMP generates locally varying stencils that are optimized for flow accuracy and minimum stencil width. To guarantee monotonicity, the VCMP stencils are adapted to assure the coefficient matrix is an M-matrix whenever nonmonotone solutions are encountered. This is referred to as a selective M-fix procedure.

The new global VCMP upscaling methods are applied to multiple realizations of two-dimensional fine-scale permeability descriptions to generate coarse models defined on both Cartesian and irregular quadrilateral grids. Both log-normally distributed permeability fields with oriented layers and channelized models are considered. Six different upscaling techniques (extended local, direct global, and iterated global, each using both two-point and VCMP flux approximations) are assessed for four different sets of global boundary conditions. The global VCMP techniques consistently display high degrees of accuracy for both pressure and flux. For the oriented-layer cases, where full-tensor effects are important, the global VCMP methods are shown to provide clearly better overall accuracy than analogous methods based on two-point flux approximations. For channelized cases in which full-tensor effects are not significant, both types of methods provide high levels of accuracy. The selective M-fix procedure is also shown to lead to improved accuracy, which can be significant in some cases. In total, for the systems considered here, the new global VCMP upscaling techniques are observed to provide the best overall accuracy of any of the upscaling methods investigated.

Global upscaling methods are not always appropriate because they require global fine-scale flow solutions. Therefore, we also develop and evaluate a variable compact multipoint adaptive local-global technique (VCMP-ALG), as a more efficient alternative to global VCMP methods. This approach avoids global fine-scale computations.

The VCMP-ALG method successfully combines the positive attributes of its two underlying component procedures – the VCMP flux scheme and adaptive local-global (ALG) upscaling. The performance of the local-global VCMP upscaling technique is evaluated for multiple realizations of oriented variogram-based models and synthetic deltaic systems. Extensive numerical results for two-dimensional cases demonstrate that the VCMP-ALG approach provides better overall accuracy than either of the underlying methods applied individually. However, as would be expected, it does not achieve the level of accuracy of the global VCMP methods. We also present results for two-phase oil-water flows and demonstrate that the VCMP-ALG transmissibilities, although computed from single-phase flow computations, are well-suited for use in two-phase flow simulations.

The global VCMP and VCMP-ALG methods described above are also applied to irregular quadrilateral grids. A level of accuracy comparable to that achieved for Cartesian grids is observed. These computations, however, are all for logically Cartesian grids (i.e., grids that maintain a logical i, j structure). In the final portion of this thesis, the upscaling procedures are extended to treat corner-point grids with pinchouts (in which case the i, j structure is lost). Such grids are often used in practice for modeling geological layers that merge into other layers. Coarse-scale simulation results demonstrate that high degrees of accuracy are again achieved through use of VCMP-ALG or global VCMP methods.

Acknowledgements

First, my sincere thanks go to my advisors Professor Margot Gerritsen and Professor Louis Durlofsky for their valuable guidance and continuous support and for their careful reading of this dissertation. Margot has been my advisor since my Masters program. She always supported my research work and has provided lots of encouragement. I have also benefited from Margot's sparkling research ideas and broad areas of interest. I would like to thank Professor Louis Durlofsky for his detailed instructions on the project. I learned a lot from his knowledge and his rigorous attitude toward research.

I owe many thanks to Professor James Lambers. I worked closely with Jim on this project. He provided me with his research code on VCMP-EL methods as well as many valuable suggestions and comments. Whenever I had a problem with the code or the method, I always turned to Jim for help. I also want to extend my thanks to Professor Khalid Aziz for serving on my committee and to Professor Biondo Biondi for kindly chairing my defense.

I am grateful to Yuguang Chen and Bradley Mallison at Chevron for many useful discussions and suggestions on local-global and iterative global upscaling methods. I also thank Jeremy Kozdon at Stanford University for providing me with code for simulating two-phase flow.

This work was funded by BP and by the affiliate members of the SUPRI-C research consortium at Stanford. Special thanks go to Michael King at BP for facilitating BP

support and for providing valuable insights on upscaling during my internship at BP.

I owe my gratitude to all the faculty, staff, and students in the Department of Energy Resources Engineering. The department is like a big family full of support and friendship. I truly enjoyed my stay there.

Last, but not least, I am deeply grateful to my family. I would like to express my gratitude to my parents for their love and support during the years. My sincere thanks also go to my husband, Qing Chen, for his constant help and support throughout my graduate study. He shared my happiness and difficulties, and has provided tremendous love and encouragement.

Contents

List of Tables

List of Figures

Chapter 1

Introduction

Reservoir simulation is a key component of the modern reservoir management process as it can provide forecasts for oil recovery and can be used to optimize reservoir performance. Reservoir simulation is conducted on a simulation model with reservoir geometry and properties as input. Reservoir characterization, however, is performed on a geocellular model. Scale gaps exist between geocellular models and simulation models. The geocellular model is often constructed on a very fine scale in order to integrate various types of data, which are collected at multiple scales, such as seismic data ($\sim$ 10–100 ft), well log data ($\sim$ 0.5 ft), and core data ($\sim$ 1 inch). Geocellular models can also contain very complex geological features, such as cross-bedding, faults, and pinch-outs.

Because fine-scale geological features, e.g., thief zones, can impact fluid flow significantly, capturing such features at the fine scale is very important. A typical geocellular model of a heterogeneous oil reservoir may contain on the order of $10^7 \sim 10^8$ cells. Although feasible, numerical simulations using such large geological models are usually still too expensive for realistic applications. This is because, in practice, multiple simulations must be performed in order to choose among various recovery or well placement strategies. In addition, the impact of reservoir uncertainty is typically

quantified by simulating a large number of geostatistical realizations of the reservoir (Caers, 2005). For these reasons, geological models are usually upscaled by a factor of 10 to 1000 in practical reservoir simulation settings. Figure 1.1 illustrates the upscaling process. It is especially important to use a coarsened model for fast simulation of compositional or thermal processes, and for optimization and risk analysis, as these are all CPU demanding.

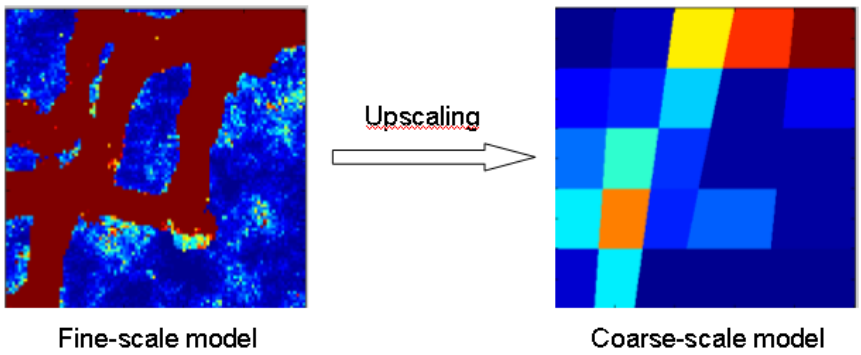

Figure 1.1: Illustration of the upscaling process. Fine-scale permeabilities (50×50 grid) are upscaled to provide coarse-grid properties (5×5 grid).

1.1 Literature Review

In this section, we review existing upscaling and discretization algorithms for regular and irregular grids. We focus on flow-based upscaling methods including local and extended local methods, local-global methods, and global methods, and also on the combination of upscaling methods with multipoint flux schemes.

1.1.1 Flow-Based Upscaling Methods

Within the context of subsurface flow modeling, the most fundamental property considered for upscaling is the rock permeability. Upscaling of permeability has been an

active area of research, and extensive reviews of existing methods are given in Renard and de Marsily (1997), Farmer (2002), Durlofsky (2005), Gerritsen and Durlofsky (2005), and Wen and Gomez-Hernandez (1996), among others. Methods can be classified as permeability or transmissibility upscaling procedures depending on the coarse-scale property computed. Permeability upscaling methods entail the determination of equivalent permeability tensors for each coarse-scale grid block. Interface transmissibilities, which are required by finite-volume simulators, are then computed from the equivalent permeabilities in nearby grid blocks (transmissibility can be viewed as the numerical analog of permeability and involves both permeability and grid geometry). In transmissibility upscaling techniques, by contrast, the coarse-scale transmissibility at the interface is determined directly in the upscaling procedure. Transmissibility upscaling has been shown to provide more accurate coarse-scale models than permeability upscaling for highly heterogeneous systems (e.g., Chen et al., 2003; Romeu and Noetinger, 1995).

For single-phase flow, only porosity and the absolute permeability need to be upscaled. The upscaled properties computed from single-phase flow computations can be applied to multiphase flow problems and result in accurate coarse-scale models for many cases. In these models, the coarse-scale relative permeabilities are the same as those used at the fine scale. This type of upscaling is referred to as single-phase upscaling (Durlofsky, 2005). In two-phase upscaling, the two-phase flow parameters, such as relative permeability, are also upscaled (e.g., Darman et al., 2002; Pickup and Sorbie, 1996). Two-phase upscaling is less frequently used due to the high computational cost that is involved in determining the upscaled relative permeability (which requires time-dependent two-phase flow simulations) and the dependency of the resulting relative permeabilities on well conditions (Barker and Thibeau, 1997).

Upscaling methods can also be distinguished in terms of the size of the domain used for the determination of the upscaled properties. In purely local upscaling,

the upscaled transmissibility for the interface between two coarse grid blocks i and $i+1$ is computed by solving a flow problem over the fine-scale domain corresponding to these two coarse blocks. Figure 1.2 illustrates this for a general quadrilateral grid, where the solid cells depict the local region. Note that the local region here includes all fine cells needed to form rectangular coarse blocks that cover the irregular coarse blocks. Commonly, a flow is driven through this domain by applying Dirichlet boundary conditions on the inlet and outlet boundaries and no-flow conditions on the boundaries parallel to the flow direction (Durlofsky, 2005). Periodic boundary conditions (Durlofsky, 1991), or linear pressure boundary conditions (King et al., 1998; King and Mansfield, 1999) are also possible.

In extended local upscaling, border regions are added around the two coarse blocks to reduce the impact of the assumed boundary conditions (e.g., Gomez-Hernandez and Journel, 1994; Holden and Lia, 1992; Wen et al., 2003a,b; Wu et al., 2002). In Figure 1.2, for example, the extended local region (indicated by the dashed lines) has a border region of one coarse-scale cell in each direction, i.e., the number of rings of coarse cells, which we designate as r_c, is 1. Wen et al. (2003b) used a border region procedure for their permeability upscaling. Their numerical tests showed that improved accuracy in flow and transport computations were obtained using border regions. The level of improvement varied for different permeability fields. The enhanced accuracy from using border regions was significant on the lower portion (layers 36–85) of the SPE 10 model (Christie and Blunt, 2001) where the permeability fields are channelized, while little improvement was observed in the upper portion (layers 1–35), where the permeability fields are continuous. Wen et al. (2003b) and Wen et al. (2000) also studied the effect of the size of the border region. In their test cases, the use of $r_c = 1$ seemed to suffice. Little improvement in accuracy was obtained through the use of $r_c = 2$ compared to $r_c = 1$. It may therefore not be beneficial to use border regions larger than $r_c = 1$ due to the increased computational cost

involved as the border region size increases. Wen et al. (2003b) found that the effect of the boundary conditions (periodic boundary conditions and constant pressure-no flow boundary conditions) was reduced when the border region was used, which was also reported by Holden and Lia (1992).

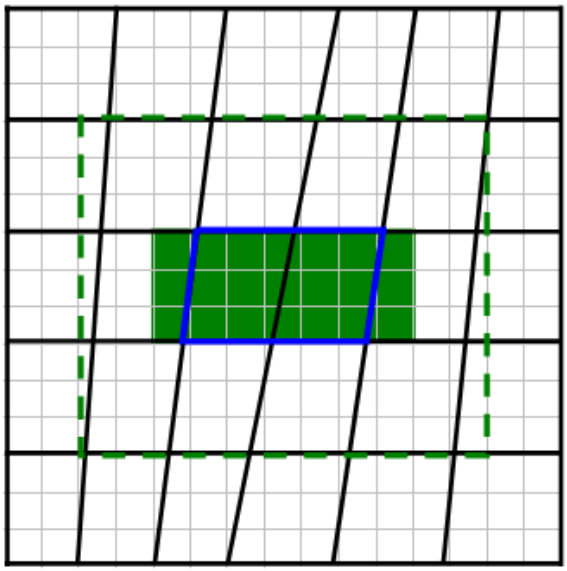

Figure 1.2: A local region (solid) and border region (dashed boundaries) for a general quadrilateral coarse grid. The coarse cells are drawn in heavier lines and underlying fine Cartesian grid cells in lighter lines.

In global upscaling approaches, here referred to as direct global upscaling, global fine-scale problems are solved to determine the coarse-scale parameters (Chen et al., 2008; Holden and Nielsen, 2000; Mallison et al., 2006; Zhang et al., 2008). Global upscaling techniques can provide better accuracy than local or extended local procedures as they are better able to capture the effects of large-scale permeability connectivity. They do however require the solution of a global flow problem, which can be expensive or even prohibitive in some cases. Holden and Nielsen (2000) computed effective permeabilities by minimizing the difference in the velocity and pressure solutions between

the coarse-scale model and the fine-scale model. Zhang et al. (2008) developed a well-driven upscaling method, which uses fine-scale solutions to provide actual boundary conditions for highly heterogenous systems. These investigators demonstrated improvements in coarse-model accuracy, which were significant in many cases, relative to that achieved using local upscaling procedures.

Recently, the iterative global method was developed to provide higher accuracy in the flux fields without increasing significantly the computational costs of the direct global approach (Chen et al., 2008; Mallison et al., 2006). This method finds a self-consistent solution by adjusting upscaled transmissibilities iteratively to match the fluxes from the reference global solution. As a result, it leads to very accurate estimates for flow rates, but does not guarantee high accuracy in the pressure solution. Refer to Chapter 2 of this thesis for more details on the iterative global method.

As indicated earlier, a potential disadvantage of global upscaling techniques is the need to solve a fine-scale flow problem. Though this fine-scale solution is feasible in many cases, it can be problematic if the geomodel is very highly resolved or if well conditions change significantly during the course of the simulation, in which case the upscaling computations may need to be repeated a number of times. In such instances, local-global upscaling can be a useful alternative to global procedures. Local-global methods (Chen and Durlofsky, 2006; Chen et al., 2003; Gerritsen and Lambers, 2008; Wen et al., 2006) incorporate global information using global coarse-scale (rather than global fine-scale) flow solutions.

Local-global upscaling was first formulated by Chen et al. (2003). Both coupled local-global (CLG) upscaling, in which two generic global flows are solved on the coarse scale (Chen et al., 2003), and adaptive local-global (ALG) upscaling, in which one global coarse-scale flow for a particular set of boundary conditions is solved (Chen and Durlofsky, 2006), have been developed. Wen et al. (2006) extended the local-global method to three dimensions and improved the computational efficiency

by using purely local upscaling for the first estimate and reduced border regions during the iterations. In the local-global technique, the boundary conditions for the local upscaling computations are interpolated from the coarse-scale pressure solution. One or more iterations are typically required to achieve self-consistency between the upscaled properties and the global flow field. More details are given in Chapter 3. Numerical results clearly demonstrate the advantages of local-global procedures over local and extended local techniques. All work mentioned above involved only Cartesian grids. Local-global upscaling was further extended by Gerritsen and Lambers (2008) to adapted Cartesian grids in a multi-level procedure. Durlofsky et al. (2007) applied the local-global technique to the construction of multiscale basis functions, within the context of a multiscale finite element method.

1.1.2 Multipoint Flux Approximation

Although the coarse-scale pressure equation is taken to be of the same form as the fine-scale pressure equation, significant full-tensor anisotropy can arise on the coarse scale as a result of the upscaling process, even if the fine-scale permeability is isotropic. This will occur, for example, if strong geological layering exists and this layering is skewed relative to the coarse grid. Full-tensor anisotropy can also appear from grid nonorthogonality effects. In the particular case of diagonal permeability tensors and orthogonal grids aligned with the principal permeability directions, it is appropriate to use two-point flux approximations (TPFA) for the solution of the governing flow equations. In TPFA procedures, the flow from one block to another depends only on the pressures in the two blocks. The limits of applicability and the level of error associated with TPFA techniques, in the context of global upscaling and local-global upscaling, are discussed in Chen et al. (2008).

When full-tensor permeabilities are included in the model, or the grid is nonorthogonal, it is well established that, in the general case, multipoint flux approximation

(MPFA) techniques are required to accurately represent full-tensor effects in finite-volume flow simulators (Aavatsmark et al., 1996; Edwards and Rogers, 1998; Lee et al., 2002). These methods express the flux between two adjacent grid blocks not only in terms of the pressure in those grid blocks, as in two-point flux approximations, but also in terms of pressures in a number of other grid blocks near the face. Aavatsmark et al. (1996) proposed two classes of discretization methods – the O-method and the U-method – for two-dimensional quadrilateral grids. Similar methods were developed for three dimensions in Aavatsmark et al. (1998). MPFA methods are more accurate than TPFA methods for systems with full-tensor anisotropy, but lead to increased computational costs because of wider discretization stencils. Most MPFA methods introduce a nine-point stencil in two dimensions and a 27-point stencil in three dimensions.

Edwards and Rogers (1998) proposed a nine-point flux-continuous finite-volume scheme in two-dimensions and also studied the convergence rates for discontinuous coefficients on nonorthogonal grids. Lee et al. (2002) found that significant errors can be introduced without appropriate treatment of full-tensor effects. Hence, they implemented a three-dimensional flux-continuous finite-volume formulation. They split the 27-point stencil in three dimensions into a 7-point stencil part and a remainder based on Taylor series expansion to simplify the linear solver. This idea was suggested earlier by Edwards (2000). Their split scheme is generally robust, but more efficient methods are required to solve the pressure equation with 27-point stencils.

Standard MPFA methods do not in general guarantee that the discretized problem results in an M-matrix, and therefore they can lead to nonmonotonic pressure solutions (Aavatsmark, 2002; Nordbotten et al., 2007). Such solutions are unphysical and can be problematic in practice. The monotonicity of MPFA solutions has been discussed in Nordbotten and Aavatsmark (2005) and Nordbotten et al. (2007) among others. To increase the monotonicity domain of the O-method, the L-method

was proposed with smaller flux stencils (Aavatsmark et al., 2006). Gerritsen et al. (2006) also addressed the monotonicity issue with their variable compact multipoint approximation (VCMP), which is discussed in more detail below.

A number of local and extended local upscaling procedures have been developed to provide full-tensor permeabilities or to be used within the context of MPFA. These include permeability (e.g., Durlofsky, 1991; Pickup et al., 1994; Wen et al., 2003b) and transmissibility upscaling techniques (Gerritsen et al., 2006; Jenny et al., 2003; Lambers et al., 2008). The VCMP methods (Gerritsen et al., 2006; Lambers et al., 2008), a recent family of transmissibility upscaling procedures, were designed to accurately capture full-tensor effects while guaranteeing monotone pressure solutions. VCMP generates locally varying stencils that are optimized for flow accuracy and minimum stencil width and can be adapted to ensure certain M-matrix properties. The method is discussed in more detail in Chapter 2. VCMP was designed for general grid topologies, but has so far been implemented only on Cartesian and adapted Cartesian grids. In addition, it has only been used in local and extended local upscaling procedures and has not been generalized for use with global upscaling. We note that ideas from VCMP have also been applied within the context of multiscale finite volume procedures (Hesse et al., 2008) to improve M-matrix properties.

1.1.3 Upscaling for Non-Cartesian Grids

Reservoirs are often highly heterogeneous, and may be heavily faulted, fractured, or have pinch-out zones. To capture these geological features or to better resolve well trajectories, irregular grids are widely used. Irregular grids can be generated by flow-based gridding, local grid refinement (e.g., Gerritsen and Lambers, 2008), and other techniques. Figure 1.3 present two examples of irregular grids. In Figure 1.3(a) a pinch-out is modeled (King and Mansfield, 1999), while in Figure 1.3(b) faults are resolved.

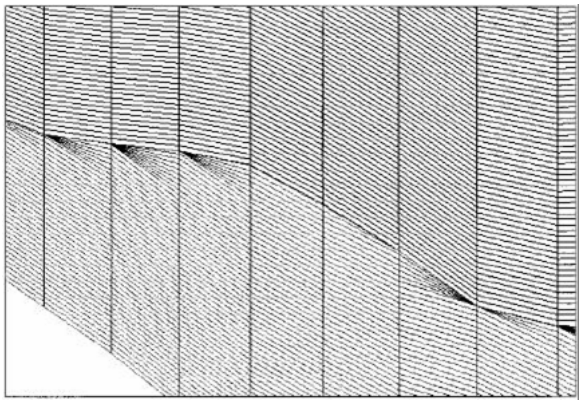

(a)

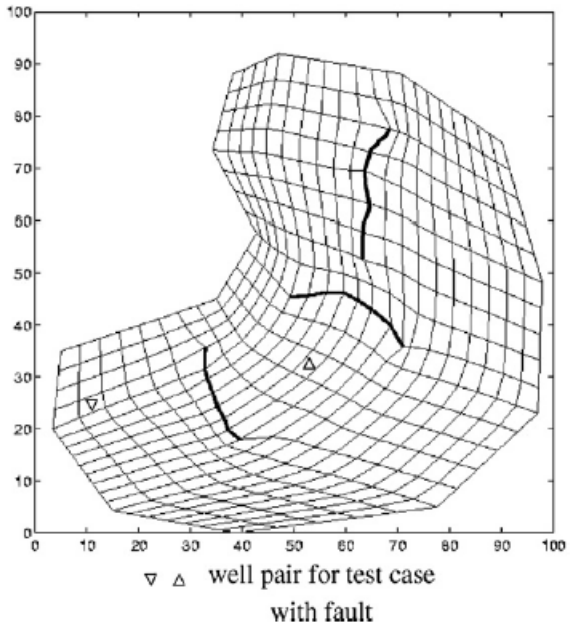

(b)

Figure 1.3: Examples of irregular grids: (a) pinch-out (from King and Mansfield, 1999) and (b) faults (from He and Durlofsky, 2006).

Compared to conventional Cartesian grids at the same density, irregular grids can better resolve the critical features in the reservoir. For example, Durlofsky et al. (1997) developed a nonuniform coarsening procedure, with high grid density in the connected regions of high permeability, to better capture important behaviors such as total flow rate and the breakthrough of the displacing fluid. Studies by Edwards et al. (1998) demonstrated that streamline-potential grids provided higher degrees of accuracy compared to uniform Cartesian grids of similar resolution for their test cases. More general curvilinear grids were investigated by Castellini et al. (2000), He et al. (2002), and He and Durlofsky (2006).

The use of irregular grids requires specialized schemes for transmissibility calculations. Under such circumstances, it is important to develop appropriate upscaling algorithms that can link fine-scale geocellular models, which are defined on regular grids, and the coarse-scale models on irregular grids. Only limited work has been reported in the literature for upscaling on non-Cartesian grids. Wen et al. (2003a) investigated the upscaling of channel systems in two dimensions using flow-based grids and full-tensor upscaling methods. He et al. (2002) developed a mixed finite element method for upscaling to general quadrilateral grids. The work of Wen et al. (2003a) and He et al. (2002) presented approaches to obtain equivalent permeability tensors for irregular quadrilateral grids.

Researchers have also studied upscaling for more geometrically complex grids, such as hexahedral grids in three dimensions and unstructured perpendicular bisector grids. He and Durlofsky (2006) investigated flow-based grid generation and upscaling for three dimensional structured grids. They developed various flow-based gridding techniques including a streamline-based method, an elliptic grid generation approach, and an optimization method. They also implemented local and global upscaling techniques associated with the gridding approaches. Prevost et al. (2005) studied gridding and upscaling techniques for three-dimensional unstructured grids. Wu et al.

(2007) developed a global upscaling method to model complex features such as faults and pinch-out zones with unstructured grids.

Non-Cartesian grids add complexity to upscaling and discretization. Due to the fact that the fine-scale grids and coarse-scale grids are not aligned exactly, irregular grids require specialized methods for flux integration along the coarse-scale block interface and the calculation of equivalent pressures. Ding (2003) proposed approaches to calculate the flux along coarse-block faces to overcome this grid misalignment issue in corner-point grids. Another difficulty is that grid nonorthogonality errors may be significant if two-point flux schemes are used for non-Cartesian grids. In general, multipoint flux approximations as discussed in Section 1.1.2 will be required.

1.2 Scope of this Work

Our objective in this work is to extend existing upscaling capabilities to provide more accurate coarse-scale models while accommodating general permeability anisotropy and irregular quadrilateral grids. We propose a new class of transmissibility upscaling methods on general quadrilateral grids. The methods are designed to accurately represent full-tensor anisotropy and to capture important large-scale connected flow paths, such as channels in fluvial systems. To fulfill this objective, we extend VCMP upscaling procedures in three important directions. Specifically, we (1) develop global VCMP methods, (2) develop adaptive local-global VCMP techniques, and (3) apply VCMP (including extended local, global, and local-global versions) to general quadrilateral grids.

The upscaling techniques proposed in this dissertation extend existing procedures in important directions. Previous global transmissibility upscaling methodologies (e.g., Chen et al., 2008; Holden and Nielsen, 2000; Mallison et al., 2006; Zhang et al., 2008) and local-global transmissibility upscaling approaches (Chen and Durlofsky,

2006; Chen et al., 2003; Gerritsen and Lambers, 2008; Wen et al., 2006) were presented within the context of TPFA, so they can lose accuracy when full-tensor effects are significant. Similarly, although full-tensor permeability upscaling on irregular grids has been presented (He and Durlofsky, 2006; He et al., 2002; Wen et al., 2003a), existing techniques for transmissibility upscaling on general quadrilateral grids are based on two-point fluxes. Thus, we believe this work presents the first global transmissibility upscaling procedure that generates multipoint flux approximations and the first transmissibility upscaling procedure that generates multipoint flux approximations for irregular quadrilateral grids. This work also proposes the first coupling of adaptive local-global upscaling to a multipoint flux approximation.

Two global approaches within the VCMP upscaling procedure are considered – one in which the upscaled model is determined directly (VCMP-DG) and one in which iteration of the coarse-scale model is used to minimize the mismatch between coarse-scale fluxes and integrated fine-scale fluxes (VCMP-IG). The iterative global approach has been shown to effectively reduce flux errors in TPFA upscaling methods, and we show that the synthesis of global iterations with VCMP leads to a robust, accurate and efficient transmissibility upscaling method. We apply the M-fix as suggested by Gerritsen et al. (2006) and Lambers et al. (2008), but only when solutions are found to be nonmonotone.

We also present a local-global version of VCMP, called VCMP-ALG. VCMP-ALG incorporates global information while retaining computational efficiency. To the author's best knowledge, no work has been reported on local-global upscaling for non-Cartesian grids. In this work, we extend the local-global upscaling method to general quadrilateral grids with both TPFA and VCMP transmissibility calculations. VCMP-ALG is demonstrated to be accurate and computationally efficient.

A complete list of the various strategies designed, implemented, and tested in this dissertation is given in Table 1.1. Among these upscaling algorithms, extended local,

direct global, iterative global, and adaptive local-global, all of which use a two-point flux approximation, are existing methods used for comparison. VCMP combined with extended-local upscaling (VCMP-EL) was developed by Lambers et al. (2008) on uniform Cartesian and adapted Cartesian grids, and modified here for general quadrilateral grids. The combinations of VCMP with global, iterative global, and adaptive local-global upscaling are new upscaling strategies.

Table 1.1: Upscaling algorithms and their abbreviations

Abbreviation	Description
TPFA-EL	TPFA extended local
TPFA-DG	TPFA direct global
TPFA-IG	TPFA iterative global
TPFA-ALG	TPFA adaptive local-global
VCMP-EL	VCMP extended local
VCMP-DG	VCMP direct global
VCMP-IG	VCMP iterative global
VCMP-ALG	VCMP adaptive local-global

In the extension of VCMP to general quadrilateral grids, we do not align the underlying computational grid with the flow, nor with the geology, and instead focus on the development of various upscaling methods that are essentially independent of any particular gridding strategy. It is clear from the discussion above that the accuracy of the upscaled model can be improved through the use of specialized gridding techniques. However, gridding itself is a very broad area of research and we do not always have grids with favorable features. Therefore, the aim of this work is to design robust and accurate upscaling methods that are applicable for any given irregular grid. We intend to achieve reasonable upscaling accuracy even for grids with poor quality. The insensitivity of upscaling accuracy to grids offered by our methods gives flexibility in gridding and can therefore simplify gridding strategies.

All of our examples involve steady-state incompressible flow in two spatial dimensions. We present most simulation results in terms of single-phase flow. The simplified form of the single-phase pressure equation allows us to understand the performance and basic properties of the various schemes. The methodologies presented here are not, however, limited to single-phase flow and can be directly applied to the multiphase flow case. High accuracy for single-phase flow is a key requirement for accuracy in upscaled multiphase flow problems. The need for accurate upscaled transmissibilities in two-phase (oil-water) systems is well documented in previous papers (e.g., Chen et al., 2003; Wen et al., 2006; Zhang et al., 2008). In Chapter 3, we demonstrate that the VCMP transmissibilities computed from single-phase flow computations are appropriate for use in two-phase flow simulations.

The global VCMP upscaling methods and local-global VCMP approaches proposed in this work involve fine-scale or coarse-scale global solutions, and thus require a certain amount of computation. However, the upscaling process (in which a steady-state single-phase flow problem is solved) only needs to be done once, assuming the well configurations are not changed considerably, while the actual flow problems, which are usually multiphase flow, are solved for many time steps. Therefore, the computational savings are significant when multiphase flow simulations are performed on the coarse-scale model.

We note that extension of the upscaling procedures presented here to three dimensions is fairly straightforward. Extension of VCMP extended local methods to three dimensions is demonstrated in Lambers and Gerritsen (2008). Wen et al. (2006) presented a three-dimensional version of TPFA-ALG. We also note that upscaling in the vicinity of wells is not considered in this dissertation; however, the methodologies developed here can be combined with near-well upscaling reported by Durlofsky et al. (2000), Hui and Durlofsky (2005), and Chen and Durlofsky (2006), among others.

1.3 Dissertation Outline

This dissertation proceeds as follows. We present the methodologies and simulation results for the new upscaling methodologies, global VCMP techniques and local-global VCMP procedures, in Chapters 2 and 3, respectively. Extensions of VCMP methods to general polygonal grids are presented in Chapter 4. Finally, we offer conclusions and suggest future directions in Chapter 5. More details on each chapter are given below.

Chapter 2 shows the methodology and results of VCMP global or iterative global upscaling for highly heterogeneous models with Cartesian and irregular quadrilateral grids. First, we present the governing pressure equation and review local and extended local upscaling, TPFA discretization schemes, and the VCMP method. Then, we consider global upscaling and describe the use of VCMP within this context. Both direct global (VCMP-DG) and iterative global (VCMP-IG) methods are developed. Extensive numerical results are presented. We consider multiple realizations of oriented Gaussian and channelized permeability fields, with flow driven by several different boundary specifications, and regular and irregular grids. The enhanced accuracy of our new procedures is clearly illustrated.

A VCMP-ALG technique is proposed in Chapter 3. We present the methodology, discuss implementation issues, and provide results for VCMP adaptive local-global upscaling. VCMP-ALG is distinguished from VCMP-DG through the use of local boundary conditions determined from interpolating coarse-scale solutions rather than from global fine-scale solutions. Thus a key step in ALG methods is the pressure interpolation. Here, a triangle-based linear interpolation is used to find pressure boundary conditions. We present single-phase and two-phase simulation results for challenging (oriented) two-dimensional systems that demonstrate the accuracy and capabilities of the method. The performance of VCMP-ALG methods on both regular

and irregular quadrilateral grids is shown. Comparisons between VCMP-ALG, TPFA-ALG, VCMP-EL, and VCMP-DG are presented.

In Chapter 4, upscaling methods are extended to unstructured grids for geological models with pinch-outs. The capability of our proposed methods is studied for complex grids other than quadrilateral grids. One of the key challenges is the definition of VCMP interaction regions. Results for oriented layered systems, with both constant layer permeabilities and heterogeneous layer permeabilities, demonstrate the improved accuracy attained by VCMP methods relative to their TPFA counterparts.

Finally, Chapter 5 summarizes our key findings and gives some ideas for future research directions.

Chapter 2

VCMP Global Methods

In this chapter and the following chapter, we propose new transmissibility upscaling procedures to accurately capture full-tensor effects and large-scale permeability connectivity in the coarse simulation model. These techniques are based on variable compact multipoint flux approximations. Specifically, in this chapter, we develop global VCMP techniques and apply them to Cartesian and irregular quadrilateral grids. Two approaches for including global flow information within the VCMP upscaling procedure are considered. One is VCMP-DG, in which the upscaled model is determined directly from the global fine-scale solution. The other is VCMP-IG, in which upscaled transmissibilities are adjusted iteratively to match integrated fine-scale fluxes.

2.1 Local and Extended Local Upscaling Methods

2.1.1 Single-phase Pressure Equation

We consider steady-state incompressible single-phase flow in the absence of gravity and source terms. The governing dimensionless fine-scale pressure equation derives

from Darcy's law ($u = -k \cdot \nabla p$) combined with mass conservation for an incompressible system ($\nabla \cdot u = 0$), with u being the Darcy velocity and p the pressure. The pressure equation is then given as

$$\nabla \cdot (k \cdot \nabla p) = 0. \tag{2.1}$$

For a two-dimensional system characterized by a diagonal tensor permeability, with $k = diag(k_x, k_y)$, the finite volume discretization of Eq. (2.1) can be written as

$$\begin{aligned} &(T_x)_{i-1/2,j}\,(p_{i-1,j} - p_{i,j}) + (T_x)_{i+1/2,j}\,(p_{i+1,j} - p_{i,j}) \\ &+ (T_y)_{i,j-1/2}\,(p_{i,j-1} - p_{i,j}) + (T_y)_{i,j+1/2}\,(p_{i,j+1} - p_{i,j}) = 0, \end{aligned} \tag{2.2}$$

where the subscripts denote grid blocks (e.g., (i, j)) or interface (e.g., $(i - 1/2, j)$). T_x and T_y are the interblock transmissibilities in the x and y directions, respectively. They are defined as

$$(T_x)_{i+1/2,j} = \frac{2\,(k_x)_{i+1/2,j}\,\Delta y_j H}{\Delta x_{i+1} + \Delta x_i}, \qquad (T_y)_{i,j+1/2} = \frac{2\,(k_y)_{i,j+1/2}\,\Delta x_i H}{\Delta y_{j+1} + \Delta y_j}, \tag{2.3}$$

where H is the model thickness, Δx and Δy are grid block sizes, and $(k_x)_{i+1/2,j}$ is the interblock permeability computed from the weighted harmonic average of $(k_x)_i$ and $(k_x)_{i+1}$, i.e.,

$$(k_x)_{i+1/2,j} = \frac{(\Delta x_i + \Delta x_{i+1})\,(k_x)_{i,j}(k_x)_{i+1,j}}{\Delta x_{i+1}(k_x)_{i,j} + \Delta x_i (k_x)_{i+1,j}}. \tag{2.4}$$

We solve Eq. (2.2) with imposed constant pressure or no-flow boundary conditions. This leads to a system of equations in the form of $Ap = b$, where A includes the transmissibilities and the coefficients from boundary conditions, p are the unknown pressures, and b contains boundary conditions.

Upscaling is required because k varies over a wide range of spatial scales. The

coarse-scale pressure equation is of the same form as Eq. (2.1), with k replaced by k^*. The discretization scheme in Eq. (2.2) can also be applied to the coarse-scale pressure equation when two-point flux approximations are used. However, the discretization is more complex when multipoint flux approximations are introduced to model full-tensor effects in the coarse scale. More discussion of this issue is given below. Our upscaling computations involve the solution of Eq. (2.1) over a particular domain, and the subsequent determination of upscaled parameters (k^* or T^*) from appropriate integration of u and p.

2.1.2 Coarse Models with Two-Point Flux Approximations

We now discuss the use of local or extended local (EL) transmissibility upscaling to provide coarse models described by TPFA. This requires the solution of Eq. (2.1) in a local or extended local fine-scale region, as illustrated in Figure 1.2. Constant-pressure boundary conditions are imposed at the inlet and outlet, and no-flow boundary conditions are prescribed on the remaining boundaries (other boundary specifications are also possible). Assuming that the flux is related only to the pressures of the two cells adjacent to the face (Figure 2.1), we compute an upscaled transmissibility as

$$T^* = \frac{f^c}{p_1^c - p_2^c}, \tag{2.5}$$

where T^* is the TPFA upscaled transmissibility and $p_1^c = \langle p \rangle_1$ and $p_2^c = \langle p \rangle_2$ represent the area-averages of the fine-scale pressures over the regions corresponding to the two coarse cells. The flux across the region corresponding to the coarse-cell face, f^c, is obtained by integrating the fine-scale fluxes over the face; i.e., we compute $\int_l u \cdot n \, dl$, where l designates the coarse-cell face and n is the unit normal to the face. When the coarse and fine grids are not aligned, a linear interpolation of the components of u in the appropriate fine-scale cell is used to determine u along the face.

The above description is for a local flow in the x-direction. A similar procedure is applied to compute the transmissibility in the y-direction, using a local flow problem driven by a pressure difference in y. These transmissibilities can then be used in Eq. (2.2), which enables us to solve for pressure on the coarse scale.

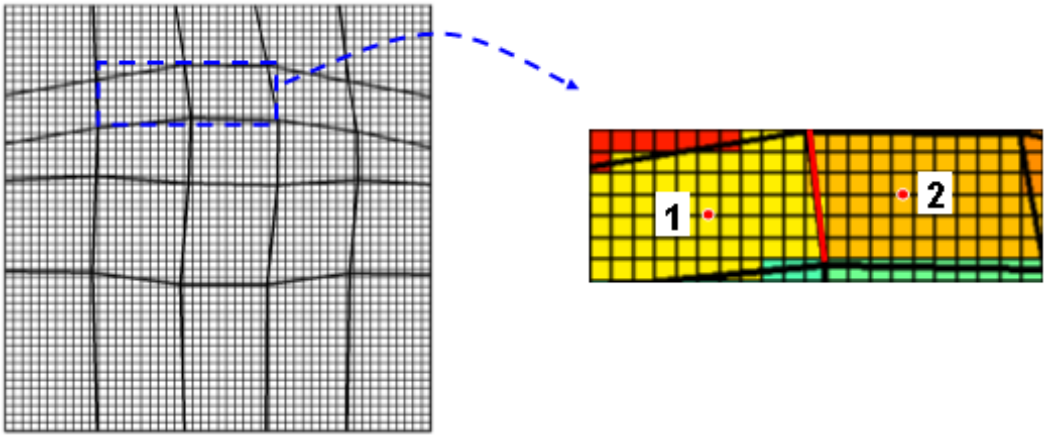

Figure 2.1: The red dots denote the centers of a quadrilateral grid that are used to construct a two-point flux approximation to the flux across a face, indicated by the thick red line.

2.1.3 Coarse Models with Variable Compact Multipoint Flux Methods

The two-point flux approximation may lead to large upscaling errors if there is strong anisotropy. To obtain an accurate representation of full-tensor permeability anisotropy, a transmissibility upscaling method for multipoint flux approximations was developed in Lambers et al. (2008). The stencil of this variable compact multipoint flux approximation (VCMP) is allowed to vary from cell to cell.

In contrast to TPFA, the transmissibility approximations include not just two but

up to six averaged pressure values, as illustrated in Figure 2.2. Thus,

$$f^c = -t^T p^c, \tag{2.6}$$

where t is the transmissibility vector, $t = [t_1, t_2, ..., t_6]^T$, and $p^c = [p_1^c, p_2^c, ..., p_6^c]^T$ (note that we use lower case t here to distinguish these MPFA transmissibilities from TPFA transmissibilities and that, although these t_i are upscaled quantities, we drop the $*$ superscript for conciseness). The t_i are computed to honor closely the fluxes across the coarse-cell face of two generic flow problems on the extended local region, one in each coordinate direction, and to lead, when possible, to a two-point flux approximation. Additional and necessary constraints on the t_i and their signs are imposed for consistency. We find a solution by solving the optimization problem

$$\min_t \sum_{i=1}^{2} \alpha_i^2 |t^T p_i^c + f_i^c|^2 + \sum_{j=3}^{6} \beta_j^2 t_j^2, \tag{2.7}$$

under the linear constraints

$$\sum_{j=1}^{6} t_j = 0, \qquad t_{2j-1} \leq 0, \qquad t_{2j} \geq 0, \qquad j = 1, 2, 3. \tag{2.8}$$

The weights α_i and β_j in VCMP-EL are free to be chosen. Here, we elect to take them as $|f_i^c|$ and $(|f_1^c| + |f_2^c|)/M$, respectively, where M is a tuning parameter. Large values of M lead to transmissibility weights that better resolve the two local flows, while small values of M drive the method toward a TPFA representation. Here, we use $M = 1000$ to emphasize accuracy. The resulting VCMP stencils vary from cell to cell in terms of the number of points included and the values of the corresponding transmissibility weights.

Equating the sum of the fluxes across all faces of each coarse cell, so as to honor Eq. (2.1), leads to the matrix-vector equation $Ap = b$. Here, the elements of A depend

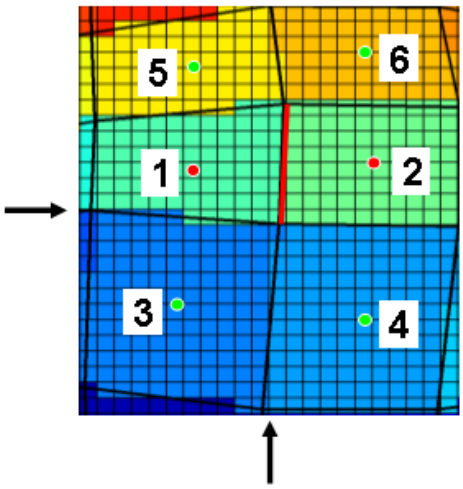

Figure 2.2: The red dots denote the centers of quadrilateral grid blocks that are used to construct a VCMP approximation to the flux across a face, indicated by the thick red line.

on the transmissibility weights.

As discussed in the Introduction, unlike TPFA, MPFA methods do not necessarily lead to a monotone pressure field. In Gerritsen et al. (2006) it was therefore suggested to apply a correction to the matrix elements of A to make it an M-matrix, hence guaranteeing monotonicity. Specifically, for A to be an M-matrix, we must have

$$a_{k,k} > 0, \quad \forall k, \tag{2.9}$$

$$a_{k,l} \leq 0, \quad \forall k, l, \quad k \neq l, \tag{2.10}$$

and the row sums must satisfy

$$\sum_l a_{k,l} \geq 0, \quad \forall k, \tag{2.11}$$

with strict inequality for at least one row. Thanks to the sign constraints imposed on the weights, the diagonal elements of A are already guaranteed to be positive, so

Eq. (2.9) is automatically satisfied.

If we can ensure that Eq. (2.10) is also satisfied, then the condition in Eq. (2.11) is satisfied as well. The first condition in Eq. (2.8) implies that the row sum will be zero if row k corresponds to a cell without boundary faces, and positive for a cell with a boundary face, because, in view of the inequality constraints in Eq. (2.8), only negative contributions to matrix elements will be omitted due to the boundary conditions.

Therefore, we only have to fix the wrongly-signed off-diagonal elements to obtain an M-matrix. Each off-diagonal element of A is composed of nonnegative and nonpositive transmissibilities and can be written as:

$$a_{kl} = \sum_{j=1}^{m_{kl}^+} t_{j,kl}^+ + \sum_{j=1}^{m_{kl}^-} t_{j,kl}^-, \tag{2.12}$$

where each $t_{j,kl}^+ \geq 0$ and each $t_{j,kl}^- \leq 0$. Let $\tilde{a}_{kl}$ be the (k,l) entry of the updated matrix $\tilde{A}$. To guarantee that $\tilde{A}$ is an M-matrix, we impose the constraints

$$|\tilde{t}_{j,kl}^-| \geq |t_{j,kl}^-|, \qquad |\tilde{t}_{j,kl}^+| \leq \frac{1}{m_{kl}^+} \left(\sum_{j=1}^{m_{kl}^+} |t_{j,kl}^-| \right), \tag{2.13}$$

in addition to Eq. (2.8), and then recompute t_j. This predictor-corrector step is called the M-fix.

It is important to note that we can guarantee monotonicity for all possible boundary conditions by imposing the M-fix on the matrix resulting for Dirichlet boundary conditions on the entire boundary. This is due to the fact that for any face on which Neumann boundary conditions are imposed, potential positive contributions to off-diagonal elements are not included in Eq. (2.13), whereas such stencils are included in the analysis when only Dirichlet boundary conditions are imposed.

In our implementation, we do not indiscriminately apply the M-fix. The above

M-fix constraints, which are sufficient but not always necessary to guarantee monotonicity, can affect upscaling accuracy in some cases. Therefore, we choose to only apply the M-fix when the computed solutions are indeed nonmonotone. We refer to this as the selective M-fix.

2.1.4 Algorithms for VCMP-Local and VCMP-EL

The algorithms for VCMP combined with local (VCMP-local) and extended local (VCMP-EL) upscaling are given as follows:

1. For each face of the coarse grid, define a fine-scale local or extended local region. The local region for VCMP methods is the smallest rectangle containing the six coarse cells surrounding the face, shown in Figure 2.2. For VCMP-EL, we add one coarse-scale cell along the dimension that is approximately perpendicular to the face.

2. Solve two local fine-scale flows (Eq. (2.1)) with two sets of generic boundary conditions on the local regions: constant pressure in one coordinate direction and no-flow in the other coordinate direction.

3. Find the six coarse-scale pressure values, p^c, and coarse-scale fluxes on the face, f^c, from these local fine-scale solutions through averaging and integration, respectively.

4. Solve the optimization problem (Eq. (2.7)) with the constraints in Eq. (2.8) to compute VCMP transmissibility vectors, $t = [t_1, t_2, ..., t_6]^T$. In the rare case that the optimization problem cannot be solved, we simply use two-point flux solutions, described in Eq. (2.5), as substitutes.

5. Once transmissibilities are determined for each coarse-grid face, solve the coarse-scale pressure equation. Check if the pressure solution is monotone and apply

the M-fix if necessary.

2.2 Global and Iterative Global Upscaling

Global upscaling approaches use a fine-scale global solution to determine transmissibilities for coarse-scale faces. They generally provide better upscaling accuracy than (extended) local methods because connectivities at scales larger than the (extended) local regions are now included in the transmissibility calculations. The price to pay for this increased accuracy is the global solution on the geocellular grid. As compared to the full multiphase reservoir simulation, however, the computational costs associated with this solution may be acceptable.

In direct global upscaling with the two-point flux approximation, which we refer to as TPFA-DG, a fine-scale flow problem is solved over a global region. The imposed boundary conditions may be either generic (e.g., $p = 1$ at the left boundary, $p = 0$ at the right boundary, no-flow elsewhere) or they may mimic those to be used in the eventual multiphase flow simulations. Following the flow solution, the coarse-scale transmissibilities are calculated directly from Eq. (2.5). This approach does not guarantee that all T^* will be positive, and in the general case some number of negative T^* will occur. When a $T^* < 0$ is observed, we replace it with T^* computed using the TPFA-EL method. This replacement of negative transmissibilities, however, acts to reduce upscaling accuracy. If there are very few (or zero) negative T^*, TPFA-DG tends to give highly accurate approximations to the averaged fine-scale solutions.

Other strategies also exist for eliminating negative transmissibilities, and these can provide better accuracy than the use of TPFA-EL. One such approach, referred to as TPFA-IG (iterative global), iteratively adjusts the T^* from TPFA-DG using global coarse-scale solutions (Chen et al., 2008). The goal of TPFA-IG is to match the fluxes from the global fine-scale reference solution. Designating the integrated

global fine-scale flux for a particular coarse-scale interface as f_G, TPFA-IG computes the upscaled transmissibility for this interface at the next iteration as

$$(T^*)^{\nu+1} = \frac{f_G}{(p^c)_1^\nu - (p^c)_2^\nu}, \tag{2.14}$$

where $(p^c)_1^\nu$ and $(p^c)_2^\nu$ represent the coarse-block pressures in the two cells sharing the target interface at the previous iteration (ν). TPFA-IG can provide highly accurate flux approximations, but some accuracy in the coarse-scale pressure is generally lost in the iterative process, as the goal of the procedure is to match fluxes, not pressures.

As indicated earlier, previous global transmissibility upscaling procedures rely on TPFA approximations. Our goal here is to incorporate MPFA (specifically VCMP) into global upscaling. This should lead to better accuracy, particularly in cases with strong full-tensor effects. Here, we propose two new algorithms that generalize their TPFA counterparts: VCMP-DG (direct global) and VCMP-IG (iterative global). Although the methods vary in terms of computational cost, coding effort and accuracy, both are suitable for upscaling of heterogeneous permeability fields with full-tensor anisotropy.

As discussed in Section 2.1.3, VCMP requires two flow solutions. In our first implementation of VCMP with global flow information, we used two fine-scale global flows with generic boundary conditions: one with a linear pressure drop in the x-direction and one with a pressure drop in the y-direction. However, we observed that in some cases these two global flows did not provide sufficiently dissimilar local flows. This is especially true in strongly channelized systems. Also, the transmissibilities computed in this way did not lead to high accuracy for flow problems driven by other global boundary conditions. In our current implementation, we first perform a single global fine-scale flow simulation (the boundary conditions used for this solution could correspond to those to be used for the eventual multiphase flow simulations). For

each coarse face, we then choose a complementary local fine-scale flow. This local flow is driven by a pressure gradient that is approximately orthogonal to the pressure gradient imposed by the global flow. The two flows thus provide complementary information that is used to construct the VCMP stencil. The VCMP-DG and VCMP-IG algorithms are outlined below.

2.2.1 Algorithm for VCMP-DG

Combining direct global upscaling with VCMP leads to the following algorithm:

1. Solve a global fine-scale flow problem with specified boundary conditions. Determine coarse-scale pressure, p_G, and flux, f_G.

2. For each face of a coarse-scale grid, calculate the averaged pressure gradients, $[\partial p_G/\partial x, \partial p_G/\partial y]$, across the extended region. Select a complementary local fine-scale flow with pressure gradients $[\partial p_L/\partial x, \partial p_L/\partial y] = [-\partial p_G/\partial y, \partial p_G/\partial x]$, and solve it. Determine coarse-scale p_L and f_L.

3. Solve the optimization problem (Eq. (2.7)) honoring the two flows (p_G and f_G, p_L and f_L), with the constraints in Eq. (2.8), to find the VCMP transmissibility, $t = [t_1, t_2, ..., t_6]^T$. In the rare case that the optimization problem cannot be solved, we use the transmissibility from a VCMP-EL method as a substitute.

4. Check if the pressure solution is monotone. If not, find the wrongly-signed elements in A, and recompute the transmissibilities across the contributing faces using the additional M-fix constraints in Eq. (2.13).

2.2.2 Algorithm for VCMP-IG

Combining VCMP with iterative global upscaling (Chen et al., 2008) leads to the algorithm:

1. Solve a global fine-scale flow problem with specified boundary conditions. Compute the coarse-scale pressure, p_G^0, and flux, f_G, to be used in the transmissibility calculations. Here f_G is the global reference solution that VCMP-IG pursues by adjusting coarse-scale transmissibilities.

   Set the iteration number $\nu = 0$.

2. For each face of a coarse-scale grid, solve a local fine-scale flow complementary to the global flow, as described in step 2 of the VCMP-DG algorithm. The solution of this local flow is denoted as p_L^ν and f_L^ν.

3. Solve the optimization problem (Eq. (2.7)) honoring the two flows (p_G^ν and f_G, p_L^ν and f_L^ν), with the constraints in Eq. (2.8), to find the VCMP transmissibility, $t^{\nu+1} = [t_1^{\nu+1}, t_2^{\nu+1}, ..., t_6^{\nu+1}]^T$. When the optimization problem cannot be solved, $t^{\nu+1}$ is replaced by the transmissibility from the last iteration t^ν. For the initial step $\nu = 0$, t^0 is calculated from a VCMP-EL method.

4. Check if the pressure solution is monotone. If not, find the wrongly-signed elements in A, and obtain the recomputed transmissibilities, $t^{\nu+1}$, across the contributing faces using the additional M-fix constraints in Eq. (2.13).

5. Using $t^{\nu+1}$, solve global coarse-scale flow problems, with the same specified boundary conditions as used in step 1, to obtain a coarse-scale pressure solution, and assign it to $p_G^{\nu+1}$.

6. If not converged, set $\nu = \nu + 1$ and iterate through steps 2-5.

The convergence criteria are based on the difference between the VCMP-IG solution and the reference fine-scale solution or the change in the VCMP-IG solution

between iterations. For the results shown in Sections 2.4 and 2.5, the following criterion is used. We stop the iteration if

$$\max\left(\frac{\parallel p_G^{\nu} - p_G^{\nu-1} \parallel_2}{\parallel p_G^{\nu} \parallel_2}, \frac{\mid (Q^c)^{\nu} - (Q^c)^{\nu-1} \mid}{\mid (Q^c)^{\nu} \mid}\right) \leq 0.01, \tag{2.15}$$

where ν is an iteration counter, Q^c is the total flow rate at the boundary from the coarse-scale model, and p_G is coarse-scale pressure. In most cases, it takes $3-5$ iterations to converge. Fast error reduction is achieved in the initial two iterations. Since iterative global upscaling methods are designed to enhance accuracy in fluxes (while usually resulting in accuracy reduction in pressures), different convergence criteria can be chosen depending on the choice of error tolerance for fluxes and pressures.

VCMP global upscaling methods are similar to VCMP-EL except for the flow problems to be honored. VCMP global methods use one global flow and one complementary local flow, while VCMP-EL uses two generic local flows. The parameter α, introduced in Eq. (2.7), is defined differently for the local versus global methods. For VCMP-EL, the two local flows are weighted based on their flow rates. In VCMP-DG and VCMP-IG, $\alpha_G = n \times |f_L/f_G|$ and $\alpha_L = 1$ such that the global flow is honored more than the local flow. Here n is a number between one (weighting the global and local flows equally in the optimization procedure) and infinity (only using the global flow), which can be tuned for different geologies. Large values of n give high accuracy for the global flow used to compute upscaled transmissibility, while small values of n provide more robustness in the upscaled model as the resulting VCMP transmissibility takes into account the two dissimilar flows equally in the optimization procedure. Results are not highly sensitive to n, though this parameter can have an impact on accuracy. In the results below, for log-normally distributed permeability fields we use $n = 5$ and for channelized models we use $n = 20$. Even though this weights the global flow much more than the local complementary flow, the resulting solutions

from VCMP global methods were found to be more robust than TPFA global methods due to the extra information provided by the local flow and the flexible multipoint character of VCMP.

2.3 Test Suite

Our test suite consists of two types of fine-scale permeability fields:

- Twenty-five realizations of log-normally distributed permeability fields, generated by sequential Gaussian simulation (Deutsch and Journel, 1998). All log-normal cases have dimension 100×100 on a unit square. The dimensionless correlation lengths are $\lambda_1 = 0.5$ and $\lambda_2 = 0.02$. The variance of $\log k$ is 3.0 and the mean is also 3.0. The direction of the long correlation is misaligned with the grid with an angle θ, relative to the x axis. This misalignment results in permeability anisotropy in the coarse-scale model, meaning that full-tensor effects are expected to be important when θ differs appreciably from zero. In the base case, we use $\theta = 30^\circ$. Figure 2.4(a) shows a typical realization. All realizations are upscaled to 10×10 coarse grids that are either Cartesian or general quadrilateral grids. We also studied variants of the base case with different layering orientations, e.g., $\theta = 45^\circ$, and different coarse-grid aspect ratios. We additionally investigated the process dependency of the various upscaling methods.

- Fifty channelized layers from the SPE 10 Comparative Solution Project (Christie and Blunt, 2001). The permeability field of a typical channelized layer is presented in Figure 2.4(b). The fine grids are of dimension 220×60, with $\Delta x = 10$ and $\Delta y = 20$. The models are upscaled to 22×6 coarse grids that are either Cartesian or general quadrilateral grids.

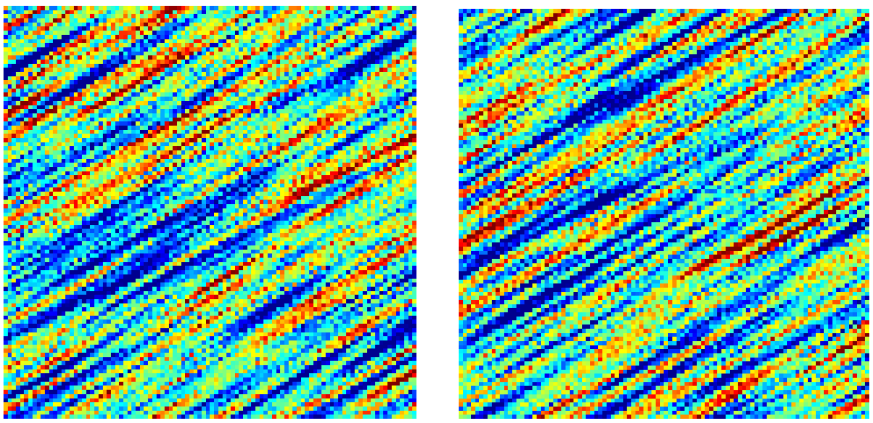

(a) Realization 1

(b) Realization 2

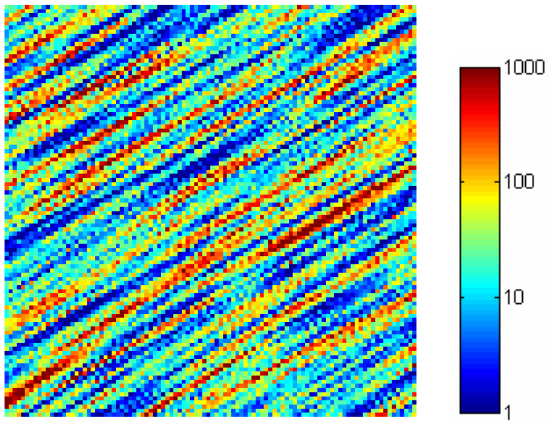

(c) Realization 3

Figure 2.3: Three realizations of log-normally distributed permeability fields with correlation lengths $\lambda_1 = 0.5$ and $\lambda_2 = 0.02$. The long correlation direction is oriented at 30° to the x-axis.

On these fields we apply all VCMP type methods (VCMP-EL, VCMP-DG and VCMP-IG) and their TPFA analogs (TPFA-EL, TPFA-DG and TPFA-IG). The size of the border regions used in TPFA-EL is as shown in Figure 1.2. The border regions for VCMP-EL are the same so the results are directly comparable.

We consider both uniform Cartesian grids and irregular grids. Starting with a uniform grid with node spacings Δx_c and Δy_c, the coarse irregular grids are generated by perturbing each node in the x-direction by $\xi \Delta x_c$ and in the y-direction

by $\xi \Delta y_c$, where ξ is a random number within $[-0.3, 0.3]$. The boundary nodes are limited to move in only one direction. Examples of these grids are illustrated in Figure 2.4. When these grids are applied, a different random grid is generated for each permeability realization.

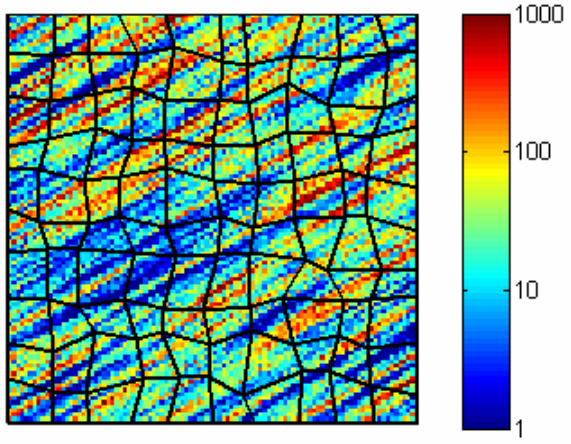

(a) Log normal permeability

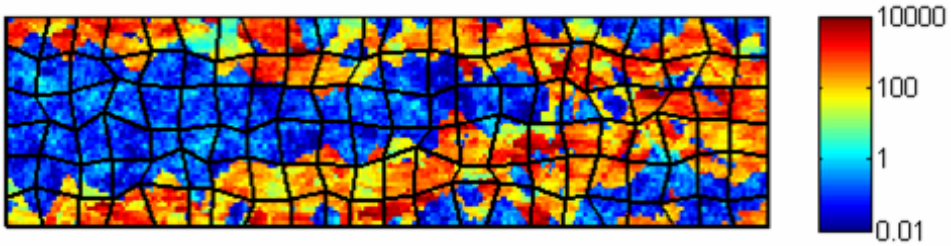

(b) Channelized permeability

Figure 2.4: Fine-scale permeability fields and random grids for (a) log-normally distributed permeability realization with correlation lengths $\lambda_1 = 0.5$ and $\lambda_2 = 0.02$ and a layering orientation angle $\theta = 30°$ and (b) channelized layer (layer 44 from SPE 10).

For each permeability field and each grid, we solve the pressure equation with four sets of boundary conditions:

- Constant pressure/no-flow boundary conditions in the x and y-directions, respectively. For the x-direction flow, we set $p(0, y) = 1$, $p(L_x, y) = 0$, and

$u_y(x,0) = u_y(x,L_y) = 0$. For the y-direction flow, we set $p(x,0) = 1$, $p(x,L_y) = 0$, and $u_x(0,y) = u_x(L_x,y) = 0$. Here, L_x and L_y designate system lengths.

- Corner-to-corner flows. For example, for flow from the lower-left corner to the upper-right corner of a log-normal permeability field, we prescribe $p = 1$ for $0 \le y/L_y \le 0.2, x = 0$ and $0 \le x/L_x \le 0.2, y = 0$; $p = 0$ for $0.8 \le y/L_y \le 1, x = L_x$ and $0.8 \le x/L_x \le 1, y = L_y$ and no-flow conditions elsewhere. This boundary condition is also called "along layering" flow because it is aligned with the layer orientation of the log-normally distributed permeability fields. The boundary conditions for flow from the upper-left corner to the lower-right corner are defined similarly. This is called "across layering" flow. Figure 2.5 shows these two boundary conditions. For channelized layers, we define "along layering" and "across layering" flows similarly, except that we fix pressure over two coarse-scale cells instead of over the x and y-ranges given above.

A variant on lower-left to upper-right flow is introduced to assess process dependency. For this case we prescribe $p = 1$ for $0 \le y/L_y \le 0.5, x = 0$; $p = 0$ for $0.5 \le y/L_y \le 1, x = L_x$ and no-flow conditions elsewhere. This scenario is referred to as "corner flow" and is used on log-normal permeability models.

Unless otherwise stated, in the tables below we report the average relative errors for total flow rate through the system (E_Q) and L_2 flux and pressure errors (E_f and E_p) for the upscaled models averaged over all realizations. All errors are computed relative to the reference fine-scale solutions. The errors are defined as:

$$E_Q = \frac{|Q - Q_{ref}|}{|Q_{ref}|}, \qquad E_f = \frac{\|f - f_{ref}\|_2}{\|f_{ref}\|_2}, \qquad E_p = \frac{\|p - p_{ref}\|_2}{\|p_{ref}\|_2}, \tag{2.16}$$

where Q, f, and p designate the coarse-scale solutions and Q_{ref}, f_{ref} and p_{ref} are analogous quantities computed from the fine-scale solutions. Specifically, f_{ref} is obtained by integrating fine-scale fluxes along the face of each coarse cell and p_{ref} is

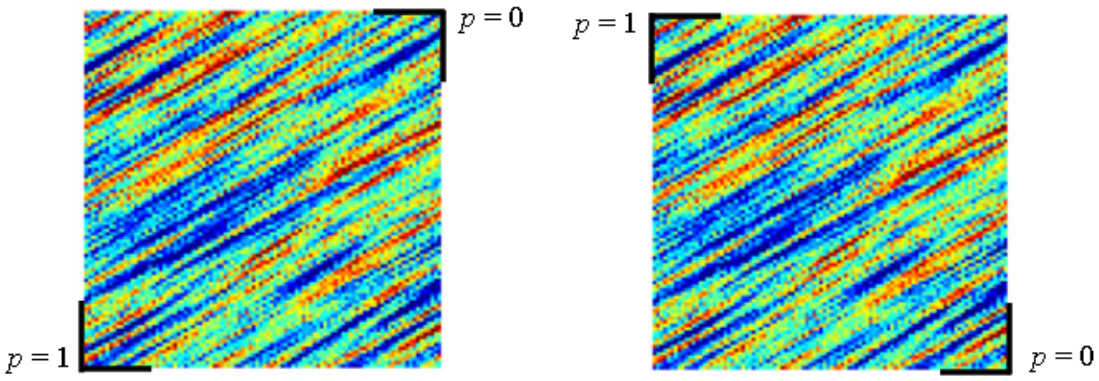

(a) Along layering flow (b) Across layering flow

Figure 2.5: Schematic showing boundary conditions: (a) along layering flow and (b) across layering flow.

computed as the area-weighted average of the fine-scale pressures corresponding to each coarse cell.

All results shown below are computed with the selective M-fix, unless otherwise stated. A comparison of the original M-fix with the selective M-fix is shown in 2.4.5.

2.4 Results for Log-normal Permeability Fields

We now present detailed upscaling results for log-normal permeability fields on Cartesian and irregular grids. VCMP-EL has already been demonstrated to be a promising approach for upscaling on Cartesian grids by Lambers et al. (2008). Here we include the results of VCMP-EL and TPFA-EL for completeness, though our emphasis is on the new upscaling strategies, VCMP-DG and VCMP-IG, and their performance relative to TPFA-DG and TPFA-IG.

2.4.1 Results for Cartesian Grids

Tables 2.1, 2.2, and 2.3 display the mean errors in the total flow rate, flux and pressure, respectively, using various upscaling methods for 25 realizations of the log-normal permeability fields with $\theta = 30°$. Results are reported for four sets of boundary conditions. We note first that TPFA-EL displays large errors, particularly for flow rate and flux, and these are reduced significantly through use of VCMP-EL. This is consistent with the results reported by Lambers et al. (2008). Note that the VCMP results in Lambers et al. (2008) may have unphysical oscillations because the monotonicity fix was not applied, while all results presented in this dissertation are oscillation free thanks to the use of the full M-fix or selective M-fix.

Next we compare VCMP global upscaling methods to their TPFA counterparts. We observe that VCMP-DG provides improvement over TPFA-DG for all quantities considered. In particular, VCMP-DG gives much more accurate results for flux and pressure than TPFA-DG, as indicated by the very small E_f (Table 2.2) and E_p (Table 2.3) values for all four boundary conditions.

TPFA-IG gives low errors for total flow rate and flux, though the flow rate and flux errors using VCMP-IG are generally even smaller. The pressure errors using TPFA-IG are larger than the pressure errors using TPFA-DG. This is as expected because, during the iterations, flux errors are minimized at the expense of pressure errors. Pressure errors using TPFA-IG are significant for x-direction and y-direction flows (E_p=0.165 and 0.130, respectively). These errors essentially vanish after applying VCMP-IG.

Because of the strong anisotropy in the coarse-scale models, which results from the oriented layering in the fine-scale permeability fields, accurate full-tensor upscaling is important for this case. For this reason, VCMP methods consistently outperform their TPFA analogs.

Among the VCMP-type methods, VCMP-EL shows the largest errors in total flow

rate, local flux, and local pressure. VCMP-DG and VCMP-IG both improve upon VCMP-EL because they incorporate global flow information in the upscaling process. VCMP-IG reduces the L_2 flux errors associated with VCMP-DG, but leads to larger errors in pressure, as expected. Overall, both VCMP-DG and VCMP-IG give small errors in both flux and pressure ($E_f \leq 0.010$ and $E_p \leq 0.012$).

The results presented in the tables can also be viewed on a realization-by-realization basis. We consider along layering flow. Figure 2.6 shows crossplots of coarse-scale flow rate versus fine-scale flow rate using all six upscaling methods for the 25 log-normally distributed permeability realizations. Perfect upscaling would result in all points falling on the 45° line. Here the TPFA-ALG method gives a large error (E_Q = 0.434 as shown in Table 2.1). The accuracy is greatly improved by VCMP-EL ($E_Q = 0.139$), though there is still a fair amount of scatter. Among the four global methods, TPFA-DG shows noticeable but small errors, while the other three methods (VCMP-DG, TPFA-IG, and VCMP-IG) provide high degrees of accuracy.

The L_2 flux errors presented in the tables above represent averages of all of the flux errors in a particular model (and the subsequent average over all 25 realizations). We now present face-by-face comparisons of flux for particular models. In Figures 2.7 and 2.8 we plot coarse-scale fluxes versus integrated fine-scale fluxes for x-direction flows for two layers. We compare results using TPFA-DG (Figures 2.7(a) and 2.8(a)) and VCMP-DG (Figures 2.7(b) and 2.8(b)). Figure 2.7 is for the layer with the largest L_2 flux error using TPFA-DG and Figure 2.8 is for the layer with L_2 flux error nearest the average value reported in Table 2.2. The improvement resulting from VCMP-DG, and the high level of accuracy of the VCMP-DG results, are clearly evident in both cases.

The above face-by-face comparisons of flux show that the magnitude of flux is well represented by VCMP-DG. We present velocity vector plots with velocity computed from TPFA-DG and VCMP-DG in Figure 2.9. We consider the same model as in

Table 2.1: Relative errors for total flow rate, E_Q, using various upscaling methods for 25 realizations of log-normal permeability fields with $\theta = 30°$, on 10×10 Cartesian grids.

Flow	TPFA-EL	VCMP-EL	TPFA-DG	VCMP-DG	TPFA-IG	VCMP-IG
In x-direction	0.103	0.047	0.057	0.00003	0.0006	0.00003
In y-direction	0.084	0.016	0.030	0.0002	0.0003	0.0002
Along layering	0.434	0.139	0.044	0.002	0.0001	0.001
Across layering	0.241	0.060	0.019	0.0001	0.0001	0.0001

Table 2.2: L_2 flux errors, E_f, using various upscaling methods for 25 realizations of log-normal permeability fields with $\theta = 30°$, on 10×10 Cartesian grids.

Flow	TPFA-EL	VCMP-EL	TPFA-DG	VCMP-DG	TPFA-IG	VCMP-IG
In x-direction	0.433	0.064	0.379	0.0003	0.026	0.0003
In y-direction	0.437	0.106	0.377	0.0009	0.026	0.0008
Along layering	0.519	0.236	0.204	0.010	0.007	0.005
Across layering	0.369	0.186	0.213	0.0004	0.016	0.0004

Table 2.3: L_2 pressure errors, E_p, using various upscaling methods for 25 realizations of log-normal permeability fields with $\theta = 30°$, on 10×10 Cartesian grids.

Flow	TPFA-EL	VCMP-EL	TPFA-DG	VCMP-DG	TPFA-IG	VCMP-IG
In x-direction	0.133	0.012	0.120	0.00004	0.165	0.0001
In y-direction	0.121	0.013	0.098	0.0001	0.130	0.0003
Along layering	0.113	0.074	0.063	0.004	0.074	0.012
Across layering	0.069	0.035	0.027	0.0001	0.038	0.0002

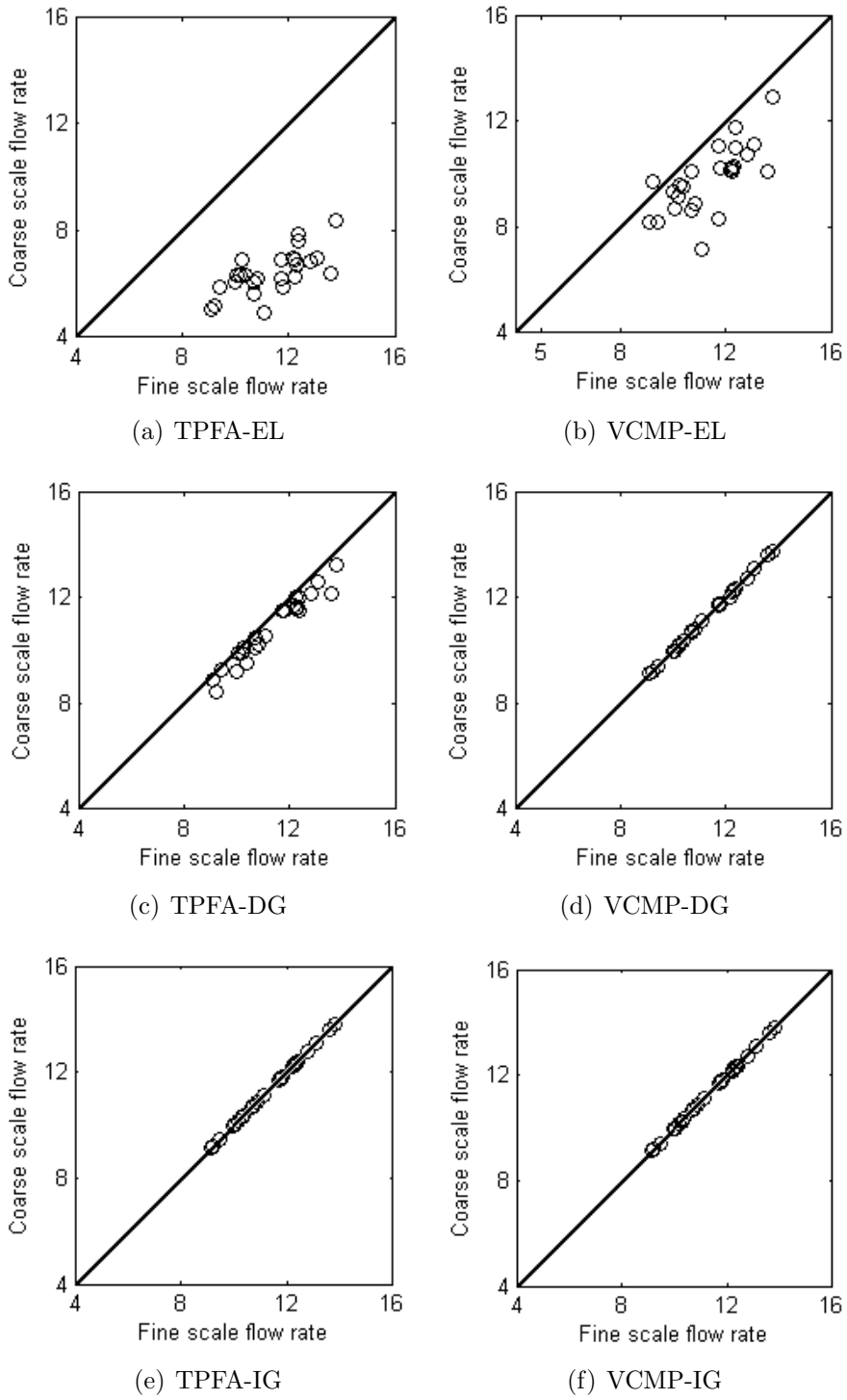

(a) TPFA-EL (b) VCMP-EL

(c) TPFA-DG (d) VCMP-DG

(e) TPFA-IG (f) VCMP-IG

Figure 2.6: Realization-by-realization comparisons for flow rate (along layering flow, Cartesian grids).

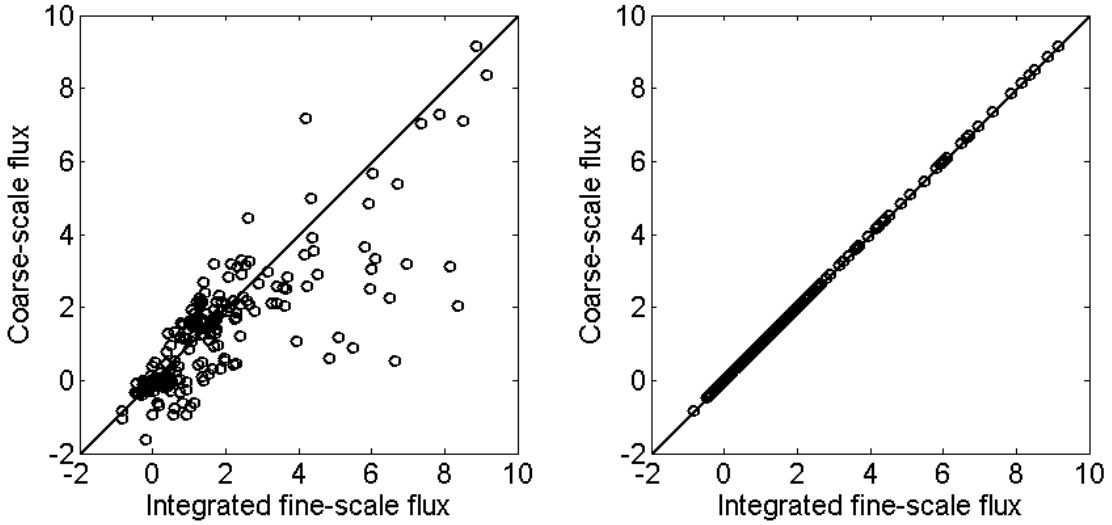

(a) TPFA-DG (b) VCMP-DG

Figure 2.7: Comparison of integrated fine-scale flux and coarse-scale flux for the realization with the largest TPFA-DG flux error (x-direction flow, Cartesian grids).

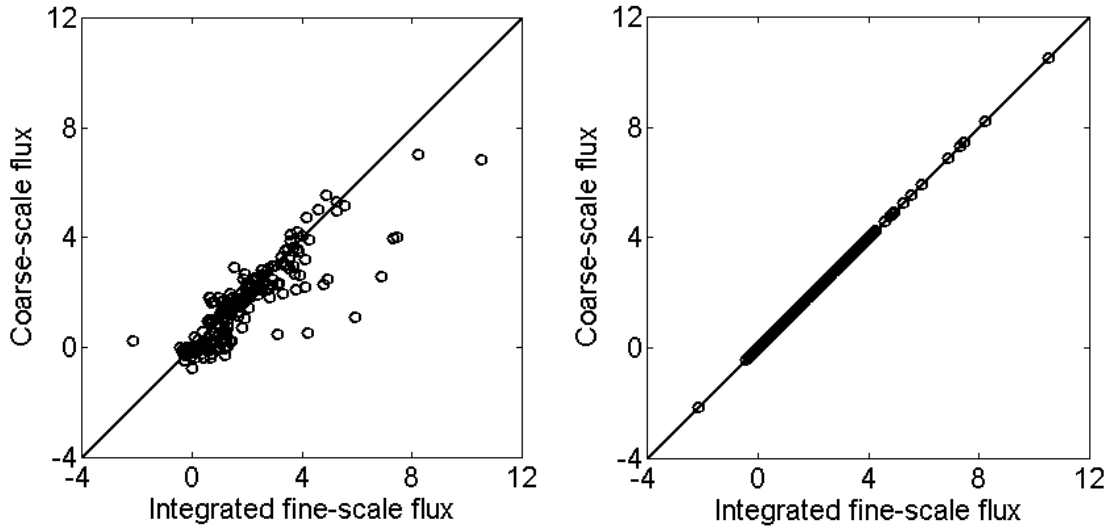

(a) TPFA-DG (b) VCMP-DG

Figure 2.8: Comparison of integrated fine-scale flux and coarse-scale flux for a typical realization (x-direction flow, Cartesian grids).

Figure 2.7, which is the worst-case scenario for flux for TPFA-DG. It is evident that VCMP-DG captures both the magnitude and direction of the averaged fine-scale velocity vectors accurately (Figure 2.9). The velocity vectors resulting from TPFA-DG show less accuracy in both magnitude and direction. The magnitude of velocity is underestimated in many grid cells and orientation is generally aligned too closely with the coordinate axes.

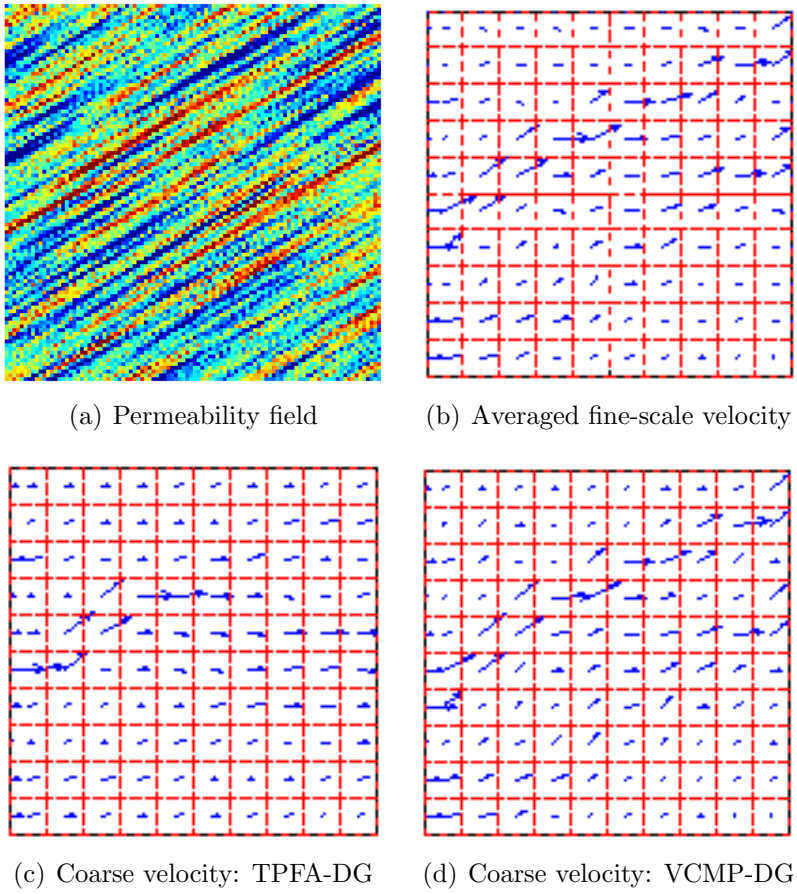

(a) Permeability field (b) Averaged fine-scale velocity

(c) Coarse velocity: TPFA-DG (d) Coarse velocity: VCMP-DG

Figure 2.9: Velocity fields for the realization with the largest TPFA-DG flux error (x-direction flow, Cartesian grids).

We next illustrate the performance of TPFA-IG and VCMP-IG through visualization of the coarse-scale pressure solutions. Again, we consider worst-case (Figure 2.10)

and typical (Figure 2.11) scenarios. The fine-scale results are averaged onto the coarse grid for easier comparison. Significant improvement using VCMP-IG is clearly evident in Figure 2.10, where it is apparent that TPFA-IG is not able to accurately capture the effects of anisotropy. Improvement can also be observed in Figure 2.11, where TPFA-IG again appears limited in representing oriented pressure contours. These results, along with those in Figures 2.7, 2.8, and 2.9, demonstrate that the global VCMP methods are indeed well suited for the accurate modeling of coarse systems with strong full-tensor effects.

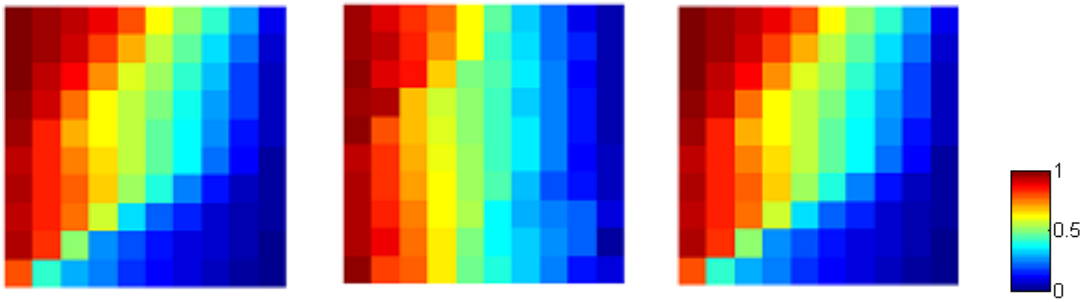

(a) Averaged fine (b) Coarse: TPFA-IG (c) Coarse: VCMP-IG

Figure 2.10: Pressure fields for the realization with the largest pressure error using TPFA-IG (x-direction flow, Cartesian grids).

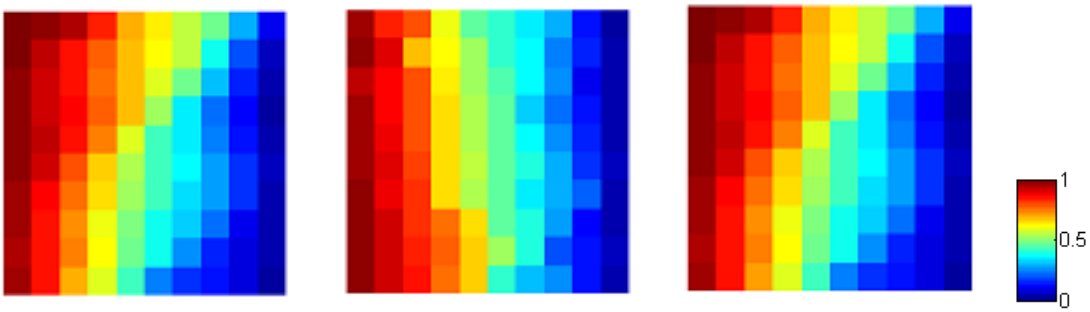

(a) Averaged fine (b) Coarse: TPFA-IG (c) Coarse: VCMP-IG

Figure 2.11: Pressure fields for a typical realization (x-direction flow, Cartesian grids).

TPFA-DG and TPFA-IG were designed for use with global flows identical or very similar to the flow used to generate the upscaled model. In Gerritsen et al. (2006) and Lambers et al. (2008), VCMP-EL was shown to perform robustly also for flows different than the generic flows used in the upscaling procedure. Here we assess the level of robustness of the various methods, which is useful as the methods may be applied within workflows where it is difficult to update the upscaled model as flow rates or well conditions change. We generate the upscaled model using global x-direction flow. Results are presented for VCMP-DG, TPFA-DG, TPFA-IG and VCMP-EL methods (for VCMP-EL, the usual generic local flows are used in the upscaling) for two additional flows.

Results for total flow rate, flux and pressure errors are presented in Tables 2.4, 2.5, and 2.6. The total flow rate errors from global TPFA methods are generally large when applied to flows different than those used to generate coarse-scale models. Except for TPFA-IG for the case of x-direction flow (which was used to generate the TPFA T^*), the TPFA methods generally result in significant flux errors. VCMP-DG provides results that are consistently more accurate than TPFA-IG and TPFA-DG (except for TPFA-IG flux for x-direction flow) and gives results that are generally comparable to VCMP-EL. This suggests that, unlike the TPFA methods, the robustness of VCMP-DG is comparable to that of VCMP-EL, which is one of the best extended local methods. Similar observations hold for the pressure errors, though here the errors using TPFA methods are not as large as they are for flux. The enhanced robustness of VCMP-DG relative to the TPFA methods is likely due in part to the fact that we use a complementary local flow problem in the determination of the upscaled transmissibilities in VCMP, which enables the upscaled model to capture effects that do not appear in the global flow, but also to its flexible multipoint character.

Table 2.4: Robustness test: upscaled transmissibility from flow in the x-direction. Relative errors for total flow rate, E_Q, using various upscaling methods for 25 realizations of log-normal permeability fields with $\theta = 30°$, on 10×10 Cartesian grids.

Corner	VCMP-EL	TPFA-DG	TPFA-IG	VCMP-DG
In x-direction	0.052	0.057	0.001	0.012
Corner flow	0.029	0.191	0.089	0.035
Along layering	0.138	0.231	0.473	0.109

Table 2.5: Robustness test: upscaled transmissibility from flow in the x-direction. L_2 flux errors, E_f, using various upscaling methods for 25 realizations of log-normal permeability fields with $\theta = 30°$, on 10×10 Cartesian grids.

Corner	VCMP-EL	TPFA-DG	TPFA-IG	VCMP-DG
In x-direction	0.072	0.379	0.026	0.033
Corner flow	0.112	0.407	0.279	0.097
Along layering	0.236	0.473	0.817	0.242

Table 2.6: Robustness test: upscaled transmissibility from flow in the x-direction. L_2 pressure errors, E_p, using various upscaling methods for 25 realizations of log-normal permeability fields with $\theta = 30°$, on 10×10 Cartesian grids.

Corner	VCMP-EL	TPFA-DG	TPFA-IG	VCMP-DG
In x-direction	0.014	0.120	0.165	0.009
Corner flow	0.070	0.144	0.153	0.041
Along layering	0.076	0.221	0.349	0.097

2.4.2 Results for Permeability Fields Oriented at 45°

In addition to the base case, we studied permeability fields orientated at 45°. The errors in total flow rate, flux, and pressure are shown in Tables 2.7, 2.8, and 2.9. Compared to the 30° case (Tables 2.1, 2.2, and 2.3), the errors from TPFA-EL generally increase, while the errors from the VCMP methods do not change much. Note that the x-direction flow and the y-direction flow cases are the same statistically because the permeability field is oriented at 45°. The slight differences in results are due to the limited number of realizations (25 in this case).

2.4.3 Results for Non-Square Grid Blocks

We also tested the various upscaling techniques for cases with coarse-grid aspect ratio ($\Delta x/\Delta y$) of 4. This was accomplished by upscaling the 100×100 models to 5×20 models. The total flow rate errors are listed in Table 2.10. The L_2 flux and pressure errors are presented in Tables 2.11 and 2.12. Overall, the errors for this case are slightly higher than those for the base case. It can be seen that large errors from TPFA-EL are reduced significantly by using VCMP-EL. All global methods provide accurate estimates for total flow rate. TPFA-DG gives large flux errors, which are greatly reduced by TPFA-IG, VCMP-DG and VCMP-IG. Pressure errors using TPFA-IG and TPFA-DG are much larger than are those for their counterpart VCMP procedures. Again, we see that the global VCMP methods are the methods of choice.

2.4.4 Results for Irregular Grids

We now demonstrate the performance of the various upscaling techniques on irregular grids. As described above, these grids are generated by randomly perturbing the nodes on uniform grids. Errors for total flow rate, flux, and pressure are presented

Table 2.7: Relative errors for total flow rate, E_Q, using various upscaling methods for 25 realizations of log-normal permeability fields with $\theta = 45°$, on 10×10 Cartesian grids.

Flow	TPFA-EL	VCMP-EL	TPFA-DG	VCMP-DG	TPFA-IG	VCMP-IG
In x-direction	0.132	0.018	0.041	0.0001	0.0004	0.0001
In y-direction	0.135	0.016	0.048	0.00004	0.0003	0.00004
Along layering	0.498	0.142	0.039	0.019	0.00002	0.015
Across layering	0.385	0.078	0.018	0.00003	0.0003	0.00003

Table 2.8: L_2 flux errors, E_f, using various upscaling methods for 25 realizations of log-normal permeability fields with $\theta = 45°$, on 10×10 Cartesian grids.

Flow	TPFA-EL	VCMP-EL	TPFA-DG	VCMP-DG	TPFA-IG	VCMP-IG
In x-direction	0.461	0.091	0.432	0.0005	0.025	0.0005
In y-direction	0.463	0.084	0.427	0.0002	0.021	0.0002
Along layering	0.561	0.231	0.175	0.056	0.005	0.031
Across layering	0.455	0.204	0.191	0.0001	0.029	0.0001

Table 2.9: L_2 pressure errors, E_p, using various upscaling methods for 25 realizations of log-normal permeability fields with $\theta = 45°$, on 10×10 Cartesian grids.

Flow	TPFA-EL	VCMP-EL	TPFA-DG	VCMP-DG	TPFA-IG	VCMP-IG
In x-direction	0.151	0.020	0.140	0.00009	0.198	0.0003
In y-direction	0.148	0.019	0.134	0.00004	0.184	0.0001
Along layering	0.107	0.081	0.048	0.013	0.054	0.040
Across layering	0.078	0.055	0.026	0.00002	0.033	0.0001

Table 2.10: Relative errors for total flow rate, E_Q, using various upscaling methods for 25 realizations of log-normal permeability fields with $\theta = 30°$, on 5×20 Cartesian grids.

Flow	TPFA-EL	VCMP-EL	TPFA-DG	VCMP-DG	TPFA-IG	VCMP-IG
In x-direction	0.267	0.032	0.049	0.004	0.0001	0.002
In y-direction	0.172	0.097	0.029	0.006	0.001	0.001
Along layering	0.444	0.146	0.028	0.004	0.0004	0.003
Across layering	0.269	0.053	0.017	0.012	0.001	0.002

Table 2.11: L_2 flux errors, E_f, using various upscaling methods for 25 realizations of log-normal permeability fields with $\theta = 30°$, on 5×20 Cartesian grids.

Flow	TPFA-EL	VCMP-EL	TPFA-DG	VCMP-DG	TPFA-IG	VCMP-IG
In x-direction	0.680	0.240	0.485	0.015	0.018	0.005
In y-direction	0.357	0.116	0.313	0.021	0.026	0.006
Along layering	0.511	0.279	0.185	0.017	0.011	0.010
Across layering	0.538	0.275	0.164	0.055	0.021	0.010

Table 2.12: L_2 pressure errors, E_p, using various upscaling methods for 25 realizations of log-normal permeability fields with $\theta = 30°$, on 5×20 Cartesian grids.

Flow	TPFA-EL	VCMP-EL	TPFA-DG	VCMP-DG	TPFA-IG	VCMP-IG
In x-direction	0.137	0.053	0.116	0.005	0.158	0.010
In y-direction	0.131	0.020	0.114	0.004	0.149	0.007
Along layering	0.195	0.115	0.053	0.006	0.063	0.018
Across layering	0.086	0.058	0.027	0.008	0.053	0.016

in Tables 2.13, 2.14, 2.15. Note that VCMP-EL has not been applied previously to irregular grids, so these results are also of interest.

The results for the irregular grids are very comparable to those for uniform grids (compare Tables 2.1, 2.2, and 2.3). VCMP-EL consistently provides better accuracy for total flow rate, flux, and pressure than TPFA-EL. For the global methods, TPFA-DG does not provide high accuracy for flux, though errors are quite small using the other three global methods. For pressure, the error using TPFA-IG is significant for x- and y-direction flows. This error is essentially eliminated using the global VCMP methods. Thus, in accordance with the uniform grid results, we see that the global TPFA methods are unable to consistently provide high degrees of accuracy for both flux and pressure for these anisotropic systems. Global VCMP methods, by contrast, are designed to capture full-tensor effects and are therefore able to provide high accuracy for both flux and pressure.

As we did for uniform grids, we now compare the coarse-scale pressure solutions from the TPFA-IG and VCMP-IG methods for random grids. Again, a worst-case scenario (Figure 2.12) and a typical case (Figure 2.13) are shown. For both cases, the coarse-scale solutions from VCMP-IG represent the oriented pressure contours well, while the TPFA-IG results clearly display less accuracy. These results are consistent with the uniform grid results (Figures 2.10 and 2.11).

2.4.5 Accuracy Using M-fix and Selective M-fix

As mentioned in Chapter 1, VCMP, like other standard MPFA methods, can lead to nonmonotonic pressure solutions. Thus the M-fix was designed to guarantee monotonicity. An example to demonstrate the effect of the M-fix is presented in Figure 2.14. It is clear that there are unphysical oscillations in the pressure solution without the M-fix (Figure 2.14(a)). The oscillations are eliminated through application of the M-fix (Figure 2.14(b)).

Table 2.13: Relative errors for total flow rate, E_Q, using various upscaling methods for 25 realizations of log-normal permeability fields with $\theta = 30°$, on 10×10 random grids.

Flow	TPFA-EL	VCMP-EL	TPFA-DG	VCMP-DG	TPFA-IG	VCMP-IG
In x-direction	0.124	0.037	0.029	0.0004	0.0002	0.0004
In y-direction	0.087	0.012	0.018	0.0007	0.0002	0.0002
Along layering	0.443	0.139	0.021	0.003	0.00001	0.002
Across layering	0.208	0.057	0.034	0.0001	0.0003	0.0001

Table 2.14: L_2 flux errors, E_f, using various upscaling methods for 25 realizations of log-normal permeability fields with $\theta = 30°$, on 10×10 random grids.

Flow	TPFA-EL	VCMP-EL	TPFA-DG	VCMP-DG	TPFA-IG	VCMP-IG
In x-direction	0.450	0.059	0.310	0.004	0.015	0.003
In y-direction	0.434	0.109	0.353	0.008	0.017	0.001
Along layering	0.531	0.232	0.156	0.026	0.002	0.010
Across layering	0.372	0.204	0.283	0.0007	0.019	0.0007

Table 2.15: L_2 pressure errors, E_p, using various upscaling methods for 25 realizations of log-normal permeability fields with $\theta = 30°$, on 10×10 random grids.

Flow	TPFA-EL	VCMP-EL	TPFA-DG	VCMP-DG	TPFA-IG	VCMP-IG
In x-direction	0.132	0.013	0.098	0.0007	0.131	0.003
In y-direction	0.120	0.014	0.090	0.0005	0.115	0.001
Along layering	0.116	0.077	0.052	0.009	0.062	0.020
Across layering	0.070	0.044	0.036	0.0001	0.044	0.0006

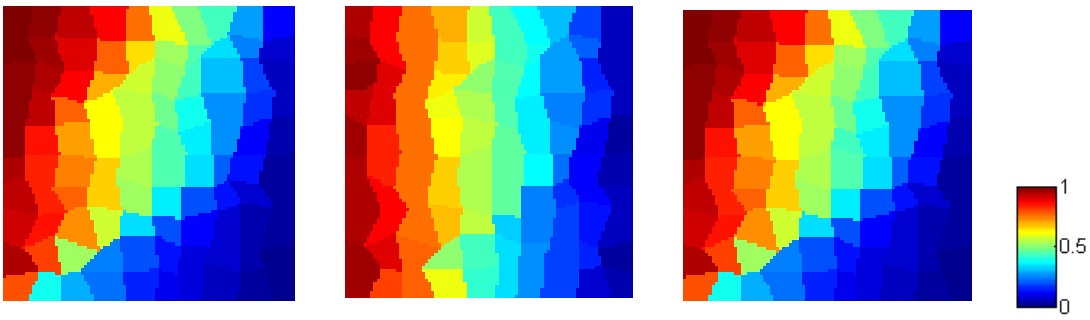

(a) Averaged fine (b) Coarse: TPFA-IG (c) Coarse: VCMP-IG

Figure 2.12: Pressure fields for the realization with the largest pressure error using TPFA-IG (x-direction flow, random grids).

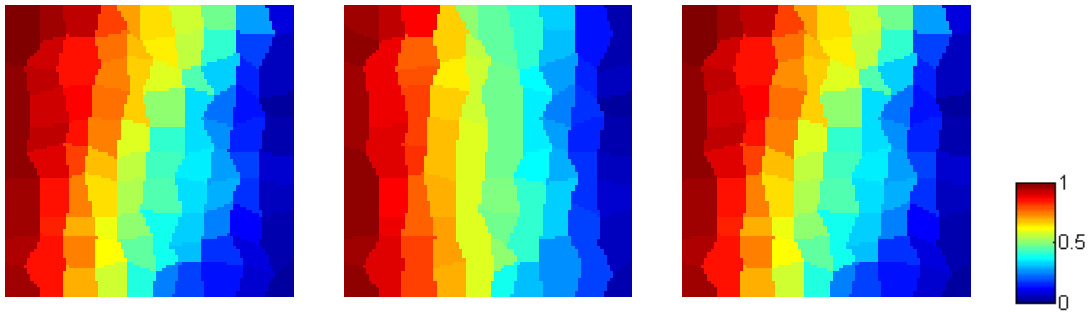

(a) Averaged fine (b) Coarse: TPFA-IG (c) Coarse: VCMP-IG

Figure 2.13: Pressure fields for a typical realization (x-direction flow, random grids).

The full M-fix procedure, however, is a sufficient but not necessary condition to give a monotone pressure solution, as discussed earlier. In the results presented in this paper we use a selective M-fix, that is, we apply the M-fix only when a nonmonotone pressure solution is found. We show here that in some cases the full M-fix can affect solution accuracy. Table 2.16 compares flow results for VCMP-EL and VCMP-DG upscaling with M-fix and selective M-fix techniques for log-normal permeability fields. The total flow rate, L_2 flux, and L_2 pressure errors are averaged over 25 realizations. These results are for flow in the y-direction. It is evident that reductions in all three errors are achieved when the selective M-fix (designated "smfix" in the table) is used

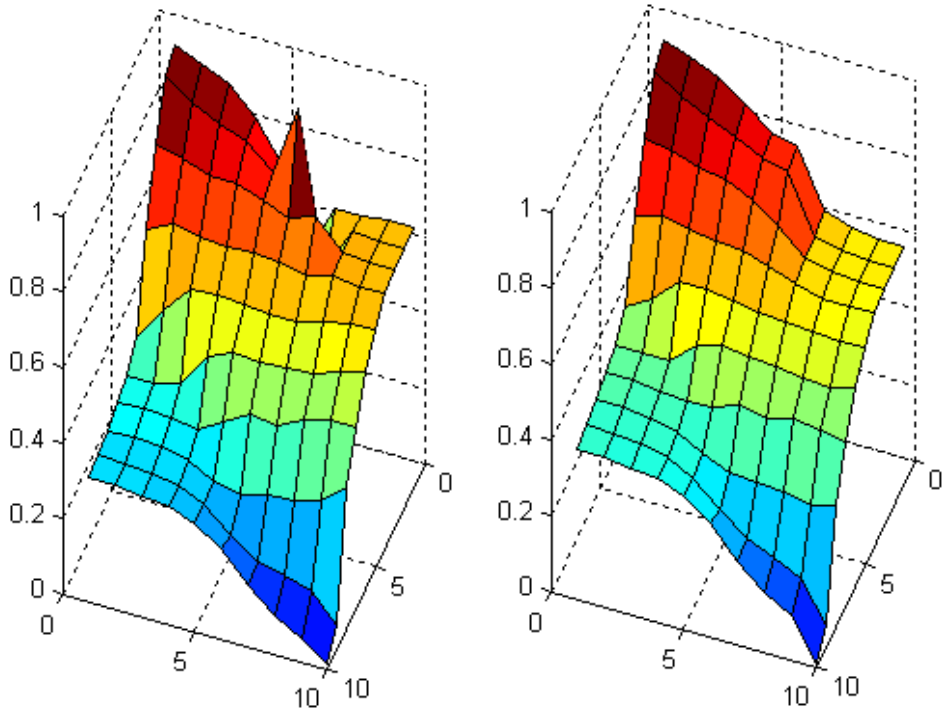

(a) Without M-fix (b) With M-fix

Figure 2.14: Pressure surfaces (a) without M-fix and (b) with M-fix, for a log-normal permeability field with $\theta = 30°$ (along layering flow, Cartesian grids).

in place of the full M-fix (designated "mfix"). This is the case for both the VCMP-EL and VCMP-DG methods, though the improvement is more dramatic for the DG case (for which all three errors are less than 0.1%). We reiterate that although the A matrix generated using the selective M-fix is not an M-matrix, the pressure solution computed by solving $Ap = b$ is nonetheless in all cases monotonic.

The improvement offered through use of the selective M-fix is, however, not always as significant. Table 2.17, for example, shows y-direction flow through 50 channelized layers (considered in the next section) for which case the selective M-fix offers almost no improvement when used with VCMP-EL. Improvement with VCMP-DG, although noticeable, is fairly modest. The limited impact in this case is likely because tensor

effects are not very important for these channelized models, so the results are fairly insensitive to the M-fix treatment.

Table 2.16: Flow results using VCMP-EL or VCMP-DG with full M-fix or selective M-fix, for 25 realizations of log-normal permeability fields, on Cartesian grids, with flow in the y-direction.

Errors	VCMP-EL-mfix	VCMP-EL-smfix	VCMP-DG-mfix	VCMP-DG-smfix
E_Q	0.138	0.016	0.092	0.0002
E_f	0.289	0.106	0.203	0.0009
E_p	0.065	0.013	0.054	0.0001

Table 2.17: Flow results using VCMP-EL or VCMP-DG with full M-fix or selective M-fix, for 50 realizations of SPE 10 permeability fields, on Cartesian grids, with flow in the y-direction.

Errors	VCMP-EL-mfix	VCMP-EL-smfix	VCMP-DG-mfix	VCMP-DG-smfix
E_Q	0.123	0.122	0.020	0.008
E_f	0.348	0.343	0.127	0.068
E_p	0.090	0.089	0.042	0.022

2.5 Results for Channelized Permeability Fields

We now consider the 50 channelized layers from the SPE 10 model. These correspond to the lower 50 layers of the 85 total layers contained in SPE 10. We consider both uniform and irregular grids. In all cases we upscale the 220×60 fine models to 22×6 coarse models.

2.5.1 Results for Cartesian Grids

Table 2.18 presents the mean errors in total flow rate using various upscaling methods for the 50 layers. Tables 2.19 and 2.20 show L_2 flux and pressure errors. Both VCMP-DG and VCMP-IG provide high degrees of accuracy for all quantities. For this case TPFA-IG also provides results of reasonably high accuracy for all quantities including pressure (though pressure error for y-direction flow is 0.086). Pressure errors using TPFA-IG are generally smaller in this case than for the oriented layer case considered above. This is probably because this channelized system does not display strong anisotropy. Indeed, in over 70% of the domain, the maximum of t_3, t_4, t_5, and t_6 (see Eq. (2.6)) is less than 10% of the maximum of t_1 and t_2. Thus, a good TPFA method such as TPFA-IG is able to capture both flux and pressure reasonably well in this case. Results for flux and pressure using VCMP-IG are however in all cases more accurate than those using TPFA-IG. For the extended local methods, VCMP-EL is generally more accurate than TPFA-EL for this system.

We now present the velocity fields computed from TPFA-DG and VCMP-DG in Figure 2.15. We consider x-direction flow in layer 41 of the SPE 10 model. It can be seen that VCMP-DG gives a more accurate representation of the averaged fine-scale velocity vectors than TPFA-DG. The mismatch between the TPFA-DG coarse-scale velocity and the averaged fine-scale velocity is most apparent in the region around $x = 1600$. These results, together with those in Table 2.19, where TPFA-DG is seen to give large L_2 flux errors, demonstrate that direct global upscaling methods combined with VCMP are more suitable than TPFA-DG for channelized systems.

2.5.2 Results for Irregular Grids

The total flow rate, flux, and pressure errors for the various upscaling methods for the 50 channelized layers of SPE 10 on random coarse grids are presented in Tables 2.21,

Table 2.18: Relative errors for total flow rate, E_Q, using various upscaling methods for 50 channelized layers of SPE 10, on 22×6 Cartesian grids.

Flow	TPFA-EL	VCMP-EL	TPFA-DG	VCMP-DG	TPFA-IG	VCMP-IG
In x-direction	0.204	0.025	0.038	0.005	0.001	0.002
In y-direction	0.158	0.122	0.045	0.008	0.004	0.001
Along layering	0.309	0.242	0.016	0.011	0.001	0.001
Across layering	0.313	0.236	0.029	0.012	0.001	0.002

Table 2.19: L_2 flux errors, E_f, using various upscaling methods for 50 channelized layers of SPE 10, on 22×6 Cartesian grids.

Flow	TPFA-EL	VCMP-EL	TPFA-DG	VCMP-DG	TPFA-IG	VCMP-IG
In x-direction	0.368	0.090	0.190	0.021	0.024	0.009
In y-direction	0.417	0.343	0.255	0.068	0.053	0.015
Along layering	0.484	0.369	0.195	0.052	0.033	0.013
Across layering	0.472	0.375	0.196	0.035	0.019	0.009

Table 2.20: L_2 pressure errors, E_p, using various upscaling methods for 50 channelized layers of SPE 10, on 22×6 Cartesian grids.

Flow	TPFA-EL	VCMP-EL	TPFA-DG	VCMP-DG	TPFA-IG	VCMP-IG
In x-direction	0.086	0.028	0.043	0.008	0.046	0.020
In y-direction	0.087	0.089	0.074	0.022	0.086	0.035
Along layering	0.212	0.171	0.037	0.013	0.040	0.020
Across layering	0.200	0.103	0.039	0.010	0.046	0.021

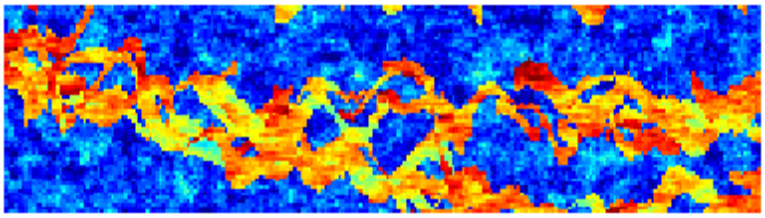

(a) Permeability field

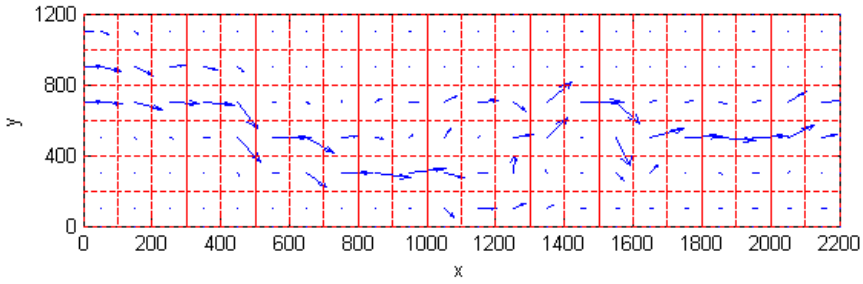

(b) Averaged fine-scale velocity

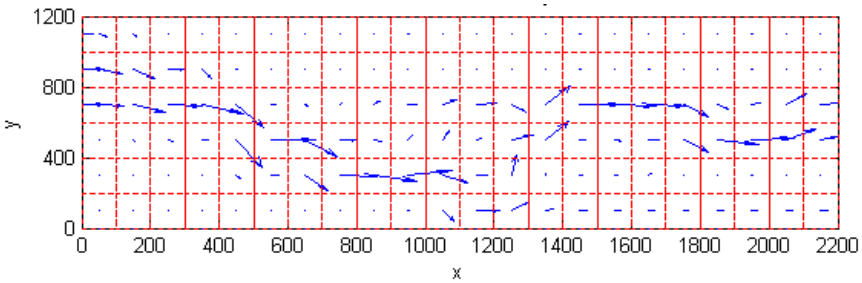

(c) Coarse-scale velocity from TPFA-DG

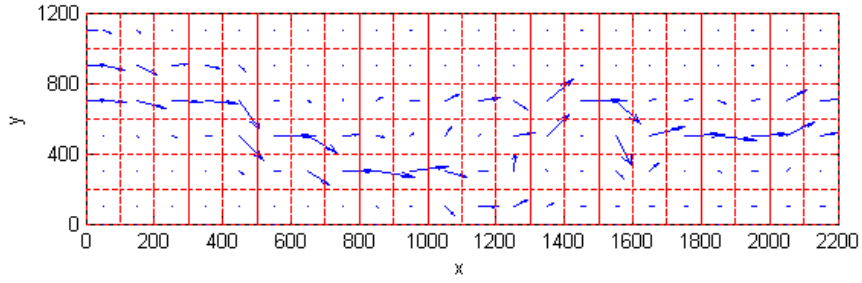

(d) Coarse-scale velocity from VCMP-DG

Figure 2.15: Velocity fields for layer 41 of SPE 10 (x-direction flow, Cartesian grids).

2.22 and 2.23. VCMP-DG reduces the L_2 flux errors from TPFA-DG significantly, as shown in Table 2.22. VCMP-IG and TPFA-IG give results that are accurate and generally quite comparable. It appears that, even with irregular grids, the full-tensor effects for this case are not that significant, which enables TPFA-IG to provide accurate results. This is likely because the average orientation of the grids is still more or less flow aligned. As clearly shown for the non-aligned permeability fields in the previous subsection, the accuracy of TPFA-IG decreases when the full-tensor effects are stronger.

In contrast to the results on uniform grids, VCMP-EL with the selective M-fix provides low accuracy in some cases, particularly for the y-direction flow and across layering flow. The values reported in the tables are strongly impacted by two low-flow layers, which display large errors. Eliminating these two layers, VCMP-EL is seen to provide better accuracy for total flow rate and flux than TPFA-EL (see Table 2.24).

2.6 Discussion

In this chapter we developed and applied new upscaling procedures that are suitable for the accurate representation of general anisotropy (full-tensor effects) in coarse-scale simulation models. These approaches are based on the previously developed variable compact multipoint (VCMP) flux approximation technique. Two important new features were introduced here: the coupling of VCMP with global flow information and the extension of VCMP procedures to irregular quadrilateral grids. A selective M-fix procedure, which enforces the M-matrix property in the upscaled coefficient matrix only when it is necessary to achieve monotone pressure solutions, was also introduced.

We demonstrated the significant improvements offered by global VCMP methods over their TPFA counterparts. Our results demonstrate very clear advantages of

Table 2.21: Relative errors for total flow rate, E_Q, using various upscaling methods for 50 channelized layers of SPE 10, on 22×6 random grids.

Flow	TPFA-EL	VCMP-EL	TPFA-DG	VCMP-DG	TPFA-IG	VCMP-IG
In x-direction	0.229	0.023	0.015	0.009	0.0002	0.006
In y-direction	0.156	0.432	0.050	0.014	0.001	0.002
Along layering	0.336	0.241	0.019	0.033	0.001	0.005
Across layering	0.320	0.578	0.026	0.051	0.001	0.012

Table 2.22: L_2 flux errors, E_f, using various upscaling methods for 50 channelized layers of SPE 10, on 22×6 random grids.

Flow	TPFA-EL	VCMP-EL	TPFA-DG	VCMP-DG	TPFA-IG	VCMP-IG
In x-direction	0.433	0.099	0.183	0.045	0.013	0.019
In y-direction	0.478	0.881	0.342	0.095	0.065	0.023
Along layering	0.551	0.387	0.238	0.100	0.029	0.031
Across layering	0.515	0.768	0.205	0.079	0.018	0.026

Table 2.23: L_2 pressure errors, E_p, using various upscaling methods for 50 channelized layers of SPE 10, on 22×6 random grids.

Flow	TPFA-EL	VCMP-EL	TPFA-DG	VCMP-DG	TPFA-IG	VCMP-IG
In x-direction	0.078	0.027	0.030	0.012	0.036	0.034
In y-direction	0.101	0.109	0.080	0.031	0.095	0.051
Along layering	0.227	0.182	0.040	0.026	0.051	0.045
Across layering	0.207	0.107	0.034	0.023	0.042	0.047

Table 2.24: L_2 flux and pressure errors, using TPFA-EL and VCMP-EL for 48 of the 50 channelized layers of SPE 10, on 22×6 random grids.

	E_Q		E_f		E_p	
Flow	TPFA-EL	VCMP-EL	TPFA-EL	VCMP-EL	TPFA-EL	VCMP-EL
In x-direction	0.233	0.023	0.438	0.099	0.077	0.026
In y-direction	0.162	0.098	0.476	0.295	0.101	0.106
Along layering	0.325	0.225	0.545	0.377	0.231	0.182
Across layering	0.328	0.150	0.517	0.282	0.214	0.102

VCMP-DG over TPFA-DG. In typical cases, the accuracy of VCMP-DG is such that iteration on the resulting transmissibilities is really not necessary; i.e., there is often not much need to perform VCMP-IG. The same cannot be said for TPFA-DG, which often results in significant error, so TPFA-IG is generally required. When VCMP-IG is applied, the iteration procedure is designed to force agreement only in fluxes. As a result, the pressure error generally increases. The flexibility of VCMP makes it possible, however, to devise a modified VCMP-IG procedure in which the objective of the iterations is to minimize error in both pressure and flux. The resulting coarse-scale model could then potentially provide even more accurate pressures than are currently achieved.

Numerical results in this chapter have shown that the inclusion of global flow information in VCMP upscaling computations improves coarse-grid accuracy. However, global upscaling procedures may involve high computational costs that are not affordable in some cases. Therefore, in the next chapter, we develop an alternative technique – the adaptive local-global VCMP method. The VCMP-ALG method is less accurate than the global methods developed in this chapter, but it avoids global fine-scale solutions.

Chapter 3

Adaptive Local-Global VCMP Methods

In the previous chapter, we developed global VCMP upscaling techniques. These methods provide a global upscaling capability that incorporates MPFA representations into coarse-scale models. The methods were demonstrated to provide high degrees of accuracy for log-normally distributed permeability fields with oriented layering and for channelized models. In particular, global VCMP upscaling techniques were consistently more accurate than their TPFA counterparts for cases where full-tensor effects are important.

Global upscaling methods require the solution of a global fine-scale flow problem. The computational costs of this global fine-scale solution can be very high, especially when the resulting flow system is strongly ill-conditioned. Also, we may need to simulate multiple realizations for uncertainty assessments. Multiple global fine-scale simulations result in excessive computational cost. Thus in this chapter, we develop a more efficient procedure – an adaptive local-global VCMP upscaling method. Local-global methods comprise a family of procedures designed to introduce global flow effects without the need for global fine-scale solutions (Chen and Durlofsky, 2006;

Chen et al., 2003; Gerritsen and Lambers, 2008; Wen et al., 2006). Here we combine adaptive local-global methods with VCMP transmissibility calculations to capture full-tensor effects. Compared to global VCMP methods, VCMP-ALG incorporates global flow information without requiring fine-scale global solutions.

This chapter proceeds as follows. The local-global VCMP upscaling technique is first described and key implementation issues are noted. Next, we present single-phase and two-phase simulation results for challenging (oriented) two-dimensional systems that demonstrate the accuracy and capabilities of the method. We also consider the effect of border region sizes and the robustness of the VCMP-ALG method.

3.1 Algorithm for VCMP-ALG

The idea with local-global procedures is to incorporate approximate global flow information into the upscaling computations. In the so-called adaptive local-global (ALG) method, which is the procedure used here, the global flow information is generated by simulating the actual flow problem of interest. Coupled local-global methods (Chen et al., 2003), which use information from generic global flow problems, could also be combined with VCMP schemes, though this is not investigated here.

As indicated above, adaptive local-global methods (Chen and Durlofsky, 2006) add information from specific global coarse-scale solutions into the local property calculations. To determine these coarse-scale solutions, an estimate of t_i (for VCMP-ALG) or T^* (for the ALG method based on two-point flux approximations, referred to as TPFA-ALG) is first required. These initial estimates are computed through application of standard local or extended-local methods using generic boundary conditions. The global coarse-scale solutions are used to determine the boundary conditions applied in the upscaling. Because the global solutions are on the coarse scale, an interpolation procedure must be introduced to provide boundary conditions for the

local fine-scale solutions of Eq. (2.1). The flow problem thus defined (i.e., by interpolating the global coarse-scale pressure solution to provide local fine-scale boundary conditions) provides one of the flow problems required by VCMP. For the second flow problem, in analogy with the approach used for global VCMP methods in Chapter 2, we define a complementary set of boundary conditions which prescribe a pressure gradient which is approximately orthogonal to that of the first flow (the specific boundary conditions are given below). This complementary flow problem is not required for TPFA-ALG. The upscaled transmissibilities are then recomputed. The procedure is iterated until a self-consistent solution is obtained.

The specific algorithm is as follows:

1. Solve a global coarse-scale problem with transmissibility t determined from a VCMP extended local upscaling procedure. Set the iteration number $\nu = 0$.

2. For each face of the coarse-scale grid, define an extended local region, for which fine-scale pressure boundary conditions are determined through interpolation of global coarse-scale pressures. Solve this local fine-scale problem and obtain pressure and flux solutions designated p_1^ν and f_1^ν. Find coarse-scale pressures p_1^c by averaging fine-scale pressures and calculate coarse-scale fluxes f_1^c by integrating fine-scale fluxes.

3. Calculate the averaged pressure gradients, $[\partial p_1^\nu/\partial x, \partial p_1^\nu/\partial y]$, across the extended region. Define a complementary local fine-scale flow with pressure gradient orthogonal to that of p_1^ν, i.e., $[\partial p_2^\nu/\partial x, \partial p_2^\nu/\partial y] = [-\partial p_1^\nu/\partial y, \partial p_1^\nu/\partial x]$. Solve the complementary flow and obtain p_2^ν and f_2^ν. Determine coarse pressures p_2^c and fluxes f_2^c.

4. Compute the VCMP transmissibilities $t^{\text{est},\nu}$ by solving an optimization problem (Eq. (2.7)) honoring the two flows (p_1^c and f_1^c, p_2^c and f_2^c) and also subject to

the constraints in Eq. (2.8). In the rare case when the optimization problem cannot be solved, keep the value from the last iteration, i.e., $t^{\text{est},\nu} = t^{\nu}$.

5. Apply a relaxation procedure to determine t for the next iteration:

$$t^{\nu+1} = \alpha t^{\text{est},\nu} + (1-\alpha)t^{\nu}, \tag{3.1}$$

where $0 \leq \alpha \leq 1$ is a relaxation parameter. In this work, we use $\alpha = 0.5$.

6. Solve the global coarse-scale problem using $t^{\nu+1}$. Check if the pressure solution is monotone. If not, return to step 4, recompute coarse-scale transmissibilities using the M-fix as required (Chen et al., 2009), and again solve the coarse-scale pressure equation. Update coarse pressures $(p^c)^{\nu+1}$ and coarse fluxes $(f^c)^{\nu+1}$.

7. Set $\nu = \nu + 1$ and iterate through steps 2–6 until a 'converged' solution is achieved.

The convergence criteria are based on the change in the VCMP-ALG solution between iterations. We terminate the iteration if

$$\max\left(\frac{\parallel (p^c)^{\nu} - (p^c)^{\nu-1} \parallel_2}{\parallel (p^c)^{\nu} \parallel_2}, \frac{\mid (Q^c)^{\nu} - (Q^c)^{\nu-1} \mid}{\mid (Q^c)^{\nu} \mid}\right) \leq tol, \tag{3.2}$$

where Q^c is the total flow rate at the boundary from the coarse-scale model and p^c is coarse-scale pressure. The parameter tol is the tolerance (here we set $tol = 0.01$). Significant error reduction is achieved in the first few iterations.

A thresholding procedure is applied to reduce computational costs by updating t_i only in high-flow regions (Chen and Durlofsky, 2006). Thresholding can also help avoid anomalous coarse-scale properties in regions with low flow rates. For the thresholding parameter defined in Chen and Durlofsky (2006), we use $\varepsilon = 0.1$, which is suggested by Chen and Durlofsky (2006) based on their sensitivity analysis. For the

weighting parameter α, introduced in Eq. (2.8), we use $\alpha_1 = 5 \times |f_2^c/f_1^c|, \alpha_2 = 1$ in the local-global VCMP method such that the global flow is honored more than the complementary local flow during the optimization procedure.

3.2 Implementation Issues for VCMP-ALG

Here we discuss the determination of local fine-scale boundary conditions from the coarse-scale pressure solution and the use of reduced border regions in the upscaling computations.

We apply a triangle-based linear interpolation of the coarse-scale pressure to provide boundary conditions for the upscaling computations. The approach, illustrated in Figure 3.1, is applicable for both Cartesian and irregular quadrilateral grids. In the figure, the coarse-scale pressures from the most recent global solution are shown as black $\times$'s. Pressure values are required along the boundary of the extended local region (shown in green). For pressure at a particular location (x_0, y_0), designated by the red circle on the boundary of the extended local region, we find the three nearest coarse-scale pressure values and apply linear interpolation. Other more complicated pressure interpolation algorithms (such as harmonic interpolation) were tested but no consistent improvement in coarse-scale accuracy was observed.

The size of the border region in extended local and local-global algorithms generally impacts the accuracy of the coarse solution, with larger border regions providing better accuracy. Larger border regions, however, require more computation, so it is important to determine the appropriate size. In Wen et al. (2006) it was shown that relatively small border regions provided accurate results for three-dimensional simulations using TPFA-ALG. Figure 3.2 illustrates the local region and different sized border regions (here we describe the regions in terms of VCMP upscaling methods, while Figure 1.2 is drawn for TPFA methods). The target interface (shown in bold

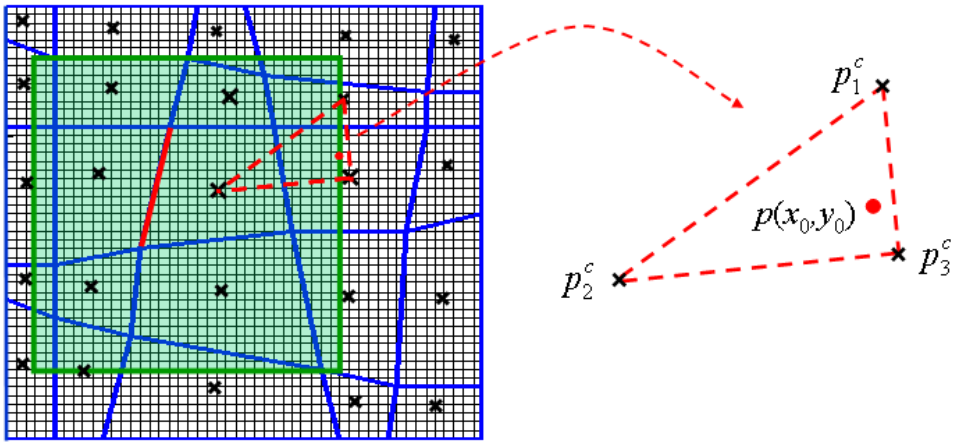

Figure 3.1: Pressure interpolation to determine boundary conditions for VCMP-ALG upscaling computations. VCMP extended local region is depicted in shaded green. The coarse grid is depicted in heavier lines and the fine grid in lighter lines.

red) is in the center of the region. The light green area corresponds to the local VCMP region, which includes all fine cells needed to form rectangular coarse blocks that cover the six irregular coarse blocks. The 'default' extended local region is often taken to include the fine cells corresponding to an additional column of coarse cells on each side of the local region. This region is outlined in Figure 3.2 by the blue dashed line. An alternate (reduced) extended local region is indicated by the solid red line in Figure 3.2. For this reduced region, we extend the local region by just two fine cells in the direction perpendicular (or approximately perpendicular) to the target face.

3.3 Numerical Results

We now test the performance of the new VCMP-ALG methods on a range of examples on both Cartesian and irregular structured grids. These results are compared to those obtained using an extended local VCMP (VCMP-EL) method and an adaptive local-global technique that uses two-point flux approximation (TPFA-ALG). These techniques are the appropriate methods for comparison because the new VCMP-ALG

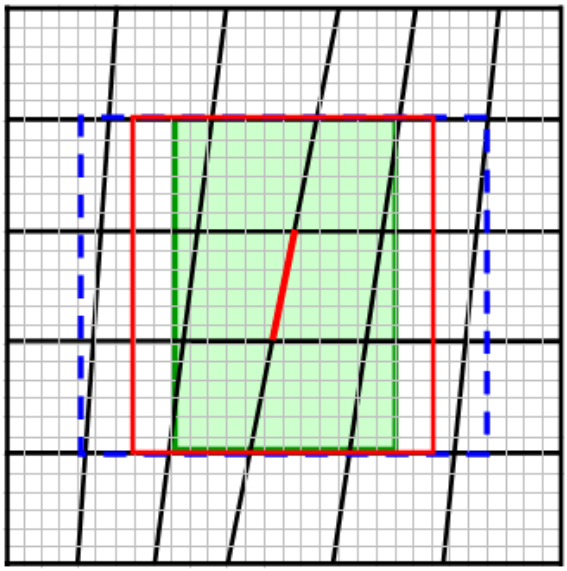

Figure 3.2: VCMP local region (shaded green), large border region (blue dashed lines), and reduced border region (red solid lines) for a general quadrilateral coarse grid. The coarse grid is depicted in heavier lines and the fine grid in lighter lines.

approach essentially combines these two procedures. We also compare to VCMP-DG, which is expected to be the worst accurate method. We note that all of these upscaling methods are typically much more accurate than an extended local TPFA method (as is evident from the results in Chapter 2). Our test suite consists of two types of fine-scale permeability fields: 25 realizations of a variogram-based geostatistical model and 20 layers taken from the Stanford VI model (Castro, 2007), which represent a deltaic system.

3.3.1 Results for Log-normal Permeability Fields with Cartesian Grids

We use the same log-normal permeability fields, with $\theta = 30°$, and apply the same boundary conditions as described in Chapter 2. The results using VCMP-ALG, VCMP-EL, and TPFA-ALG are presented for coarse Cartesian grids in this section.

Results for irregular quadrilateral grids are presented in Section 3.3.2. We additionally investigate the effect of the border region size on accuracy and the process dependency of the various upscaling methods for selected flows.

We first evaluate the effect of the border region size on the accuracy of VCMP-ALG upscaling. The parameter r_f refers to the number of fine-scale columns included on the inlet and outlet sides of the local region (i.e., in the flow direction). With reference to Figure 3.2, the red box corresponds to r_f=2 and the dashed blue box to r_f=5. The local region (shaded green) is designated by r_f=0. The total flow rate errors using VCMP-ALG with r_f=10, 2 and 0 are presented in Table 3.1. The L_2 flux and pressure errors are listed in Tables 3.2 and 3.3. It is evident that, as would be expected, the upscaling accuracy generally degrades as the size of the border region decreases. The results nonetheless show that the reduced method does provide reasonable accuracy along with efficiency. This is consistent with the results reported by Wen et al. (2006). Using r_f=2, the error in flow rate is in all cases less than 10%, and this is the value we will use in subsequent computations. Note that we also use r_f=2 for all VCMP-EL and TPFA-ALG computations. It should be kept in mind that higher accuracy could be achieved by using larger r_f, but at the expense of computational efficiency. It is worth pointing out that all the results in Chapter 2 use r_f=10.

We now demonstrate the improvement achieved with iteration using VCMP-ALG. The system in the first case is the realization that gives the largest error in flow rate (of the 25 layers considered) using VCMP-EL for flow along the layering. Results for flow rate error, flux error and pressure error as a function of iteration number are shown in Figure 3.3. For total flow rate, the initial error of 33% (obtained using VCMP-EL) is reduced to 1.9% by VCMP-ALG. Large error reduction in flux and pressure is also observed. It is evident that this reduction is achieved in just two iterations. The second case is for the realization with total flow rate error nearest the average value (Figure 3.4). The error reduction in total flow rate, flux and pressure is mainly

Table 3.1: Total flow rate errors, E_Q, using VCMP-ALG methods with different sized border regions for 25 realizations of log-normal permeability fields on 10×10 Cartesian grids.

Flow	$r_f = 10$	$r_f = 2$	$r_f = 0$
In x-direction	0.011	0.036	0.050
In y-direction	0.013	0.045	0.082
Across layering	0.015	0.018	0.035
Along layering	0.042	0.083	0.113

Table 3.2: L_2 flux errors, E_f, using VCMP-ALG methods with different sized border regions for 25 realizations of log-normal permeability fields on 10×10 Cartesian grids.

Flow	$r_f = 10$	$r_f = 2$	$r_f = 0$
In x-direction	0.032	0.054	0.071
In y-direction	0.065	0.094	0.133
Across layering	0.071	0.057	0.097
Along layering	0.091	0.124	0.149

Table 3.3: L_2 pressure errors, E_p, using VCMP-ALG methods with different sized border regions for 25 realizations of log-normal permeability fields on 10×10 Cartesian grids.

Flow	$r_f = 10$	$r_f = 2$	$r_f = 0$
In x-direction	0.007	0.010	0.013
In y-direction	0.008	0.013	0.020
Across layering	0.021	0.018	0.026
Along layering	0.012	0.017	0.022

achieved in only one iteration. Therefore the additional cost of using VCMP-ALG is not excessive.

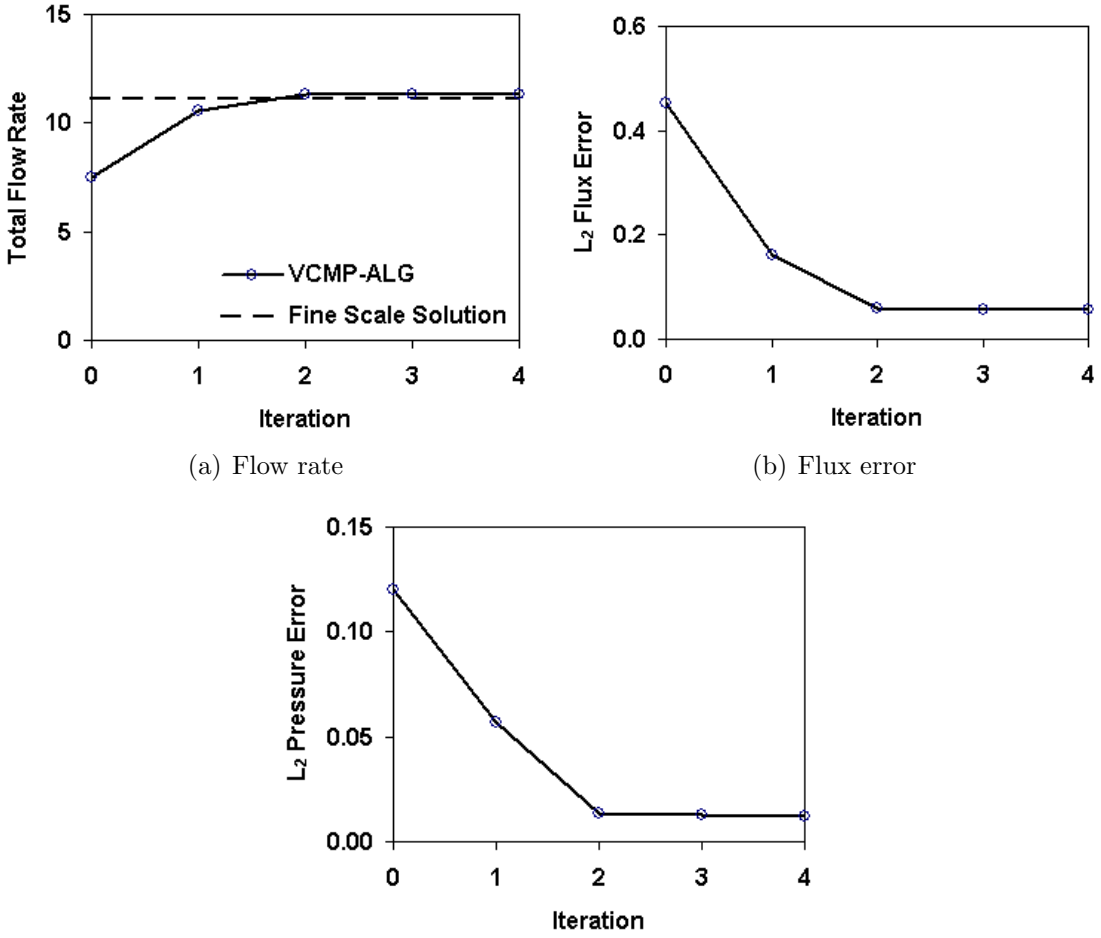

(a) Flow rate

(b) Flux error

(c) Pressure error

Figure 3.3: VCMP-ALG results for along layering flow for a log-normal permeability field for which VCMP-EL gives the largest total flow rate error.

Tables 3.4, 3.5, and 3.6 present the errors for total flow rate, flux, and pressure. These results represent averages over the 25 realizations. The errors from VCMP-ALG are generally smaller than those from VCMP-EL (an exception is flow rate error for across layering flow), and larger than those from VCMP-DG. Note that the VCMP-DG results presented in this chapter differ slightly from those in Chapter 2,

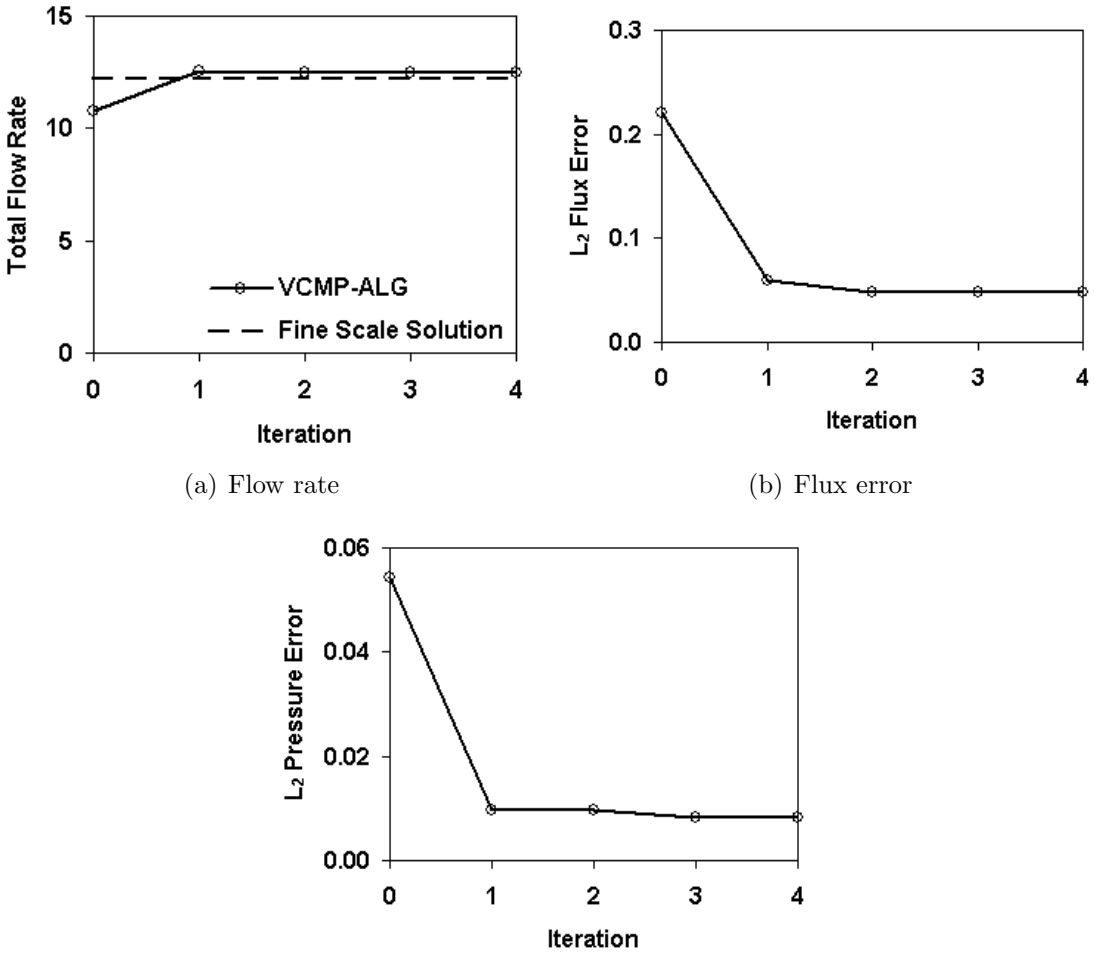

(a) Flow rate

(b) Flux error

(c) Pressure error

Figure 3.4: VCMP-ALG results for along layering flow for a log-normal permeability field for which VCMP-EL gives a total flow rate error nearest the average value.

because here we use $r_f = 2$ while in Chapter 2 we used $r_f = 10$. Compared to TPFA-ALG, VCMP-ALG provides improved accuracy in all errors. Specifically, for the L_2 flux error, error reduction of a factor of 2–6 is observed, while for L_2 pressure error, error reduction ranges from a factor of about 3–10.

The results presented in the tables can also be viewed on a realization-by-realization basis. In Figure 3.5 we present crossplots of coarse-scale flow rates versus fine-scale

Table 3.4: Relative errors for total flow rate, E_Q, using various upscaling methods for 25 realizations of log-normal permeability fields on 10×10 Cartesian grids.

Flow	VCMP-EL	TPFA-ALG	VCMP-ALG	VCMP-DG
In x-direction	0.068	0.075	0.036	0.00004
In y-direction	0.045	0.145	0.045	0.0006
Along layering	0.120	0.020	0.018	0.002
Across layering	0.055	0.163	0.083	0.0001

Table 3.5: L_2 flux errors, E_f, using various upscaling methods for 25 realizations of log-normal permeability fields on 10×10 Cartesian grids.

Flow	VCMP-EL	TPFA-ALG	VCMP-ALG	VCMP-DG
In x-direction	0.085	0.313	0.054	0.0003
In y-direction	0.131	0.372	0.094	0.005
Along layering	0.223	0.165	0.057	0.014
Across layering	0.193	0.274	0.124	0.0004

Table 3.6: L_2 pressure errors, E_p, using various upscaling methods for 25 realizations of log-normal permeability fields on 10×10 Cartesian grids.

Flow	VCMP-EL	TPFA-ALG	VCMP-ALG	VCMP-DG
In x-direction	0.014	0.097	0.010	0.00004
In y-direction	0.019	0.096	0.013	0.0004
Along layering	0.074	0.063	0.018	0.005
Across layering	0.039	0.047	0.017	0.0001

flow rates using all three upscaling methods for the 25 variogram-based realizations. These plots are for y-direction flow. For this boundary condition, the TPFA-ALG method gives the lowest accuracy ($E_Q = 0.145$ as shown in Table 3.4), while the VCMP-EL and VCMP-ALG methods provide better accuracy ($E_Q = 0.045$ for both methods). These results illustrate that use of TPFA-ALG leads to a degradation in accuracy for systems with strong full-tensor anisotropy. This is perhaps not surprising, as the method attempts to capture full-tensor effects with a two-point flux approximation.

Next we consider along layering flow (Figure 3.6). Here we see that TPFA-ALG and VCMP-ALG provide the most accurate results, while use of VCMP-EL leads to some error. For this flow scenario, it appears to be important to capture the effects of large-scale permeability connectivity in the coarse model – otherwise the total flow rate may be underestimated. For this reason the ALG methods perform well, while the extended local method results in the underprediction of flow rate. It would appear that, for this flow scenario, the inclusion of large-scale flow information is the essential ingredient and that capturing full-tensor effects is secondary, which is why TPFA-ALG and VCMP-ALG perform comparably.

We next consider detailed face-by-face comparisons of flux for two particular models. These are presented in Figures 3.7 and 3.8 where we plot coarse-scale versus integrated fine-scale fluxes at each coarse face for along layering flow. We compare results using VCMP-EL (Figures 3.7(a) and 3.8(a)) and VCMP-ALG (Figures 3.7(b) and 3.8(b)). Figure 3.7 is for realization with the largest L_2 flux error using VCMP-EL and Figure 3.8 is for the realization with L_2 flux error nearest the average value reported in Table 3.5. For both cases, the face-by-face flux results are clearly improved by using VCMP-ALG rather than VCMP-EL.

Similar face-by-face flux comparisons using TPFA-ALG and VCMP-ALG are presented in Figures 3.9 and 3.10. We again consider both the case with the largest L_2

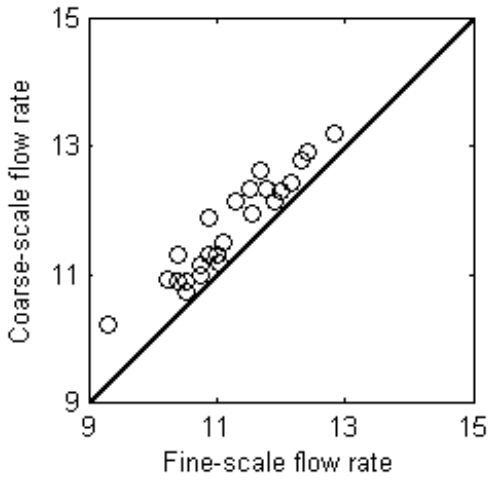

(a) VCMP-EL

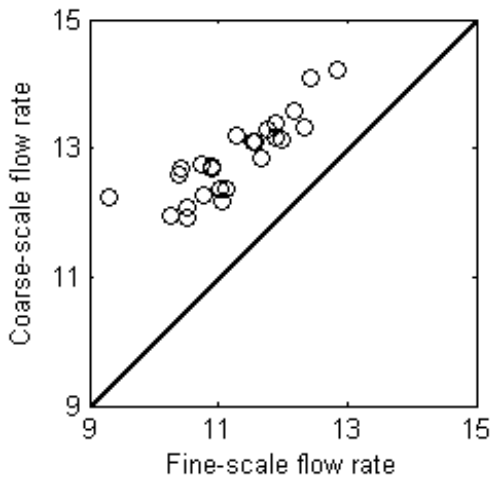

(b) TPFA-ALG

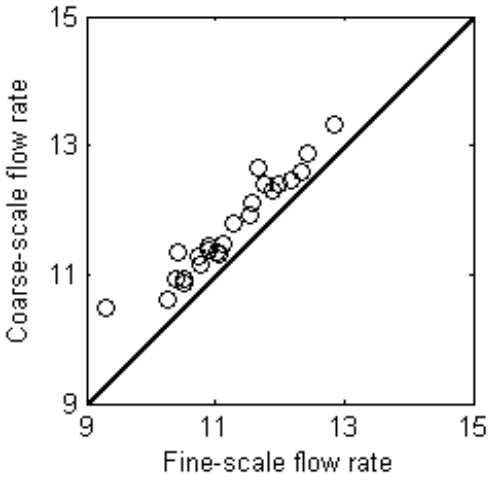

(c) VCMP-ALG

Figure 3.5: Realization-by-realization comparisons for flow rate (y-direction flow, Cartesian grids).

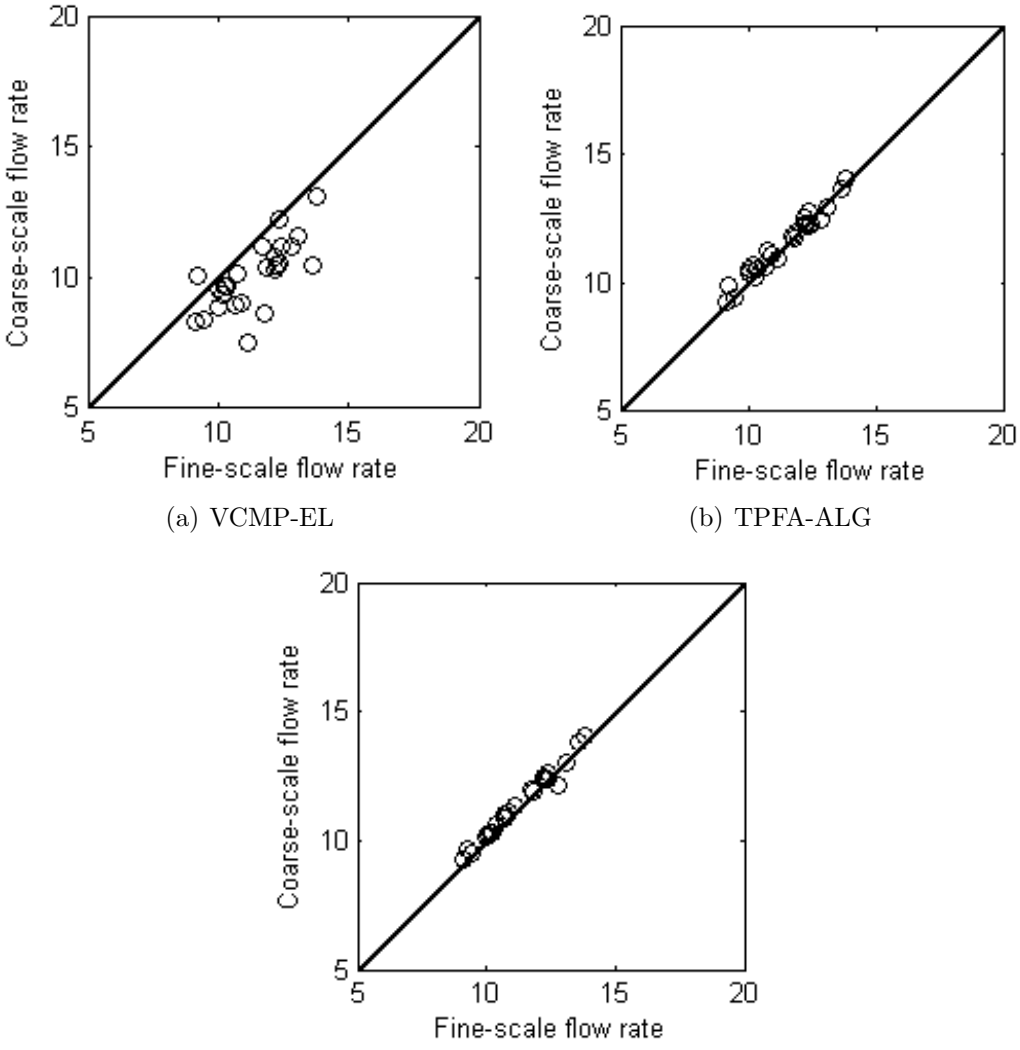

(a) VCMP-EL

(b) TPFA-ALG

(c) VCMP-ALG

Figure 3.6: Realization-by-realization comparisons for flow rate (along layering flow, Cartesian grids).

flux error using TPFA-ALG and the case with error closest to the average. These results are for the case of y-direction flow. Again, we see that VCMP-ALG clearly provides the more accurate results for face-by-face flux.

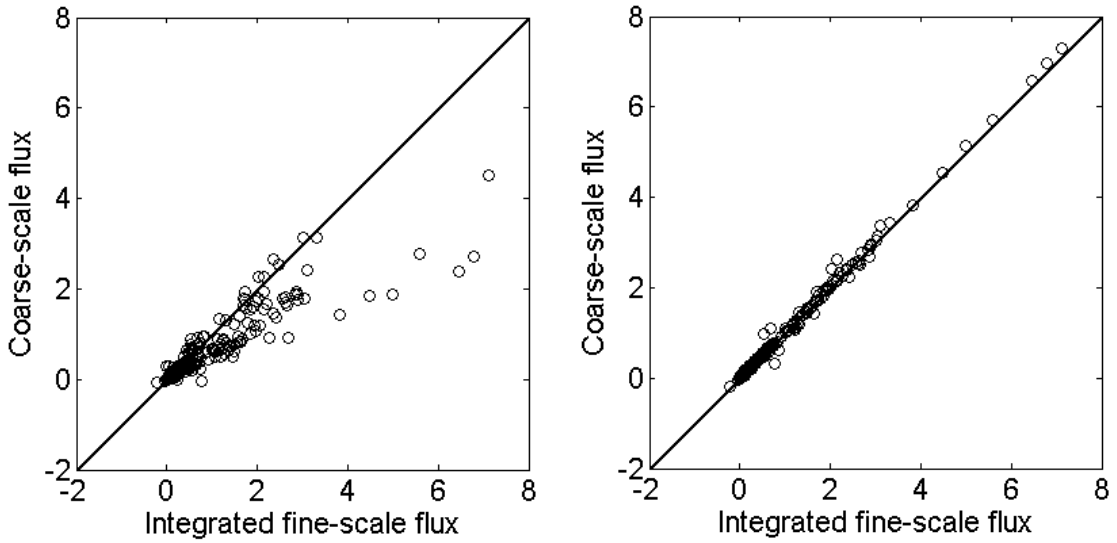

(a) VCMP-EL (b) VCMP-ALG

Figure 3.7: Comparison of integrated fine-scale flux and coarse-scale flux for the realization with the largest VCMP-EL flux error (along layering flow, Cartesian grids).

We next compare pressure fields from VCMP-EL and VCMP-ALG to fine-scale results for particular realizations. For easier comparison, we first average the fine-scale results onto the coarse 10×10 grid. Again we consider the case with the maximum error (using VCMP-EL) and a typical case for along layering flow. Results are presented in Figures 3.11 and 3.12. Coarse pressures using VCMP-ALG are clearly more accurate than those using VCMP-EL. This is immediately evident in Figure 3.11, but careful inspection of Figure 3.12 also leads to the same conclusion.

Taken in total, the results presented above demonstrate the advantages of VCMP-ALG over both VCMP-EL and TPFA-ALG. More specifically, Figures 3.3, 3.6, 3.7, 3.8, 3.11, and 3.12 show that VCMP-ALG provides a higher level of accuracy than VCMP-EL. In addition, Figures 3.5, 3.9, and 3.10 demonstrate that VCMP-ALG

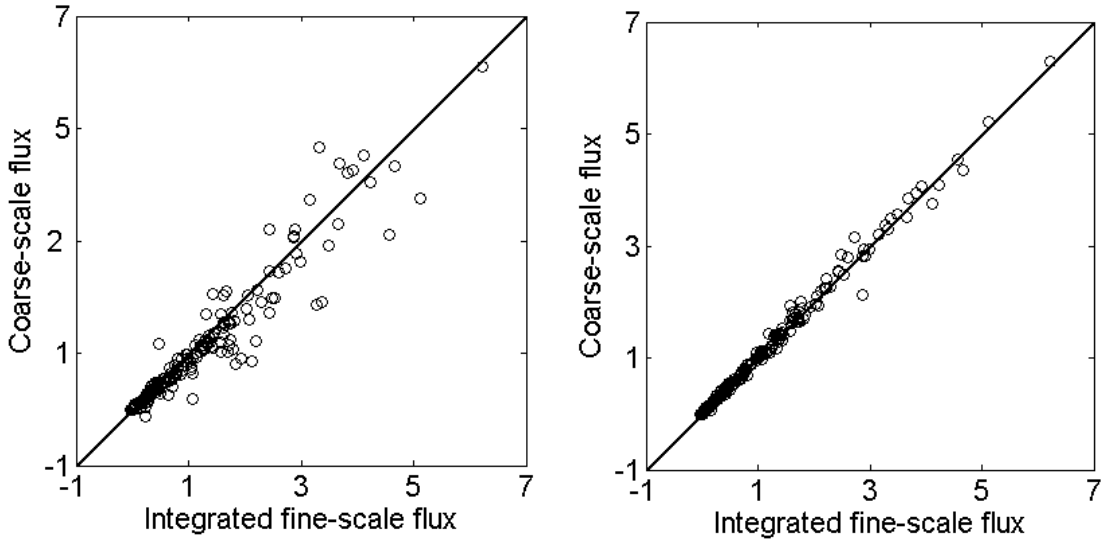

(a) VCMP-EL (b) VCMP-ALG

Figure 3.8: Comparison of integrated fine-scale flux and coarse-scale flux for a typical realization (along layering flow, Cartesian grids).

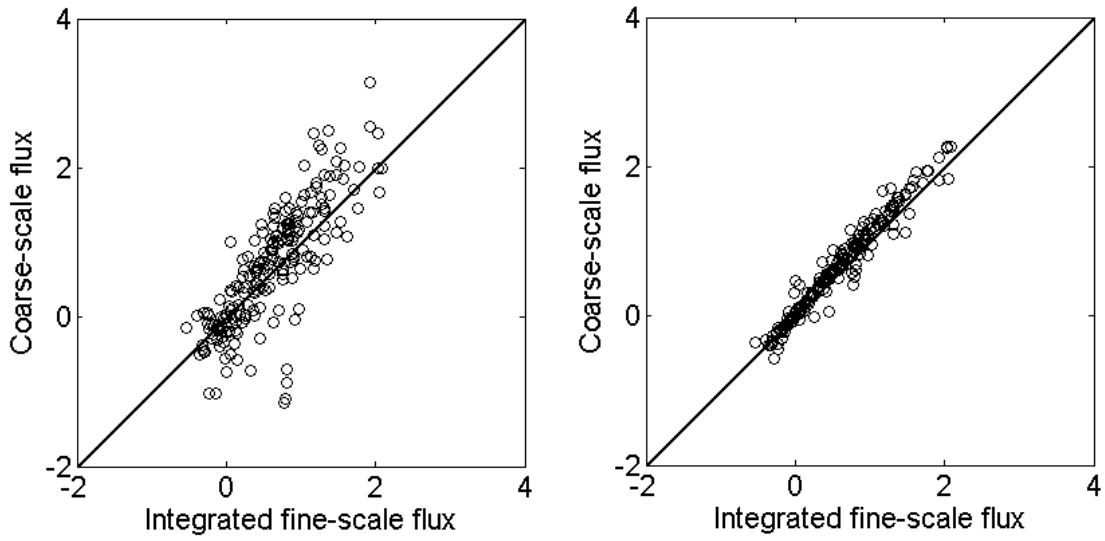

(a) TPFA-ALG (b) VCMP-ALG

Figure 3.9: Comparison of integrated fine-scale flux and coarse-scale flux for a realization with the largest TPFA-ALG flux error (y-direction flow, Cartesian grids).

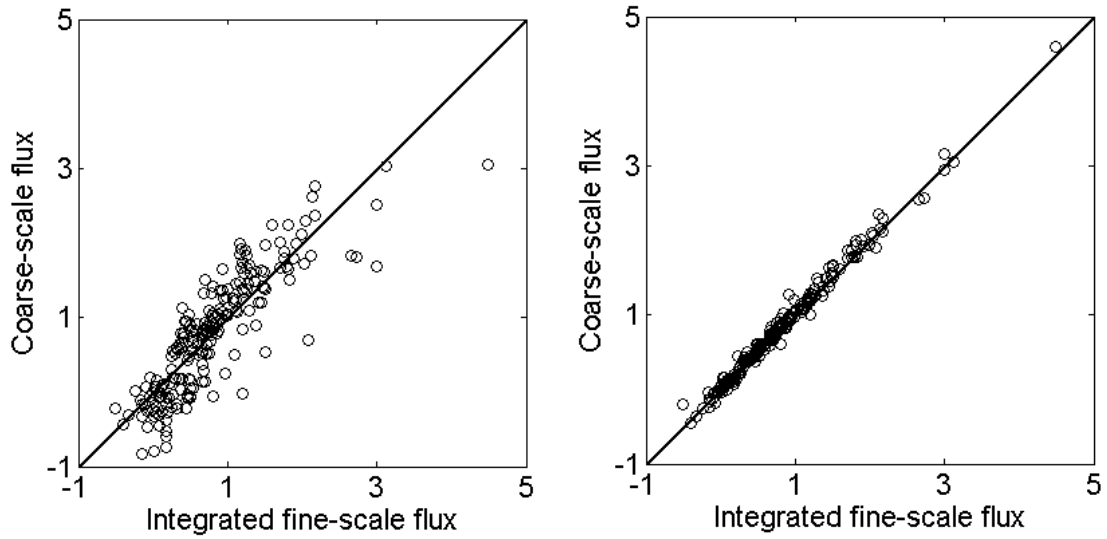

(a) TPFA-ALG (b) VCMP-ALG

Figure 3.10: Comparison of integrated fine-scale flux and coarse-scale flux for a typical realization (y-direction flow, Cartesian grids).

methods are preferable to TPFA-ALG for modeling coarse systems with strong full-tensor effects. Thus, from these results we can conclude that VCMP-ALG successfully incorporates both approximate global and full-tensor effects in the coarse model.

We next assess the robustness (also referred to as the process dependency) of VCMP-ALG, VCMP-EL, and TPFA-ALG (the robustness of VCMP-DG was considered in Chapter 2. By this we mean the accuracy of the methods for flow scenarios that differ from those used for the construction of the coarse-scale model. For VCMP-ALG and TPFA-ALG, we first generate upscaled models using global x-direction flow (recall that a complementary flow problem is also used for VCMP-ALG). For VCMP-EL, we construct the coarse model as usual using two generic local flows.

The total flow rate, L_2 flux and pressure errors are shown in Tables 3.7, 3.8, and 3.9. For total flow rate, VCMP-ALG provides results for corner flow and along layering flow that are comparable to VCMP-EL and significantly more accurate than TPFA-ALG. This indicates a reasonable degree of robustness in the VCMP-ALG

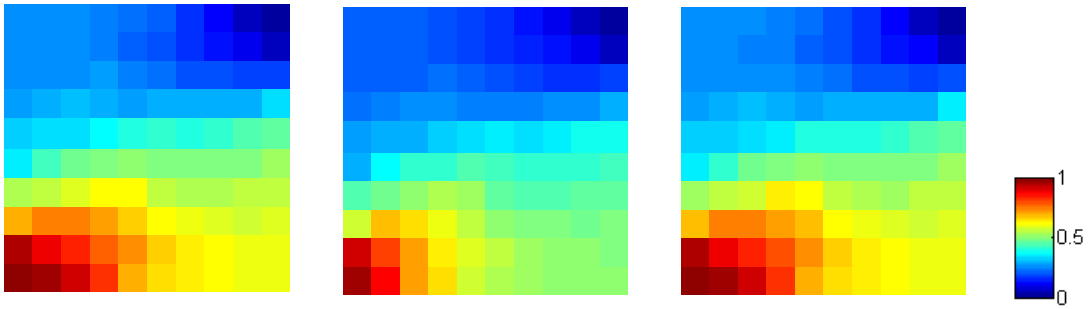

(a) Averaged fine (b) Coarse: VCMP-EL (c) Coarse: VCMP-ALG

Figure 3.11: Pressure fields for the realization with the largest pressure error using VCMP-EL (along layering flow, Cartesian grids).

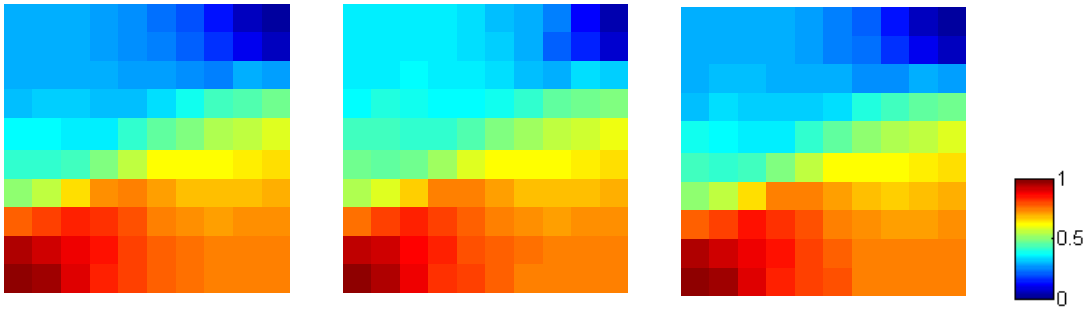

(a) Averaged fine (b) Coarse: VCMP-EL (c) Coarse: VCMP-ALG

Figure 3.12: Pressure fields for a typical realization (along layering flow, Cartesian grids).

model. It should be noted that enhanced robustness could likely be achieved with TPFA-ALG if a complementary flow problem was incorporated into the formulation. For flux and pressure errors, VCMP-ALG is again seen to outperform TPFA-ALG and to give results comparable to those using VCMP-EL. Note that the errors associated with VCMP-ALG for the x-direction flow are slightly different from those reported in Tables 3.4 and 3.6 because of the way we apply the selective M-fix. Here for the robustness test, the coarse model from VCMP-ALG is required to give oscillation-free solutions for all three boundary conditions. For the rest of the results, we only check for oscillations in the VCMP-ALG solution and apply M-fix as needed for a single

boundary condition.

3.3.2 Results for Log-Normal Permeability Fields with Irregular Grids

The upscaling procedures considered in this thesis have all been extended to treat irregular quadrilateral grids. Here we assess the performance of the methods using random grids of the type considered in Section 2.2. These grids are generated by perturbing points on a uniform grid in the x and y-directions by a random amount that is prescribed to be between -0.3 and 0.3 times the grid block size. A different (random) irregular grid is used for each permeability realization.

Table 3.10 presents the total flow rate errors using random grids. As was the case using Cartesian grids (Table 3.4), VCMP-ALG provides more accurate results than VCMP-EL and TPFA-ALG except for across layering flow, for which VCMP-EL gives a smaller error. Flux and pressure errors using random grids, presented in Tables 3.11 and 3.12, show similar trends as those reported in Tables 3.5 and 3.6 for Cartesian grids. From these results we conclude that the VCMP-ALG procedure is performing as expected on irregular grids.

3.3.3 Effect of Upscaling Ratio

We now study the sensitivity of upscaling results to coarse-grid dimensions. To have a broader variety of coarse-grid sizes, we choose a fine-scale model of dimension 120×120, rather than 100×100 as used in all other log-normal permeability cases. The dimensionless correlation lengths are $\lambda_1 = 0.6$ and $\lambda_2 = 0.02$, we again set $\theta = 30°$. The fine model is upscaled to coarse models of dimensions 8×8, 10×10, 20×20, 24×24, 40×40, corresponding to upscaling ratios (in each coordinate direction) of 15, 12, 6, 5, and 3, respectively. Ten realizations are considered. Note that fixed border

Table 3.7: Robustness test: upscaled transmissibility from flow in the x-direction. Total flow rate errors, E_Q, using various upscaling methods for 25 realizations of log-normal permeability fields on 10×10 Cartesian grids.

Corner	VCMP-EL	TPFA-ALG	VCMP-ALG
In x-direction	0.068	0.075	0.039
Corner flow	0.026	0.094	0.022
Along layering	0.120	0.170	0.100

Table 3.8: Robustness test: upscaled transmissibility from flow in the x-direction. L_2 flux errors, E_f, using various upscaling methods for 25 realizations of log-normal permeability fields on 10×10 Cartesian grids.

Corner	VCMP-EL	TPFA-ALG	VCMP-ALG
In x-direction	0.085	0.313	0.059
Corner flow	0.110	0.306	0.094
Along layering	0.223	0.411	0.223

Table 3.9: Robustness test: upscaled transmissibility from flow in the x-direction. L_2 pressure errors, E_p, using various upscaling methods for 25 realizations of log-normal permeability fields on 10×10 Cartesian grids.

Corner	VCMP-EL	TPFA-ALG	VCMP-ALG
In x-direction	0.014	0.097	0.011
Corner flow	0.069	0.120	0.047
Along layering	0.074	0.181	0.082

Table 3.10: Relative errors for total flow rate, E_Q, using various upscaling methods for 25 realizations of log-normal permeability fields on 10×10 random grids.

Flow	VCMP-EL	TPFA-ALG	VCMP-ALG	VCMP-DG
In x-direction	0.057	0.047	0.026	0.0003
In y-direction	0.038	0.128	0.038	0.001
Along layering	0.125	0.017	0.016	0.004
Across layering	0.060	0.145	0.081	0.0001

Table 3.11: L_2 flux errors, E_f, using various upscaling methods for 25 realizations of log-normal permeability fields on 10×10 random grids.

Flow	VCMP-EL	TPFA-ALG	VCMP-ALG	VCMP-DG
In x-direction	0.077	0.317	0.044	0.002
In y-direction	0.120	0.368	0.085	0.008
Along layering	0.225	0.165	0.055	0.020
Across layering	0.218	0.279	0.124	0.001

Table 3.12: L_2 pressure errors, E_p, using various upscaling methods for 25 realizations of log-normal permeability fields on 10×10 random grids.

Flow	VCMP-EL	TPFA-ALG	VCMP-ALG	VCMP-DG
In x-direction	0.015	0.095	0.009	0.0004
In y-direction	0.019	0.098	0.014	0.001
Along layering	0.078	0.065	0.014	0.008
Across layering	0.043	0.046	0.018	0.0001

region size, $r_f = 2$, is used in all models. Figure 3.13 presents the total flow rate errors, L_2 flux and pressure errors using VCMP-EL and VCMP-ALG methods. It is evident that all three errors generally decrease as the coarse grid becomes more refined. The error reduction is more obvious in the total flow rate error and L_2 flux error, which are consistently larger than the L_2 pressure error. VCMP-EL results are slightly more sensitive to coarse-grid density compared to VCMP-ALG. Results for VCMP-DG, though not shown here, give small errors (1% or less) for all these grids. As expected, VCMP algorithms provide better accuracy for models with smaller upscaling ratios.

3.3.4 Stanford VI Permeability Fields

We now consider more geologically realistic systems, specifically 20 layers from the Stanford VI model (Castro, 2007). We select layers 41–60, which correspond to a deltaic system. Rather than use the full layers, we use the upper-right quarter of each layer, which retains the geological structure. Three typical models are shown in Figure 3.14. The fine grids are of dimension 75×100, and we take $\Delta x = \Delta y = 1$ (where Δx and Δy are grid block dimensions). The models are upscaled to 15×20 uniform grids.

Results for flow rate error, flux and pressure errors are presented in Tables 3.13, 3.14, and 3.15. The flow rate errors for VCMP-ALG, VCMP-EL, and TPFA-ALG are fairly comparable, though the average error (over all four flow scenarios) is slightly lower using VCMP-ALG than it is with the other two methods. For the L_2 pressure error, the best accuracy is clearly achieved using VCMP-ALG (here the errors using TPFA-ALG are considerably larger). These results indicate that, although the improvement in this case is relatively modest, VCMP-ALG continues to perform well for this deltaic system. As expected, errors in nearly all cases are the least with VCMP-DG.

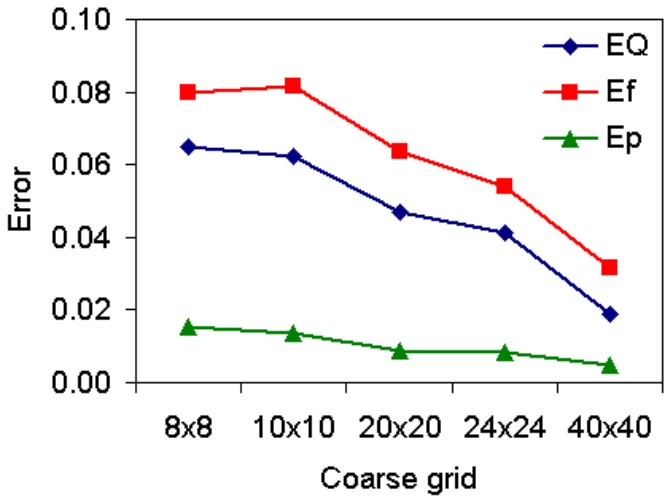

(a) VCMP-EL

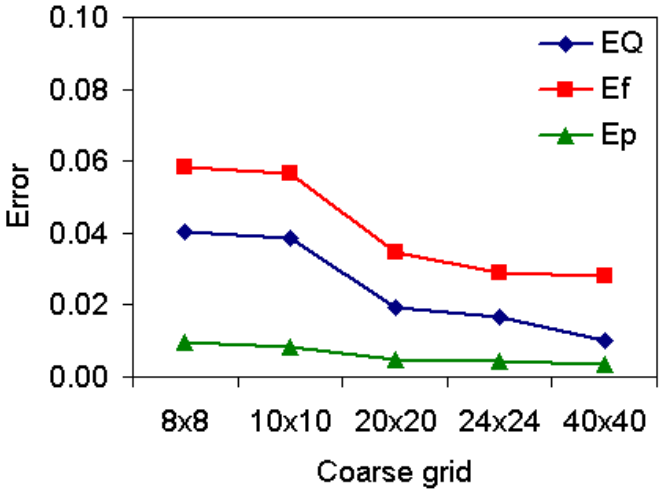

(b) VCMP-ALG

Figure 3.13: Effects of upscaling ratio on coarse-model accuracy. The fine grid is of dimension 120×120.

Table 3.13: Relative errors for total flow rate, E_Q, using various upscaling methods for 20 layers of Stanford VI on 15×20 Cartesian grids.

Flow	VCMP-EL	TPFA-ALG	VCMP-ALG	VCMP-DG
In x-direction	0.023	0.019	0.026	0.007
In y-direction	0.068	0.044	0.050	0.015
Along layering	0.079	0.030	0.044	0.036
Across layering	0.049	0.105	0.048	0.009

Table 3.14: L_2 flux errors, E_f, using various upscaling methods for 20 layers of Stanford VI on 15×20 Cartesian grids.

Flow	VCMP-EL	TPFA-ALG	VCMP-ALG	VCMP-DG
In x-direction	0.104	0.192	0.102	0.054
In y-direction	0.154	0.290	0.127	0.045
Along layering	0.266	0.241	0.154	0.119
Across layering	0.192	0.282	0.111	0.028

Table 3.15: L_2 pressure errors, E_p, using various upscaling methods for 20 layers of Stanford VI on 15×20 Cartesian grids.

Flow	VCMP-EL	TPFA-ALG	VCMP-ALG	VCMP-DG
In x-direction	0.034	0.074	0.028	0.021
In y-direction	0.025	0.051	0.020	0.009
Along layering	0.049	0.035	0.026	0.021
Across layering	0.069	0.079	0.028	0.007

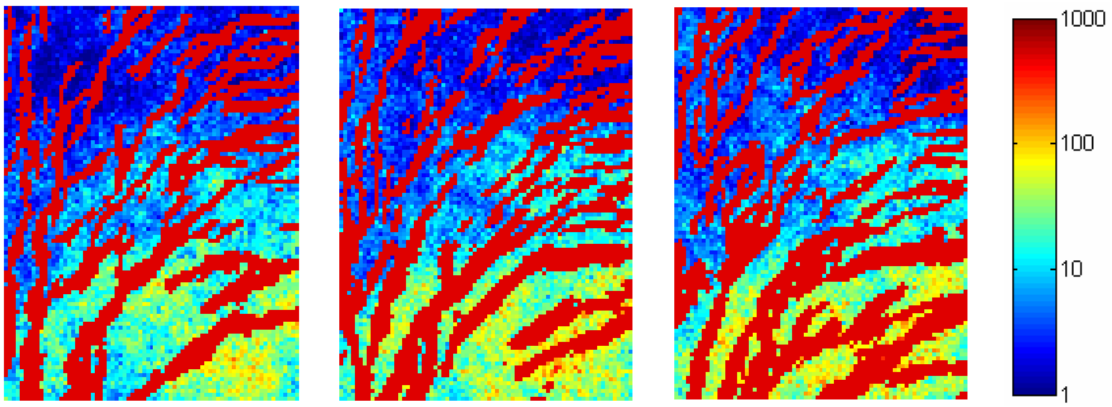

(a) Layer 42 (b) Layer 47 (c) Layer 50

Figure 3.14: Fine-scale permeability fields (75×100) of three typical deltaic layers from the modified Stanford VI model (Castro, 2007).

3.3.5 Two-Phase Flow Simulations

As stated earlier, the upscaled transmissibilities obtained from single-phase upscaling can be applied to model two-phase flow. The governing equations for a simplified two-phase flow system (incompressible fluid and rock, gravitational and capillary pressure effects neglected) can be written as:

$$\nabla \cdot (\lambda_t(S) k \cdot \nabla p) = q_t, \tag{3.3}$$

$$\frac{\partial S}{\partial t} + \nabla \cdot (u f(S)) = -q_w, \tag{3.4}$$

where S is the water saturation, t is time, $\lambda_t(S)$ and $f(S)$ are the total mobility and Buckley-Leverett fractional flow function, and q_t and q_w are the total flow rate and the water flow rate. Here we take porosity to be constant. Note that the only difference between Eq. (3.5) and Eq. (2.1) is the addition of the total mobility, given by:

$$\lambda_t = \frac{k_{rw}}{\mu_w} + \frac{k_{ro}}{\mu_o}, \tag{3.5}$$

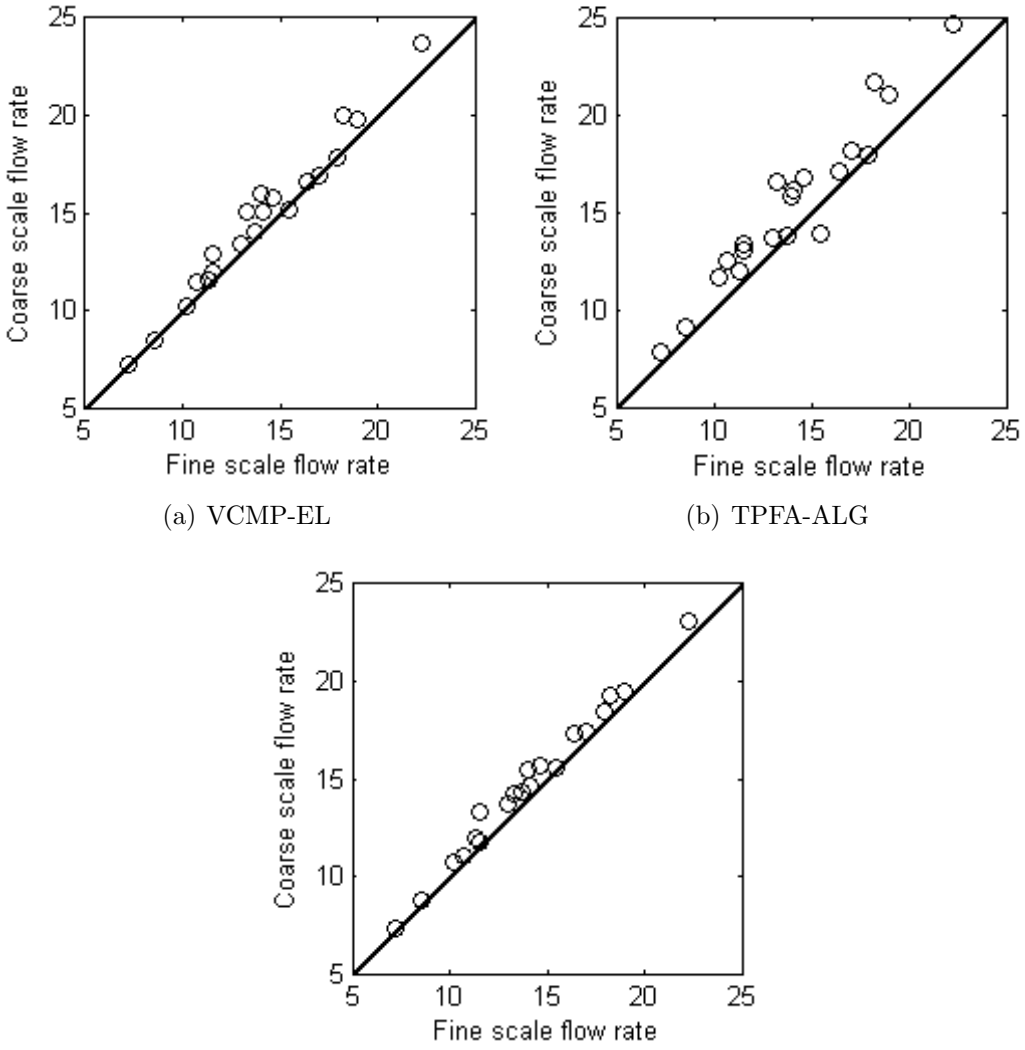

(a) VCMP-EL

(b) TPFA-ALG

(c) VCMP-ALG

Figure 3.15: Realization-by-realization comparisons for flow rate (across layering flow, Cartesian grids, the modified Stanford VI model).

where k_{rw} and k_{ro} are the relative permeability functions and μ_w and μ_o are water and oil viscosities. Here we set $k_{rw} = S^2$, $k_{ro} = (1-S)^2$ and $\mu_o/\mu_w = 5$. We use these relative permeability functions for both the fine and coarse-scale simulations (i.e., no pseudo relative permeabilities are used in the coarse-scale runs).

The transport equations are solved with the narrow-scheme (Kozdon et al., 2008), which can lessen the sensitivity of the solution to the grid orientation. The pressure boundary conditions are fixed in time and the injected fluid is water. We present results for the three different layers (Figure 3.14) that give the maximum errors (amongst all the combinations of 20 layers and four boundary conditions) in the single-phase flow rate for (1) VCMP-EL, (2) TPFA-ALG and (3) VCMP-ALG. We focus on worst-case scenarios here because all three methods perform reasonably well on average. For each case, we present results for the fine model and the three coarse models. Note that TPFA-EL results are shown below as reference only because TPFA-EL has been demonstrated to be less accurate than VCMP-EL in Chapter 2 and less accurate than TPFA-ALG in the paper of Chen and Durlofsky (2006).

Results for total flow rate (oil rate + water rate) and oil cut as a function of dimensionless time (pore volume injected, PVI) are presented in Figures 3.16, 3.17, and 3.18. In Figure 3.16(a), we see that the use of VCMP-EL can lead to significant errors – the error in flow rate at $PVI = 1$ is 39%. This error is essentially eliminated using VCMP-ALG, and results using TPFA-ALG are nearly as accurate. In Figure 3.17(a), the error in flow rate at $PVI = 1$ using TPFA-ALG is 19%. This error is reduced to 9% using VCMP-ALG, with VCMP-EL providing results very close to those of VCMP-ALG. Finally, in Figure 3.18(a), we see that the worst case for VCMP-ALG corresponds to an error of 13% at the end of the simulation (with comparable error using TPFA-ALG). For this case, the error is essentially eliminated using VCMP-EL. Our overall conclusion from Figures 3.16(a), 3.17(a), and 3.18(a) is that VCMP-ALG is the most reliable in the sense that, even for the worst case,

the error is only 13%, as opposed to the other two methods which can lead to larger errors. Oil cut plots in Figures 3.17(b) and 3.18(b) illustrate that all three methods give accurate estimates, while VCMP-ALG and TPFA-ALG are slightly more accurate than VCMP-EL in Figure 3.16(b). These results demonstrate that, for the problems tested here, the VCMP-ALG transmissibilities computed from single-phase flow computations are appropriate for use in two-phase flow simulations.

In this chapter we developed a local-global VCMP upscaling method that is capable of capturing large-scale connectivity and full-tensor effects through the combination of coarse-scale global information and flexible multipoint transmissibility calculations. The method was tested extensively for single-phase flow problems and was also used for several two-phase flow simulations. The VCMP-ALG method (developed in this chapter) and the global VCMP method (presented in Chapter 2) were demonstrated to provide high degrees of accuracy for both Cartesian and irregular quadrilateral grids. In the next chapter, we extend these methods to more complex grids – corner-point grids with pinch-outs.

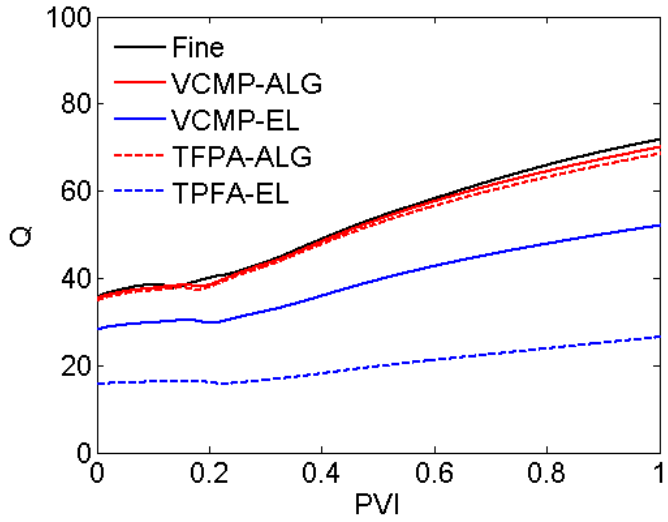

(a)

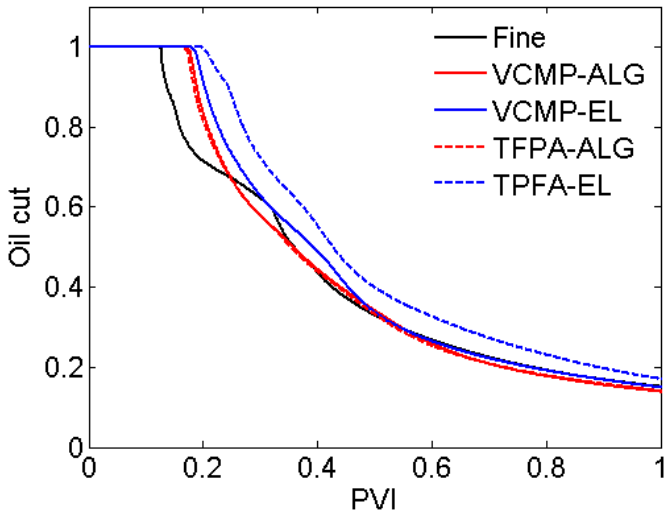

(b)

Figure 3.16: (a) Total (oil + water) flow rate and (b) oil cut for two-phase flow (along layering flow for layer 47 from modified Stanford VI model, Cartesian grids). Worst case for VCMP-EL.

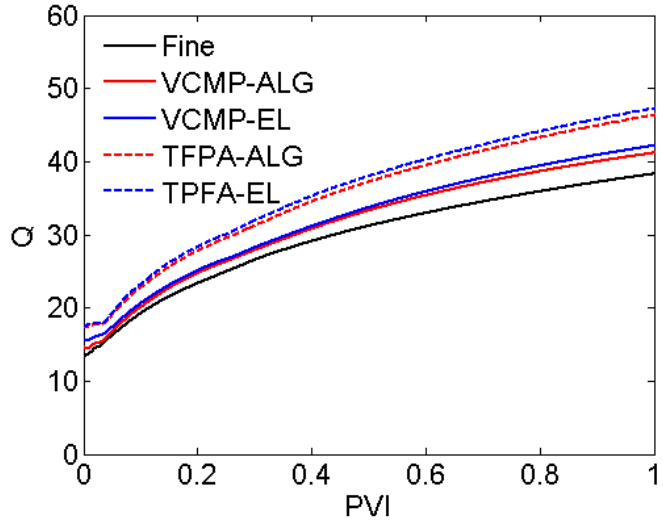

(a)

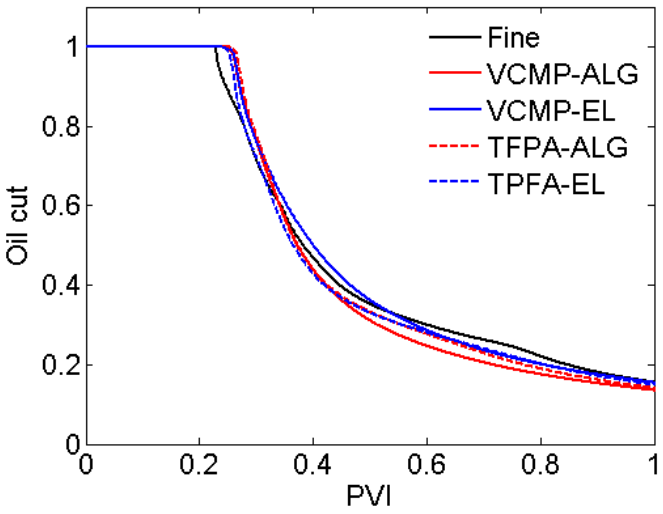

(b)

Figure 3.17: (a) Total (oil + water) flow rate and (b) oil cut for two-phase flow (across layering flow for layer 50 from modified Stanford VI model, Cartesian grids). Worst case for TPFA-ALG.

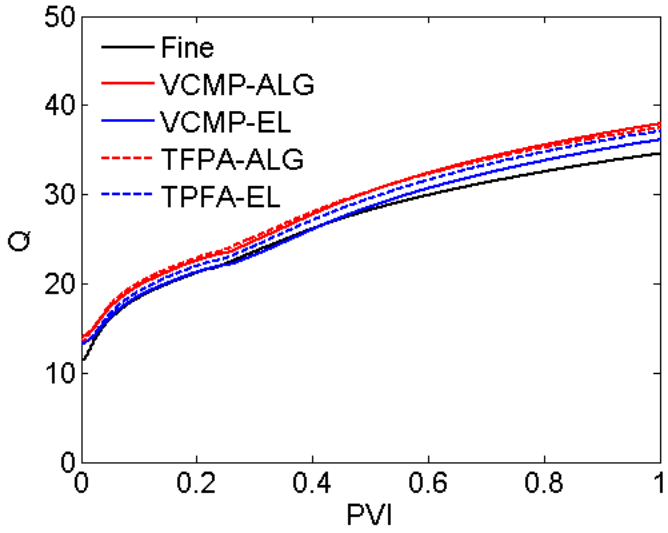

(a)

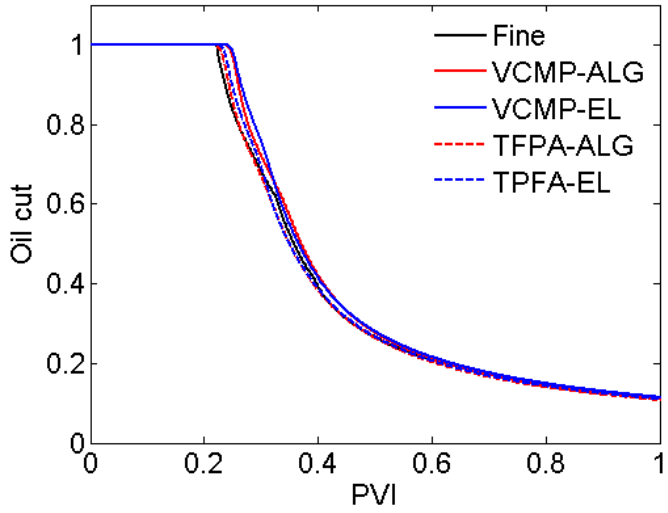

(b)

Figure 3.18: (a) Total (oil + water) flow rate and (b) oil cut for two-phase flow (across layering flow for layer 42 from modified Stanford VI model, Cartesian grids). Worst case for VCMP-ALG.

Chapter 4

Upscaling for Corner Point Grids with Pinch-Outs

In Chapters 2 and 3, the global VCMP and VCMP-ALG methods were applied to Cartesian grids and irregular quadrilateral grids, both of which are logically Cartesian grids. In this chapter, we extend these new upscaling methods to more complex grids. Particularly, we investigate corner-point grids (CPG) with pinch-outs.

4.1 Implementation Issues for CPG with Pinch-Outs

A pinch-out is a common geological feature resulting from a reduction in bed thickness due to onlapping stratigraphic sequences. Figure 4.1 shows an example of a pinch-out. The grids to capture pinch-outs often consist of mixed quadrilaterals and triangles, due to thinning or disappearance of layers. For these irregular grids, it is difficult to directly apply the upscaling techniques developed in Chapters 2 and 3.

In the representation used here, the coarse-scale grids still technically retain the

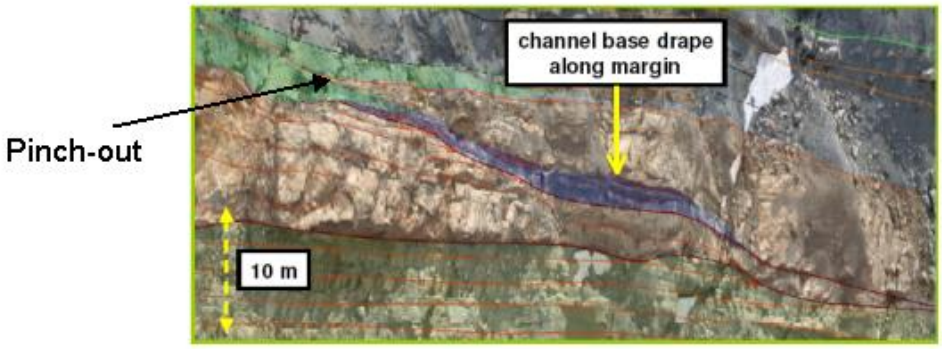

Figure 4.1: An example of pinch-out from Alpak et al. (2008).

i, j structure, however, some faces shrink to points. This means there may be cells with zero volume. We identify these zero-volume cells as inactive cells and exclude them in the pressure solution. We build non-neighbor connections between the active cells above and below the set of inactive cells. An example of a coarse-scale grid with a pinch-out is shown in Figure 4.2. There are seven layers in the j-direction. Layer four collapses for $i > 4$. A connection list can be generated by looping through all of the faces. Cell (5,3) is connected to cell (5,5) because cell (5,4) disappears.

We can readily calculate the upscaled transmissibility for each coarse face if we use two-point flux approximations. However, grids with pinch-outs are generally strongly nonorthogonal (at least in some locations), in which case an MPFA scheme is required as discussed earlier. We can apply the proposed VCMP upscaling methods to corner-point grids with pinch-outs in a similar way as we did for irregular quadrilateral grids. The key point is how to define the VCMP interaction regions. In the setup of the optimization problem in Chapter 2, we use pressure values at six points or less to construct the VCMP approximation to the flux at the target face. In two-dimensional structured grids, the selected six cells are direct neighbors of the face. The situation is more complicated for unstructured grids. In Figure 4.3, we illustrate the possible cases for a face in a pinch-out zone in two dimensions. Clearly, a face can

be surrounded by 5–7 non-zero-volume cells for this case. For consistency with the VCMP algorithm described in Chapter 2, we use six cells for the flux representation. These cells are numbered in Figure 4.3(b) through (e).

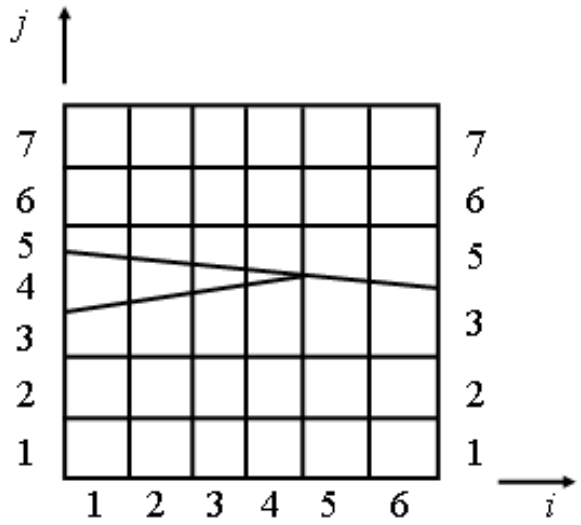

Figure 4.2: An example of a grid with a pinch-out.

The selection of the six cells proceeds as follows. First, we find the two cells that share the target face. These are designated cells 1 and 2. The two neighbors on the other two sides of cell 1 are assigned to be cells 3 and 5 (see Figure 4.3(b), (d) and (e)). If the neighbor is an inactive cell, it is not included. We repeat the same process for cell 2 to find cells 4 and 6. If any of these cells are null, we replace them with other non-null cells. For example, in Figure 4.3(c) cell 5 is not a neighbor of cell 1. In this case we find cell 5 as a neighbor of cell 6. Note that there are alternative ways to choose the six cells used to construct VCMP transmissibilities, but other approaches are not considered in this work.

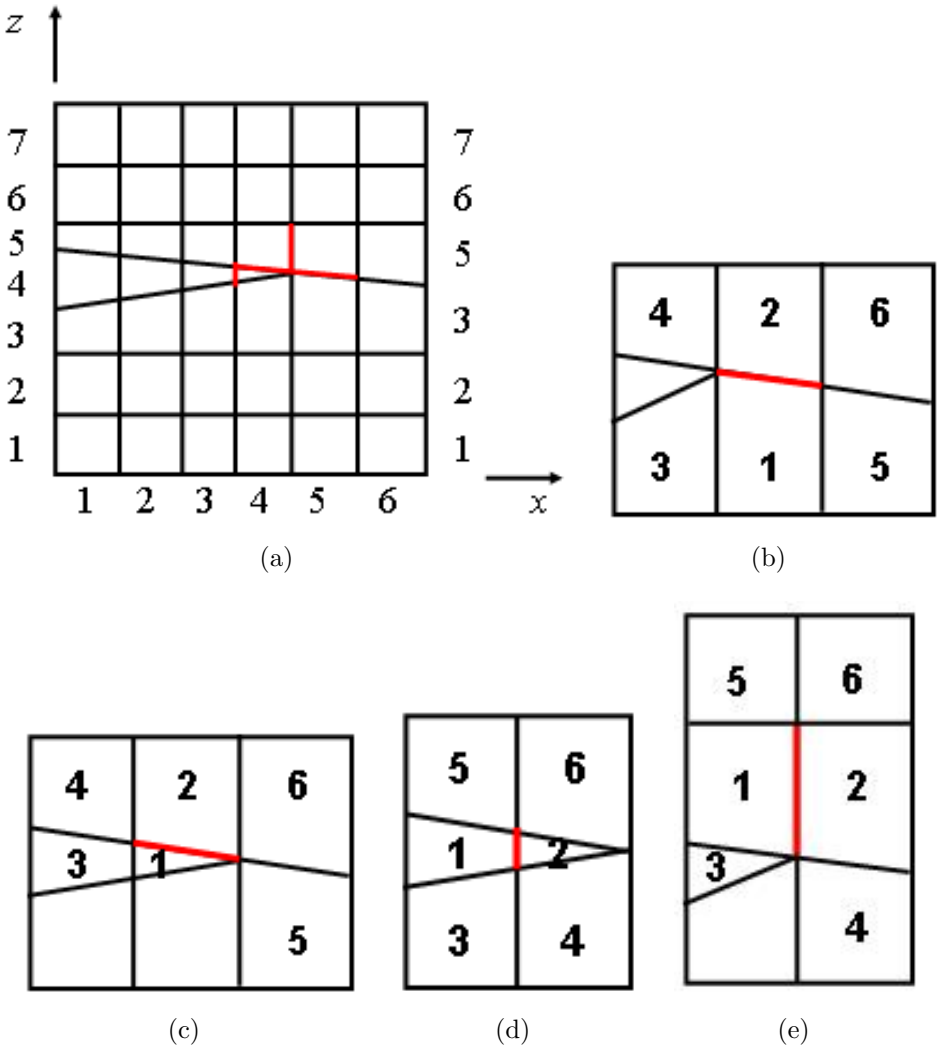

Figure 4.3: Illustration of the coarse pressures used to construct the VCMP approximation to the flux across the target faces (indicated by the thick red lines) for different scenarios encountered in corner-point grids with pinch-outs.

4.2 Numerical Results

4.2.1 Layered Model

We now present upscaling results for a synthetic pinch-out model. A constant permeability value is assigned to each layer (we refer to this case as a layered model). Figure 4.4 shows the permeability field and the coarse grid. The fine grid is of dimension 50×50 with $\Delta x = \Delta y = 1$. We add two rows of fine-scale cells at the bottom and top, respectively, to avoid the boundary condition complexity caused by pinch-outs. The coarse grid contains 29 total cells. We again apply the four boundary conditions considered earlier (defined in Chapter 2) and consider all the upscaling methods listed in Table 1.1.

First, we compare the EL and ALG methods. The errors in total flow rate, flux, and pressure are shown in Tables 4.1, 4.2, and 4.3 for extended local and adaptive local-global methods. Note that these errors are obtained for a single realization; they are not average errors as presented in Chapters 2 and 3. The TPFA-EL method generally gives the largest errors in all of the quantities. VCMP-EL provides accurate estimates for two cases (x and y-direction flows), which are similar to the flows used in the determination of upscaled transmissibilities. However, it is less accurate for the other two boundary conditions. TPFA-ALG provides high levels of accuracy in total flow rate and pressure, but flux errors are significant ($7 - 18\%$). The VCMP-ALG approach gives the best overall accuracy. The errors in total flow rate are below 1%, errors in flux are below 7%, and errors in pressure are below 2%. Thus, VCMP-ALG outperforms both VCMP-EL and TPFA-ALG.

Tables 4.4, 4.5, and 4.6 display the errors in total flow rate, flux and pressure, respectively, using global TPFA or VCMP methods. All global methods provide high degrees of accuracy in total flow rate and pressure. TPFA-DG displays some error in flux, which is improved by either TPFA-IG or global VCMP methods.

Table 4.1: Relative errors for total flow rate, E_Q, using EL and ALG upscaling methods for the layered model, using a pinch-out grid with 29 cells.

Flow	TPFA-EL	VCMP-EL	TPFA-ALG	VCMP-ALG
In x-direction	0.207	0.002	0.001	0.002
In y-direction	0.007	0.0002	0.002	0.005
Along layering	0.242	0.135	0.009	0.002
Across layering	0.093	0.147	0.018	0.010

Table 4.2: L_2 flux errors, E_f, using EL and ALG upscaling methods for the layered model, using a pinch-out grid with 29 cells.

Flow	TPFA-EL	VCMP-EL	TPFA-ALG	VCMP-ALG
In x-direction	0.383	0.020	0.067	0.016
In y-direction	0.143	0.040	0.147	0.020
Along layering	0.291	0.148	0.088	0.060
Across layering	0.199	0.148	0.179	0.064

Table 4.3: L_2 pressure errors, E_p, using EL and ALG upscaling methods for the layered model, using a pinch-out grid with 29 cells.

Flow	TPFA-EL	VCMP-EL	TPFA-ALG	VCMP-ALG
In x-direction	0.107	0.008	0.035	0.008
In y-direction	0.035	0.018	0.031	0.018
Along layering	0.087	0.095	0.017	0.014
Across layering	0.058	0.050	0.028	0.014

Table 4.4: Relative errors for total flow rate, E_Q, using global upscaling methods for the layered model, using a pinch-out grid with 29 cells.

Flow	TPFA-DG	VCMP-DG	TPFA-IG	VCMP-IG
In x-direction	0.001	0.001	0.00003	0.001
In y-direction	0.003	0.0001	0.00001	0.0001
Along layering	0.002	0.007	0.00000	0.005
Across layering	0.001	0.0001	0.00000	0.0001

Table 4.5: L_2 flux errors, E_f, using global upscaling methods for the layered model, using a pinch-out grid with 29 cells.

Flow	TPFA-DG	VCMP-DG	TPFA-IG	VCMP-IG
In x-direction	0.061	0.001	0.006	0.001
In y-direction	0.133	0.0003	0.008	0.0003
Along layering	0.034	0.015	0.00000	0.011
Across layering	0.034	0.0004	0.00000	0.0004

Table 4.6: L_2 pressure errors, E_p, using global upscaling methods for the layered model, using a pinch-out grid with 29 cells.

Flow	TPFA-DG	VCMP-DG	TPFA-IG	VCMP-IG
In x-direction	0.032	0.0002	0.039	0.001
In y-direction	0.025	0.00004	0.032	0.0001
Along layering	0.007	0.009	0.007	0.042
Across layering	0.005	0.0001	0.005	0.0004

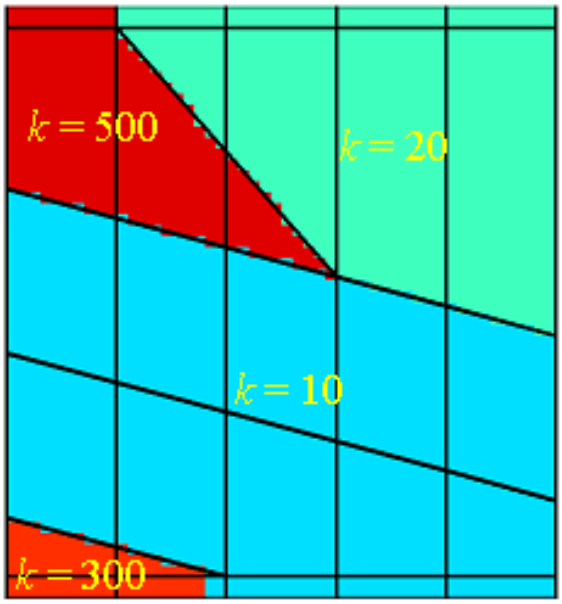

Figure 4.4: Permeability field and grid for synthetic pinch-out model.

4.2.2 Mixed Log-Normal Permeability Fields

In addition to the layered model, we also investigate log-normal permeability fields. The coarse grid is the same as the layered model (Figure 4.4). For the permeability field, we now use a fine-scale description that is reasonably consistent with the pinch-out geometry. The permeability field is of dimension 50×50 and displays oriented layering of 15° over most of the domain and 45° for the top pinched-out layer. Both types of permeability fields have dimensionless correlation lengths $\lambda_1 = 0.5$ and $\lambda_2 = 0.04$. The variance of $\log k$ is 3.0. Again we add two rows of fine-scale cells at the bottom and top as we did for the layered model. A typical fine-scale permeability field with the pinch-out coarse grid is presented in Figure 4.5.

We now present flow results averaged over ten permeability realizations. Tables 4.7, 4.8, and 4.9 display errors for total flow rate, flux and pressure for the EL and ALG methods. VCMP-ALG is overall the best method among the four considered. It improves significantly upon VCMP-EL for along layering and across layering

flows. All three errors are largely reduced. VCMP-ALG also improves upon TPFA-ALG, mainly in terms of flux errors.

It is possible that the performance of adaptive local-global methods could be further enhanced if a different pressure interpolation scheme was applied. Linear pressure interpolation, as used in this work, may not be the most appropriate for discontinuous permeability fields and highly irregular grids. Alternate interpolation schemes should be investigated in future work.

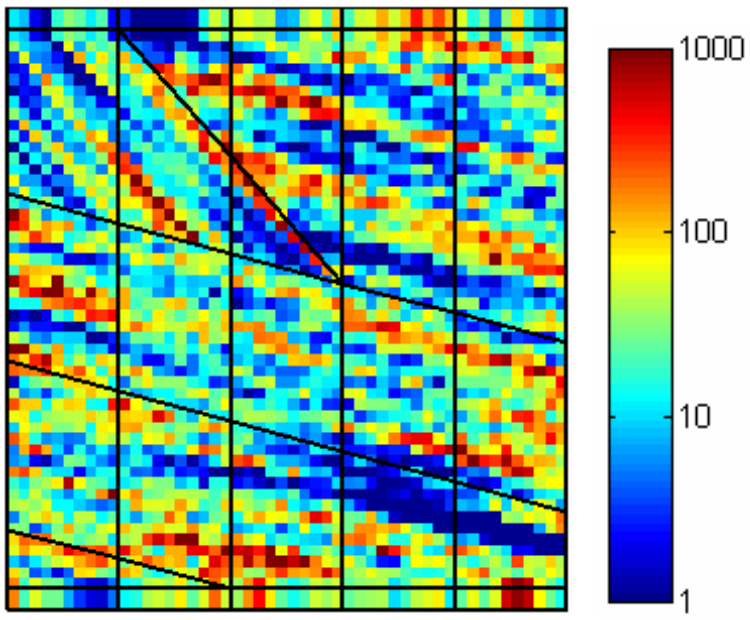

Figure 4.5: Permeability field and grid of a mixed log normally distributed permeability field.

Flow results using global TPFA or VCMP methods are presented in Tables 4.10, 4.11, and 4.12. TPFA-DG gives the least accurate results for flux (errors up to 12%) while TPFA-IG gives the least accurate results for pressure (errors up to 7.5%). Both VCMP global methods provide high degrees of accuracy in total flow rate, flux and pressure. This is consistent with our observations for general quadrilateral grids in

Table 4.7: Relative errors for total flow rate, E_Q, using EL and ALG upscaling methods for the log-normal permeability fields, using a pinch-out grid with 29 cells.

Flow	TPFA-EL	VCMP-EL	TPFA-ALG	VCMP-ALG
In x-direction	0.107	0.009	0.032	0.012
In y-direction	0.016	0.020	0.022	0.019
Along layering	0.292	0.296	0.023	0.023
Across layering	0.210	0.172	0.018	0.019

Table 4.8: L_2 flux errors, E_f, using EL and ALG upscaling methods for the log-normal permeability fields, using a pinch-out grid with 29 cells.

Flow	TPFA-EL	VCMP-EL	TPFA-ALG	VCMP-ALG
In x-direction	0.243	0.070	0.130	0.066
In y-direction	0.128	0.061	0.067	0.056
Along layering	0.331	0.317	0.106	0.090
Across layering	0.312	0.272	0.202	0.181

Table 4.9: L_2 pressure errors, E_p, using EL and ALG upscaling methods for the log-normal permeability fields, using a pinch-out grid with 29 cells.

Flow	TPFA-EL	VCMP-EL	TPFA-ALG	VCMP-ALG
In x-direction	0.139	0.079	0.101	0.079
In y-direction	0.050	0.042	0.037	0.038
Along layering	0.133	0.183	0.047	0.045
Across layering	0.181	0.178	0.072	0.051

Chapters 2 and 3. Thus global VCMP methods appear to be quite suitable for pinch-out grids.

4.3 Summary

In this chapter, we extended global and local-global VCMP methods to corner-point grids with pinch-outs. The VCMP interaction region was chosen to accommodate the existence of zero-volume cells. Simulation results demonstrated high degrees of accuracy using VCMP-ALG and global VCMP methods. These procedures generally outperformed their TPFA counterparts for the cases considered. Taken in total, these results suggest that the new VCMP global and local-global methods developed in this thesis are suitable for use with realistic simulation grids.

Table 4.10: Relative errors for total flow rate, E_Q, using global upscaling methods for the log-normal permeability fields, using a pinch-out grid with 29 cells.

Flow	TPFA-DG	VCMP-DG	TPFA-IG	VCMP-IG
In x-direction	0.012	0.0003	0.00009	0.0003
In y-direction	0.004	0.002	0.00003	0.001
Along layering	0.016	0.005	0.000002	0.001
Across layering	0.007	0.004	0.000003	0.002

Table 4.11: L_2 flux errors, E_f, using global upscaling methods for the log-normal permeability fields, using a pinch-out grid with 29 cells.

Flow	TPFA-DG	VCMP-DG	TPFA-IG	VCMP-IG
In x-direction	0.119	0.001	0.007	0.001
In y-direction	0.090	0.007	0.008	0.004
Along layering	0.075	0.044	0.001	0.003
Across layering	0.087	0.011	0.001	0.003

Table 4.12: L_2 pressure errors, E_p, using global upscaling methods for the log-normal permeability fields, using a pinch-out grid with 29 cells.

Flow	TPFA-DG	VCMP-DG	TPFA-IG	VCMP-IG
In x-direction	0.065	0.0005	0.075	0.002
In y-direction	0.016	0.001	0.018	0.007
Along layering	0.026	0.013	0.028	0.019
Across layering	0.049	0.008	0.053	0.024

Chapter 5

Conclusions and Future Directions

5.1 Summary and Conclusions

A new family of transmissibility upscaling methods based on variable compact multi-point flux approximations has been developed to accurately capture general anisotropy (full-tensor effects) in coarse-scale simulation models. Global flow information is incorporated into the upscaled models to represent large-scale permeability connectivity. Specifically, we developed global methods, in which global fine-scale flow information is used for the upscaling, and local-global techniques, in which the global flow information derives from coarse-scale simulations. The following main conclusions can be drawn from this work:

- The combination of VCMP with global upscaling methods was demonstrated to provide high degrees of accuracy for flow rate, pressure and flux. We introduced two variants of global VCMP methods: the direct global (VCMP-DG) and the iterative global methods (VCMP-IG). These approaches are clearly more accurate than their two-point flux approximation (TPFA) counterparts when applied to models with strong full-tensor effects. We illustrated this using

variogram-based geostatistical models with oriented layering and channelized systems. For the oriented-layer fine-scale models, in which case the coarse models display significant full-tensor character, the global VCMP methods provided great improvement in accuracy compared to their TPFA counterparts. For example, pressure errors from TPFA-DG and TPFA-IG are in the range of 4–16%, and they are reduced to 1% or less by VCMP-DG or VCMP-IG (Table 2.3). Flux errors of 20–38% from TPFA-DG are also reduced to 1% or less by global VCMP methods (Table 2.2). For channelized reservoir models, both global VCMP methods provide high degrees of accuracy for all quantities (e.g., flux errors below 7% in Table 2.19 and pressure errors below 4% in Table 2.20). In contrast, TPFA-DG results in large errors in flux (up to 25%, as listed in Table 2.19). However, TPFA-IG performed very well and only minimal improvement was provided by VCMP-IG methods. This is likely because full-tensor effects are not important in this case. Thus, two-point iterative global methods can accurately approximate both pressure and flux in the coarse-scale model.

- Global methods may be expensive or even prohibitive in some cases due to the need for global fine-scale solutions. Thus, to incorporate global information while retaining computational efficiency, we developed VCMP-ALG methods, where only global information at the coarse scale is used. VCMP-ALG is computationally efficient, because it avoids global fine-scale computations and also because the local fine-scale problem is solved in a reduced border region. The VCMP-ALG upscaling technique combines two existing approaches: extended local VCMP methods (VCMP-EL) and adaptive local-global TPFA methods (TPFA-ALG). Numerical results demonstrated that the adaptive local-global VCMP upscaling method provides generally more accurate results than either of the underlying methods applied individually. For the variogram-based model

with oriented layering, the total flow rate errors from TPFA-ALG and VCMP-EL were reduced by using VCMP-ALG. Compared to TPFA-ALG, the L_2 flux and pressures errors were also reduced by VCMP-ALG by factors of 2–6 and 3–10, respectively. Smaller but still significant improvements in flux and pressure accuracy relative to VCMP-EL were also observed. Simulations on the Stanford VI deltaic system showed that VCMP-ALG outperformed both VCMP-EL and TPFA-ALG in an overall sense, although the improvement for this model was fairly modest.

- The process dependency of the proposed methods was investigated. In both global VCMP methods and local-global VCMP methods, we use a complementary local flow in addition to a global flow in the determination of upscaled transmissibilities. As a result of this, and the flexible multipoint character of VCMP, these methods display some degree of robustness, meaning they can often provide a reasonable level of accuracy when applied to flows with different boundary conditions. Their accuracy for such cases was shown to be comparable to that of an extended local (VCMP-EL) method and much better than the TPFA global and local-global methods, respectively. It should be noted that a complementary local flow problem could also be used with the global or local-global TPFA methods, in which case improved robustness would likely be observed.

- We also studied the monotonicity properties of our upscaling methods. This can be an issue because the methods were developed in the context of multipoint flux approximations. It is desirable to use the selective M-fix rather than the full M-fix, that is, to only update the coefficient matrix when nonmonotone pressure solutions are observed. In some cases the improvement from using selective rather than full M-fix was slight, though in other cases (VCMP-DG

for log normal permeability fields with $\theta = 30°$) this approach reduced the flow rate, flux and pressure errors in the upscaled model significantly (from 5–20% to 0.1% or less).

- VCMP transmissibilities (computed from single-phase flow computations) are also well-suited for use in two-phase flow simulations. We considered two-phase flow for the deltaic system, and applied coarse-scale transmissibilities determined using VCMP-EL, TPFA-ALG, and VCMP-ALG. The VCMP-ALG method gives the best overall accuracy for the two-phase flow problems considered.

- The global VCMP method and VCMP-ALG method were extended to irregular quadrilateral grids. The observed levels of accuracy for all quantities were close to those achieved using uniform grids. We also extended the methods to corner-point grids with pinch-outs (in which cases the grid cells consist of not only quadrilaterals but also triangles). The non-neighbor connections were incorporated into the procedures and the VCMP interaction regions were defined appropriately. Again, benefits are achieved through the use of global VCMP methods and VCMP-ALG methods over their TPFA counterparts.

5.2 Future Directions

The global and adaptive local-global VCMP upscaling techniques developed in this work can be extended in several directions. Some recommendations for future work are outlined below.

- Develop extension of the methods to three dimensions. VCMP-EL and the M-fix were extended to three dimensions on Cartesian and adapted Cartesian grids (Lambers and Gerritsen, 2008). In addition, the adaptive local-global

method, in the context of two-point flux approximations, was extended to three dimension on Cartesian grids (Wen et al., 2006). Therefore, extension of the methods proposed in this work (including VCMP-DG, VCMP-IG, and VCMP-ALG) to three dimensions should be relatively straightforward.

- Incorporate near-well treatment into the coarse model. We evaluated various upscaling methods using flow driven by various boundary conditions, but no wells were modeled. These methods can be readily coupled with near-well upscaling procedures discussed in Durlofsky et al. (2000) and Chen and Durlofsky (2006) among others, to model well-driven flows.

- In this work, we performed single-phase upscaling and applied upscaled transmissibilities (calculated from single-phase flows) to single-phase or two-phase simulations. In the future, it might be useful to incorporate the upscaling of relative permeabilities. This should lead to better overall accuracy for both flow and transport.

- It will be useful to improve our selective M-fix procedure. This will likely require the development of necessary conditions on the A matrix (short of the M-matrix requirement) which guarantee solution monotonicity. The current M-fix is done in a predictor-corrector fashion. That is, we first calculate VCMP transmissibilities and use them to solve a coarse-scale problem. Then we check the solution monotonicity and determine extra constraints as needed and recompute t^*. Another direction to improve the M-fix procedure is to fix only wrong-signed elements with large magnitude. Based on our tests, oscillations in the pressure solutions can be removed by fixing a portion of the wrong-signed elements. However, general criteria for identifying significant wrong-signed elements still need to be determined.

- Combine upscaling methods with gridding procedures, such as flow-based gridding. Upscaling and gridding are two complementary procedures in constructing accurate coarse models. We evaluated our upscaling methods for both Cartesian and irregular grids. The irregular grids were generated randomly. The upscaling accuracy and efficiency can be improved by using appropriate grids. As reported by Gerritsen and Lambers (2008) and Lambers et al. (2008), VCMP-EL, combined with local grid adaptivity, provides high degrees of accuracy. He and Durlofsky (2006) and Prevost et al. (2005) combined flow-based gridding with upscaling methods. In the future, our upscaling methods can be applied in conjunction with one or more of these flow-based gridding techniques.

- Study upscaling for fully unstructured grids. Though the irregular grids investigated in this work are limited to general quadrilateral grids and corner-point grids with pinch-outs, our upscaling approaches should be applicable for general grid topologies. Extension of VCMP upscaling methods to fully unstructured grids will be useful because unstructured grids are receiving increasing attention (Wu et al., 2007). In addition, the application of global VCMP and local-global VCMP methods to high-aspect-ratio grids is of interest, as we have studied grids with aspect-ratio only up to five. Studies using VCMP-EL showed that reasonable accuracy was achieved for an aspect ratio of 16 (Gerritsen et al., 2006).

Nomenclature

f	flux or fractional flow function
i, j	block index
k	absolute permeability tensor
k_r	relative permeability
L_x, L_y	system lengths
p	pressure
q	well flow rate
r_f	number of rings of fine cells
t	VCMP transmissibility or time
u	Darcy velocity
E_f	L_2 flux error
E_p	L_2 pressure error
E_Q	total flow rate error
Q	total flow rate at the boundary
S	water saturation
T	transmissibility

Greek

α	relaxation parameter
α_i	weighting parameter in Eq. (2.7)

β_j	weighting parameter in Eq. (2.7)
λ_i	dimensionless correlation length
λ_t	total mobility
μ	viscosity
θ	layering orientation angle of log-normal permeability field
ε	thresholding parameter

Superscripts

$*$	upscaled parameter
0	initial step in iteration
ν	iteration counter
c	coarse-scale variable

Subscripts

G	solution of global flow
L	solution of local flow
o	oil
ref	reference value from fine-scale solution
w	water

Acronyms

ALG	adaptive local-global
CPG	corner-point grid
DG	direct global
EL	extended local
IG	iterative global
$MPFA$	multipoint flux approximation

PVI	pore volume injected
$TPFA$	two-point flux approximation
$VCMP$	variable compact multipoint

Bibliography

Aavatsmark, I.: 2002, An introduction to multipoint flux approximations for quadrilateral grids, *Computational Geosciences* **6**(3–4), 405–432.

Aavatsmark, I., Barkve, T., Boe, O. and Mannseth, T.: 1996, Discretization on non-orthogonal quadrilateral grids for inhomogeneous, anisotropic media, *Journal of Computational Physics* **127**(1), 2–14.

Aavatsmark, I., Barkve, T. and Mannseth, T.: 1998, Control-volume discretization methods for 3D quadrilateral grids in inhomogeneous, anisotropic reservoirs, *SPE Journal* **3**(2), 146–154. SPE 38000-PA.

Aavatsmark, I., Eigestad, G. T. and Nordbotten, J. M.: 2006, A compact mpfa method with improved robustness, *Proceedings of the 10th European Conference on the Mathematics of Oil Recovery*, Amsterdam, The Natherlands.

Alpak, F. O., Barton, M. D., van der Vlugt, F. F., Pirmez, C., Prather, B. E. and Tennant, S. H.: 2008, Simplified modeling of turbidite channel reservoirs, *SPE Annual Technical Conference and Exhibition*, Denver, Colorado. SPE 114854.

Barker, J. W. and Thibeau, S.: 1997, A critical review of the use of pseudorelative permeabilities for upscaling, *SPE Reseroir Engineering* **12**(2), 138–143. SPE 35491-PA.

Caers, J.: 2005, *Petroleum Geostatistics*, Society of Petroleum Engineers, Richardson, TX.

Castellini, A., Edwards, M. G. and Durlofsky, L. J.: 2000, Flow based modules for grid generation in two and three dimensions, *Proceedings of the 7th European Conference on the Mathematics of Oil Recovery*, Baveno, Italy.

Castro, S.: 2007, A probabilistic approach to jointly integrate 3D/4D seismic, production data and geological information for building reservoir models, *Ph.D. Thesis*, Stanford Univeristy, Stanford, CA.

Chen, T., Gerritsen, M. G., Lambers, J. V. and Durlofsky, L. J.: 2009, Global variable compact multipoint methods for accurate upscaling with full-tensor effects, *Computational Geosciences* . (in press).

Chen, Y. and Durlofsky, L. J.: 2006, Adaptive local-global upscaling for general flow scenarios in heterogeneous formations, *Transport in Porous Media* **62**, 157–185.

Chen, Y., Durlofsky, L. J., Gerritsen, M. G. and Wen, X. H.: 2003, A coupled local-global upscaling approach for simulating flow in highly heterogeneous formations, *Advances in Water Rescources* **26**, 1041–1060.

Chen, Y., Mallison, B. T. and Durlofsky, L. J.: 2008, Nonlinear two-point flux approximation for modeling full-tensor effects in subsurface flow simulations, *Computional Geosciences* **12**(3), 317–335.

Christie, M. A. and Blunt, M. J.: 2001, Tenth SPE comparative solution project: A comparison of upscaling techniques, *SPE Reservoir Evaluation & Engineering* **4**(4), 308–317. SPE 72469-PA.

Darman, N., Pickup, G. E. and Sorbie, K. S.: 2002, A comparison of two-phase

dynamic upscaling methods based on fluid potentials, *Computational Geosciences* **6**, 5–27.

Deutsch, C. V. and Journel, A. G.: 1998, *GSLIB: Geostatistical Software Library and User's Guide, 2nd edn.*, Oxford University Press, New York.

Ding, Y.: 2003, Permeability upscaling on corner-point geometry in the near-well region, *SPE 13th Middle East Oil Show & Conference*, Bahrain. SPE 81431.

Durlofsky, L. J.: 1991, Numerical calculation of equivalent grid block permeability tensors for heterogeneous porous media, *Water Resources Research* **27**, 699–708.

Durlofsky, L. J.: 2005, Upscaling and gridding of fine scale geological models for flow simulation, *Proceedings of the 8th International Forum on Reservoir Simulation*, Iles Borromees, Stresa, Italy.

Durlofsky, L. J., Efendiev, Y. and Ginting, V.: 2007, An adaptive local-global multiscale finite volume element method for two-phase flow simulations, *Advances in Water Resources* **30**, 576–588.

Durlofsky, L. J., Jones, R. C. and Milliken, W. J.: 1997, A nonuniform coarsening approach for the scale-up of displacement processes in heterogeneous porous media, *Advances in Water Resources* **20**, 335–347.

Durlofsky, L. J., Milliken, W. J. and Bernath, A.: 2000, Scaleup in the near-well region, *SPE Journal* **5**(1), 110–117. SPE 61855-PA.

Edwards, M. G.: 2000, Simulation with a full-tensor coefficient velocity field recovered from a diagonal-tensor solution, *SPE Journal* **5**(4), 387–393. SPE 66905-PA.

Edwards, M. G., Elf, R. A. and Aziz, K.: 1998, Quasi k-orthogonal streamline grids: Gridding and discretization, *SPE Annual Technical Conference and Exibition*, New Orleans, LA. SPE 49072.

Edwards, M. G. and Rogers, C. F.: 1998, Finite volume discretization with imposed flux continuity for the general tensor pressure equation, *Computational Geosciences* **2**(4), 259–290.

Farmer, C. L.: 2002, Upscaling: A review, *International Journal for Numerical Methods in Fluids* **40**, 63–78.

Gerritsen, M. G. and Durlofsky, L. J.: 2005, Modeling fluid flow in oil reservoirs, *Annual Review of Fluid Mechanics* **37**, 211–238.

Gerritsen, M. G. and Lambers, J. V.: 2008, Integration of local-global upscaling and grid adaptivity for simulation of subsurface flow in heterogeneous formations, *Computational Geosciences* **12**(2), 193–208.

Gerritsen, M. G., Lambers, J. V. and Mallison, B. T.: 2006, A variable and compact mpfa for transmissibility upscaling with guaranteed monotonicity, *Proceedings of the 10th European Conference on the Mathematics of Oil Recovery*, Amsterdam, The Netherlands.

Gomez-Hernandez, J. J. and Journel, A. G.: 1994, Stochastic charaterization of grid-block permeability, *SPE Formation Evaluation* **9**(2), 93–99. SPE 22187-PA.

He, C. and Durlofsky, L. J.: 2006, Structured flow-based gridding and upscaling for modeling subsurface flow, *Advances in Water Resources* **29**, 1876–1892.

He, C., Edwards, M. G. and Durlofsky, L. J.: 2002, Numerical calculation of equivalent cell permeability tensors for general quadrilateral control volumes, *Computational Geosciences* **6**(1), 29–47.

Hesse, M., Mallison, B. T. and Tchelepi, H. A.: 2008, Compact multiscale finite volume method for heterogeneous anisotropic elliptic equations, *SIAM Multiscale Modeling and Simulation* **7**(2), 934–962.

Holden, L. and Lia, O.: 1992, A tensor estimator for the homogenization of absolute permeability, *Transport in Porous Media* **8**, 37–46.

Holden, L. and Nielsen, B. F.: 2000, Global upscaling of permeability in heterogeneous reservoirs: the output least squares (OLS) method, *Transport in Porous Media* **40**, 115–143.

Hui, M. and Durlofsky, L. J.: 2005, Accurate coarse modeling of well-driven, high mobility ratio displacements in heterogeneous reservoirs, *Journal of Petroleum Science and Engineering* **49**, 37–56.

Jenny, P., Lee, S. H. and Tchelepi, H. A.: 2003, Multi-scale finite-volume method for elliptic problems in subsurface flow simulation, *Journal of Computational Physics* **187**, 47–67.

King, M. J., MacDonald, D. G., Todd, S. P. and Leung, H.: 1998, Application of novel upscaling approaches to the magnus and andrew reservoirs, *SPE European Petroleum Conference*, The Hague, The Netherlands. SPE 50643.

King, M. J. and Mansfield, M.: 1999, Flow simulation of geological models, *SPE Resrvoir Evaluation & Engineering* **2**(4), 351–367. SPE 57469.

Kozdon, J., Mallison, B. and Gerritsen, M.: 2008, Robust Multi-D transport schemes with reduced grid orientation effects, *Transport in Porous Media* . DOI 10.1007/s11242-008-9281-1.

Lambers, J. V. and Gerritsen, M. G.: 2008, Spatially-varying compact multi-point flux approximations for 3-D adapted grids with guaranteed monotonicity, *Proceedings of the 11th European Conference on the Mathematics of Oil Recovery*, Bergen, Norway.

Lambers, J. V., Gerritsen, M. G. and Mallison, B. T.: 2008, Accurate local upscaling with variable compact multipoint transmissibility calculations, *Computational Geosciences* **12**(3), 399–416.

Lee, S. H., Tchelepi, H. A., Jenny, P. and DeChant, L. J.: 2002, Implementation of a flux-continuous finite-difference method for stratigraphic, hexahedron grids, *SPE Journal* **7**(3), 267–277. SPE 80117-PA.

Mallison, B. T., Chen, Y. and Durlofsky, L. J.: 2006, Nonlinear two-point flux approximations for simulating subsurface flows with full-tensor anisotropy, *Proceedings of the 10th European Conference on the Mathematics of Oil Recovery*, Amsterdam, The Netherlands.

Nordbotten, J. M. and Aavatsmark, I.: 2005, Monotonicity conditions for control volume methods on uniform parallelogram grids in homogeneous media, *Computational Geosciences* **9**, 61–72.

Nordbotten, J. M., Aavatsmark, I. and Eigestad, G. T.: 2007, Monotonicity of control volume methods, *Numerische Mathematik* **106**(2), 255–288.

Pickup, G. E., Ringrose, P. S., Jensen, J. L. and Sorbie, K. S.: 1994, Permeability tensors for sedimentary structures, *Mathematical Geology* **26**(2), 227–250.

Pickup, G. E. and Sorbie, K. S.: 1996, The scaleup of two-phase flow in porous media using phase permeability tensors, *SPE Journal* **1**(4), 369–382. SPE 28586-PA.

Prevost, M., Lepage, F., Durlofsky, L. J. and Mallet, J. L.: 2005, Unstructured 3D gridding and upscaling for coarse modeling of geometrically complex reservoirs, *Petroleum Geoscience* **11**, 339–345.

Renard, P. and de Marsily, G.: 1997, Calculating equivalent permeability: A review, *Advances in Water Resources* **20**, 253–278.

Romeu, R. K. and Noetinger, B.: 1995, Calculation of internodal transmissibilities in finite difference models of flow in heterogeneous media, *Water Resources Research* **31**(4), 943–959.

Wen, X. H., Chen, Y. and Durlofsky, L. J.: 2006, Efficient 3D implementation of local-global upscaling for reservoir simulation, *SPE Journal* **11**(4), 443–453. SPE 92965-PA.

Wen, X. H., Durlofsky, L. J. and Edwards, M. G.: 2003a, Upscaling of channel systems in two dimensions using flow-based grids, *Transport in Porous Media* **51**, 343–366.

Wen, X. H., Durlofsky, L. J. and Edwards, M. G.: 2003b, Use of border regions for improved permeability upscaling, *Mathematical Geology* **35**(5), 521–547.

Wen, X. H., Durlofsky, L. J., Lee, S. H. and Edwards, M. G.: 2000, Full tensor upscaling of geologically complex rerservoir descriptions, *SPE Annual Technical Conference and Exhibition*, Dallas, TX. SPE 62928.

Wen, X. H. and Gomez-Hernandez, J. J.: 1996, Upscaling hydraulic conductivities in heterogeneous media: An overview, *Journal of Hydrology* **183**, ix–xxxii.

Wu, X. H., Efendiev, Y. R. and Hou, T. Y.: 2002, Analysis of upscaling absolute permeability, *Discrete and Continuous Dynamical Systems-Series B* **2**(2), 185–204.

Wu, X. H., Stone, M. T., Parashkevov, R. R., Stern, D. and Lyons, S. L.: 2007, Reservoir modeling with global scaleup, *15th SPE Middle East Oil & Gas Show and Conference*, Bahrain International Exhibition Center, Bahrain. SPE 105237.

Zhang, P., Pickup, G. and Christie, M.: 2008, A new practical method for upscaling in highly heterogeneous reservoir models, *SPE Journal* **13**(1), 68–76. SPE 103760-PA.